# Entropic Bonding in Nanoparticle and Colloidal Systems

by

Eric S. Harper

A dissertation submitted in partial fulfillment
of the requirements for the degree of
Doctor of Philosophy
(Materials Science and Engineering)
in The University of Michigan
2018

Doctoral Committee:

Professor Sharon C. Glotzer, Chair
Assistant Professor Greg van Anders, Co-Chair
Professor John Kieffer
Professor Michael J. Solomon

Eric S. Harper

harperic@umich.edu

ORCID iD: 0000-0002-7058-1686

# Dedication

This work is dedicated to my wonderful wife Madeline; and to my family, Steve, Laurie, and Carol, who have supported me throughout the years.

# Acknowledgements

I would like to acknowledge my high school Chemistry teachers Tony Rainsberger and James Slagel, for starting me on the path I find myself on today (and having the foresight to say that my middle name was “entropy”); Dr. Michael Elsass, for showing me the power and importance of simulation and modeling; and Dr. Benjamin Leever and Dr. Vladimir Benin, my undergraduate thesis advisors.

I would also like to acknowledge the help and support of my colleagues here at the University of Michigan: Ryan Marson, Richmond Newman, Matthew Spellings, Carl Simon Adorf, and Michael Waters. While research can be lonely at times, these individuals were always there to lend a helping hand and help me overcome the obstacles that lie across the way.

I would also like to acknowledge Joshua Anderson for his mentorship, especially with regards to code development. I would not have half the programming knowledge I have today without his mentorship, nor would I have been able to develop the analysis software *Freud*.

I would like to acknowledge Jeffrey Wan and Brendon Waters, two students I had the pleasure of mentoring in my time at Michigan. Both contributed to the work on the “Cube Slices” project; hopefully they learned as much from me as I did from them.

I would like to acknowledge the help and support of Advanced Research Computing at the University of Michigan, and the Michigan Institute for Computational Discovery and Engineering, especially Dr. Mariana Carrasco-Teja. We worked together to found the Scientific Computing Student Club to advance scientific computing education, opportunities, and resources for graduate students at the University of Michigan.

I would like to acknowledge the help and support of Karen Coulter. Her hard work enables the great research done in the Glotzer Group, and I would not have been able to accomplish this work without her help.

Finally, I would like to acknowledge my graduate advisors Sharon Glotzer and Greg van Anders, and my committee members John Kieffer and Michael Solomon, as well as Robert Ziff, who graciously is serving as proxy for Michael Solomon on my committee. Both Sharon and Greg have molded me into the researcher I am today, and I am grateful for all the opportunities they've given me over the years.

# Table of Contents

# List of Tables

# List of Figures

Figure 6-5 **a** Equation of state and **b** Orientation-orientation hexatic order paramete for elongated rhombs with shape parameter $\gamma = 0{,}14{,}13{,}512{,}12{,}1$. Note the 1st-order phase transitions between fluid and ordered solid phases for $\gamma \geq 512$, in contrast with the continuous fluid-to-RTP transition observed for $\gamma \leq 13$. Both continuous and 1st-order transitions are present for $\gamma = 14{,}13$. While the RTP is stable for $\gamma = 14$ over a relatively large pressure window $\Delta P* \approx 2.0$, the RTP is only stable for $\Delta P* \approx 0.5$ for $\gamma = 13$. The orientation-orientation hexatic order parameter $\Psi 6{,}6$ shows the same phase transitions as the equation of state. The values of $\Psi 6{,}6$ for the different shapes indicate which motifs are preferred in the dense fluid phase. For $\gamma = 1, \Psi 6{,}6 \to 0$, indicating that herringbone and hexagonal bonds compete equally in the fluid phase, resulting in an overall lack of orientational order congruent with either RTP or parallel phases. The fact that $\Psi 6{,}6 > 0$ indicates that the hexagonal bonds are preferred, as observed in Ref. 173[173]. As the value of $\gamma$ decreases, the value of $\Psi 6{,}6$ in the fluid phase increases, indicating an increased preference for hexagonal to herringbone order. For $\gamma \leq 13$, values of $\Psi 6{,}6$ associated with the RTP are observed, indicating the presence of the RTP phase. **c** Phase diagram constructed from **a** and **b**. Red dots represent the edge of the fluid phase connected by dashed lines representing the continuous transition between the fluid and RTP. Blue squares represent the solid phase, connected by a solid line representing the 1st-order phase transition between the RTP or fluid and parallel phases. The continuous-continuous phase transition for $\gamma = 0$ is

# Abstract

Scientists and engineers will create the next generation of materials by precisely controlling their microstructure. One of the most promising and effective methods to control material microstructure is self-assembly, in which the properties of constituent “particles” guide their assembly into the desired structure. Self-assembly mechanisms rely on both inherent interactions between particles and emergent interactions resulting from the collective effects of all particles in the system. These emergent effects are of interest as they provide minimal mechanisms to control self-assembly, and thus can be used in conjunction with other assembly methods to create novel materials.

Literature shows that complex phases can be obtained solely from hard, anisotropic particles, which are attracted *via* an emergent *Directional Entropic Force*. This thesis shows that this force gives rise to the *entropic bond*, a mesoscale analog to the chemical bond. In Chapter 3 I investigate the self-assembly of a system from a random tiling into an ordered crystal. Analysis of the emergent directional entropic forces reveal the importance of shape in the final self-assembled system as well as the ability for shape manipulation to control the final self-assembled structure. In Chapter 4, I investigate three-dimensional analogs of two-dimensional systems in Chapter 3, explaining the self-assembly behavior of these systems *via* understanding of the emergent directional entropic forces. In Chapter 5 I investigate the nature of the entropic bond, investigating

two-dimensional systems of hexagonal nanoplatelets. The Entropic bond is quantified, and the ability to manipulate the bonds to produce similar self-assembly behavior to chemically-functionalized nanoparticles is demonstrated. Finally, Chapter 6 investigates the phase transitions of the general class of particle studied in Chapter 5, showing the ability for particle shape to change the type of phase transition present in a system of nanoparticles as well as stabilize phases otherwise not found. As a whole, this work details the nature of the entropic bond and its use in directing the self-assembly of systems of non-interacting anisotropic particles.

# Chapter 1

# Introduction

## 1.1 Materials Engineering and Self-Assembly

Material structure determines materials properties, thus the design and control of material microstructure one of the most important goals of materials science and engineering. Throughout the ages, engineers have done their best to create the best tools and products with the materials available to them. Materials were so important in human history that anthropologists refer to the various epochs of human history by the type of material that dominated their technology: Stone, Bronze, Iron, with the modern-day dubbed the “Silicon-Age.”

In each of these ages, the natural microstructure of the materials determined the final material properties. While engineers and scientists discovered many impressive ways to alter material structure and thus the material properties (some still in use today), the material, that is the atoms and molecules that comprise the bulk material, still dominates the final structure and properties. Various methods including alloying and tempering allowed for crude manipulation of microstructure, such as the manipulation of the microstructure of iron *via* the addition of carbon to create steel alloys. Such research can be thought of as a “forward” investigation, starting from the material building blocks and ending with the material property. However, employing a “reverse” strategy that starts from a

desired property and works backward to identify the structure and building block required will be key to creating the next generation of materials.

Control of material microstructure opens the door to the creation of *metamaterials*, materials with properties not governed by the material itself, but rather by the underlying structure. Materials with negative Poisson ratios (expand/contract perpendicular to expansion/contraction) or negative indices of refraction are coveted due to their novel properties. There are numerous examples of such metamaterials in nature[1,2]. Butterfly wings[3–5], beetle shells[6], and even some berries[7], do not use pigmentation, but rather structural coloration i.e. the underlying structure of the material to produce their coloration.

A second class of novel materials under investigation are reconfigurable, or dynamic materials[8–14]. The historically dominant materials have typically been static: once cast, the structure of concrete is set. However, the ability for materials to reconfigure *in situ* increases their usefulness. Examples include self-healing materials[15], materials with response to slight changes in chemical concentration[16], light[17], and electric fields[9,18–21], and even self-propelled active particles[22].

Such materials require precise control over each constituent of the system, and current manufacturing methods are limited in created large quantities of these materials, especially at the sizes we desire. Let's imagine a relative small system, 1 mole of aluminum atoms, or a cube with sides of $2.23\ cm$ (a little less than $1\ in.$ per side), and that we require these atoms to all be arranged in a very particular way to obtain particular desired mechanical properties. This isn't a very

large piece of aluminum at the macro scale, and even if we are very generous with our manufacturing time and say one of these cubes can take an entire day to manufacture, any device that we created an atom at a time would have to place almost $7 \cdot 10^{18}$ atoms *per second!*

What if, rather than designing a device to place the atoms, the atoms could direct themselves to form the desired structure? After all, atoms and molecules already do this in all the familiar materials around us, such as Iron. However, we are rather limited in controlling the assembly of Iron due to its exact chemical (quantum mechanical and electronic) nature. What if we were not limited by choice of atom or molecule to determine the microstructure, but could rather choose the desired structure and design atoms and molecules to form that structure, to create a "supramolecular" chemistry? This has been achieved at the nano- $(10^{-9}m)$ and colloidal- (typically $O(100 - 1000nm)$) scale: both the shape and functionalization of these particles can be varied, allowing for a host of different ways to direct the self-assembly of these particles[23–37].

Nanoparticle systems possess many more dimensions to manipulate to control the final structure compared to atomic systems. However, this design space is infinite, and experiments, even on the nanoscale, are incredibly expensive, requiring years of research to develop the techniques and tools required to create particles with particular functionality and shape[23,38]. Investment of this time and energy must be measured, as it would be very unfortunate to spend a decade of work to finally determine a particular nanoparticle is relatively uninteresting e.g. many nanoparticle systems self-assemble FCC lattices, and

spending a decade to find one more FCC-former would be a relatively poor investment. What if there was a way to know before spending all that time and all that money that the particle you were going to make would do what you wanted it to?

## 1.2 Computer Simulation

Fortunately, there is a way to know, or at the very least have very good reason to believe a nanoparticle will behave as you expect: computer simulation[39]. After the development of computers to model the cascading fission reaction for use in atomic weaponry, the first uses of computers were for this very problem[40,41], and nearly seventy years later, more advanced computers and simulations still probe the depths of self-assembly research.

Modern computers trace their start back to analog “computers” used to crack codes in World War II, and at Los Alamos to design the first fusion weapons. It was on the MANIAC computer at Los Alamos that the first hydrogen bombs were designed; the MANIAC also ran the first *Monte Carlo* simulations, so-named due to their dependence on random numbers to simulate the systems of interest. Named Metropolis Monte Carlo after Nicholas Metropolis, the leader of the Los Alamos research team, the equation of state was computed for systems of hard disks by sampling their equilibrium distribution[42]. This problem is not only a canonical problem in soft matter and self-assembly, its underlying methods and results inform the research presented here. A few years later, the first molecular dynamics simulations we conducted on UNIVAC systems. These simulations investigated three-dimensional systems of hard spheres[43]. Rather than sample

equilibrium distributions *via* generation of random numbers, the actual Newtonian equations of motion are computed, providing dynamic information about the system, in addition to information about the equilibrium state and structure of the system.

Compared to today's standards, these computers simulated tiny systems on primitive hardware; reproducing the first Monte Carlo simulations could be done in seconds on any of today's smartphones, but the underlying methods still form the basis for the simulation methods and software used in self-assembly research today[39,44]. These simulations provided an important avenue into understanding self-assembly. In fact, it was their limited nature that allowed some of the most important insights to be learned. Rather than be able to perfectly capture the interactions between atoms, compute molecular orbitals and bonds between atoms, these simulations had to make many assumptions about the systems under investigation, limiting them to the simplest geometries (disks and spheres) with the simplest interactions (simple repulsion or perfectly hard particles)[45]. This lead to the discovery that entropy can cause the *ordering* of systems.

## 1.3 Entropy-driven self-assembly

Systems of hard spheres self-assemble an FCC lattice[46–49]. While well-known today, this was an important discovery at the time, especially since there exist no intrinsic interparticle forces to guide this assembly[43,50–54]. To understand what guides the self-assembly, thermodynamic analysis is necessary. Working in the canonical thermodynamic ensemble (constant number of particles, $N$; constant

volume, $V$; constant temperature, $T$), the Helmholtz Free-Energy is minimized in the equilibrium state of the system:

$$F = U - TS$$

Hard particles have no interaction energy, and therefore the internal energy $U$ of every allowable configuration of the system i.e. no particles are overlapping, is equal to zero. Thus, we arrive at the following reduced equation for the free energy:

$$F_{HP} = -TS$$

Interpretation of this equation leads to an important conclusion: at constant temperature, the equilibrium structure of a system of hard particles is the one that *maximizes* the entropy of the system; or, entropy can cause the ordering of systems!

### 1.3.1 Depletion interactions and self-assembly

It is perhaps easiest to understand this entropy-driven self-assembly *via* the *depletion interaction*[46,55–59]. Depletion systems are comprised of two different species: small polymers called *depletants*, and larger particles. Increasing depletant concentration results in the aggregation of the larger particles into close-packed structures. This phenomenon is a result of entropy: even though the entropy of individual large particles decreases, the entropy of the depletants increases by a greater amount, resulting in the overall increase in entropy for the system, and minimizing the free-energy of the system.

Examples of this are numerous, and control of the depletion effect is an important avenue of research for self-assembly. However, this understanding of entropy

trade-off does not satisfactorily explain why systems of hard spheres (and other shapes) would successfully self-assemble an ordered FCC crystal, as there exist no depletant species to offset the loss of entropy experienced by the larger particles.

### 1.3.2 Self-depletion and polyhedral self-assembly

The lack of an explicit depletant species in systems that self-assemble due to entropy implies that these systems are self-depleting: pairs and clusters of particles locally order (lose entropy), which is offset by the increase in global order for the rest of the particles in the system[60]. At first, polymer depleting and self-depleting systems would appear to be very different; however, it has been known since 1949[61] that monodisperse sphere systems have preferred distances, resulting from the balance of attractive and repulsive forces. This leads to the understanding that the net attraction between colloids results from the "sea" particles forcing local configurations, regardless of the composition of the sea particles[60].

Experimental research into synthesis of anisotropic nanoparticles and colloids showed a variety of interesting self-assembled structures[23,62–68]. Given the high dimensionality of the shape "dimension" in this design space, simulation and entropy-focused analysis is required to guide the eventual experimental synthesis of nanoparticles[38].

Simulations of hard polyhedra reveal an extraordinary variety in the number of structures that can be assembled due solely to the shape (and thus the entropy) of the nanoparticle[34,69]. Exotic phases including the quasicrystal are even

obtainable simply by manipulating the shape of these nanoparticles[32,70,71]. These simulations showed that nanoparticle shape plays a large role in the resulting self-assembled phase, and that these phases are a result of the local motifs found in dense fluids prior to self-assembly[34]. This means that whatever phenomenon is responsible for this ordering is *emergent* (due to the number of particles in the system as well as the density of the system), and as noted with the hard spheres, is also entropic. This evidence points to the existence of an *emergent, directional entropic force*, not unlike the attractive forces resulting in self-assembly of functionalized nanoparticle and colloidal systems, or even the forces resulting in hydrogen bonding in molecular systems[60].

### 1.3.3 Directional Entropic Force

The discovery that it was the local motifs within dense fluids[70,72–74] prior to self-assembly rather than the densest packing structures[35,75–81], along with the knowledge that different shapes were capable of assembling a vast array of different structures, including quasicrystals, implies the existence of a force, similar to the depletion interaction, that emerges due to the crowding and shape of the particles in the system[60,72,82,83]. This force must therefore be *entropic* in nature, as entropy is the only quantity that varies to lower the free-energy of the system.

Much in the same manner as the measurement of the potential of mean force[84] in a system of isotropic particles, the net attraction and repulsion between isotropic particles, the emergent entropic force between particles may be quantified *via* the

*potential of mean force and torque* (torque accounting for the preferred orientations that anisotropic particles prefer in entropy-controlled systems)[60,82].

### 1.3.4 Entropic Bonding in Nanoparticle and Colloidal Systems

If there exists an emergent, directional entropic force, and such a force can be quantified, do there also exist *emergent, entropic bonds* between anisotropic nanoparticles and colloids? In this work, I investigate this emergent directional entropic force and the entropic bonds they form between hard particles. In Chapter 2, I summarize the methods used to simulate and analyze systems of hard, anisotropic nanoparticles. Of note are the methods for computing the potential of mean force and torque (PMFT), used to compute the emergent directional entropic forces, as well as the techniques to identify and quantify the resulting entropic bonds. In Chapter 3 I investigate the self-assembly of shape-allophiles, shapes specifically designed to fit together in a complementary fashion. By measuring the directional entropic force between these shapes, I determine the effect that manipulating the allophilic pattern has on the assembly propensity of these shapes into the desired ordered structure. The addition of allophilic patterning increases the attractive force between hard particles, resulting in *entropic bonds*. This leads to the directed self-assembly of an ordered structure from a shape that does not order without allophilic patterning. details the determination of the entropic bond in an investigation of hard hexagons and elongated rhombs; the similarity of entropic bonds to established systems exhibiting hydrogen bonding and chemical functionalization is established, demonstrating the existence of these bonds. In Chapter 4 I

investigate the three-dimensional extension of the hard-square system in Chapter 3, looking at the hierarchical self-assembly of six different hard cube derivatives. I observe the self-assembly behavior of these systems, identifying a previously unreported cubatic phase in 2:1 aspect ratio rectangular prisms. By analyzing the pair configurations preferred by these shapes in their dense fluid phase, I gain insight into the shape features leading to successful self-assembly. In Chapter 5 I quantify the entropic bond by analyzing the self-assembly of a family of hexagons. By computing the entropy density for regular hexagons, I can separate the landscape into distinct geometric regions. These distinct regions are identified as entropic bonds. I track particles in simulation, determining the lifetime of these entropic bonds, finding similarities with hydrogen bonds. Further analysis of entropic bonds provides insight into the self-assembly behavior of hexagonal nanotiles, providing a method to direct the formation of entropic bonds, thereby controlling the self-assembled structure. I continue to investigate these hexagonal systems in chapter Chapter 6, determining the effect that entropic bonding has on the observed phase transitions. I show the ability for particle shape to change the number and type of phase transitions present in the hexagonal nanotile system. Such shape manipulation provides scientists and engineers an additional method to explore for the creation of reconfigurable materials. Finally, in Chapter 7 I conclude by discussing the work as a whole. I explore questions this work raises and potential directions for future research.

# Chapter 2

# Methods

## 2.1 Monte Carlo Simulation

I model nano- and colloidal-scale systems using Monte Carlo (MC) simulation, named due to its use of “random events” to investigate system equilibrium[42,85]. MC samples the equilibrium distributions of a system to gather statistical information about thermodynamic quantities of interest[39,44]. MC methods can be employed in a wide variety of systems, even being used for something as simple as estimating the area of a circle. Unlike molecular dynamics[86–92], MC does not require the use of potentials nor requires restrictions on the geometry of a particle, making it better-suited for investigating the effect that shape has on hard particle self-assembly.

### 2.1.1 Metropolis Method

Models of nanoparticle systems typically require the use of hundreds or thousands (even millions) of individual particles. I employ the metropolis approach[42,44,93] to generate and sample equilibrium distributions, as well as allowing us to draw conclusions regarding the assembly propensity of our particles because the algorithm resembles the behavior of particle in the Brownian limit. In metropolis MC, an initial configuration of the system is

generated, and then this system is integrated over a number of *Monte Carlo Sweeps*. Each sweep is comprised of $N$ individual steps:

1. A particle $(i)$ in the system is chosen at random
2. A *trial move* for $i$ is proposed: either a *translation* move, in which its coordinates are updated, or a *rotation* move, in which its orientation is updated
3. The trial move is accepted if no overlaps are introduced; otherwise it is rejected

Because one trajectory frame is directly computed from a previous frame, it is important to allow sufficient MC sweeps between frames to avoid *autocorrelation*. This is required to properly compute thermodynamic quantities, which require fair sampling of the equilibrium distribution, so that the samples are statistically independent.

### 2.1.2 Thermodynamic Ensembles

To properly understand the behavior of these models, the thermodynamic ensemble must be properly taken into account. In this thesis two ensembles are used: The *Canonical* $(NVT)$ *Ensemble* and the *Isothermal-Isobaric* $(NPT)$ *Ensemble*. In both these ensembles the number of particles $N$ is held constant. In both systems, the temperature $T$ is held constant. In $(NVT)$ simulations the volume of the system $V$ is held constant, allowing the pressure $P$ to fluctuate, while the inverse is true for $(NPT)$ simulations.

Most quantities of interest may be measured in both ensembles. However, the presence of multiple phases can complicate the calculation of some quantities,

such as the equation of state. The Gibbs' Phase Rule[84] helps determine which ensemble avoid phase coexistence:

$$f = c - p + 2$$

where $f$ is the number of intensive variables, $c$ is the number of components, and $p$ is the number of phases. In the $NPT$ ensemble, there are two intensive variables, $P$ and $T$, reducing the equation to $p = c$. Thus, for a single component system, there may only be one phase. The $NVT$ ensemble only has one intensive variable, meaning that $c + 1 = p$, resulting in the possibility of phase coexistence. Because $P$ is intensive and $V$ is extensive, only one phase may be present in $NPT$ ensembles. Unless noted otherwise, I use the $NPT$ ensemble throughout this thesis to avoid phase coexistence.

### 2.1.3 Reduced Pressure

It is common practice to used so-called reduced units rather than SI units in simulation[39] for reasons of simulation efficiency, portability across simulation systems, and ease of variable manipulation[89]. The only reduced unit of note in this work is reduced pressure, $P^*$. This pressure is typically reported as $\beta P\sigma^2$ for two-dimensional systems and $\beta P\sigma^3$ for three-dimensional systems. $\sigma$ is a length-scale of interest, resulting in the $\sigma^n$ term accounting for volume. In this work, all values of $\sigma^n$ are the volume of the nanoparticle unless otherwise noted, and $\sigma^n \equiv 1$, unless otherwise noted.

Conversion between reduced pressures is straightforward: to compare a reported reduced pressure with another, choose one to be the "reference" system, and the

other to be converted. Then, compute the value for $\sigma^x$ in the system to be converted. Multiply through to obtain:

$$P_2^*(1) = \beta P \sigma^n(1)$$

For example, in Chapter 5, systems of polyhedron derived from cubes are studied. As noted, in this work $\sigma^3 \equiv 1$; a previous study of a related system[91] defines $\sigma^3$ differently, but in the units used in this work, $\sigma^3 = 64$. Therefore, any value of $P^*$ reported in that work can be converted to the units in this work *via*

$$P^* = 64\beta P$$

It should be noted that systems of hard spheres are known to exhibit fluid-solid coexistence at a reduced pressure of $11.43 \leq P^* \leq 11.57$[89,94–100].

## 2.2 Correlation Functions

Generally, a correlation function accounts for the distance over which some quantity is correlated. The quantity of interest may be as simple as the position or orientation of a nanoparticle, or more complex order parameters, such as those in Section 2.4.

### 2.2.1 Radial Distribution Function

The most common of the correlation functions is the pair correlation function, known as the radial distribution function[84]:

$$g^2(r) = \sum_i^N r_j - r_i = g(r)$$

The radial distribution function encodes the relative probability of finding two particles a distance $r$ apart. Not only does this provide one method of identifying structures present in the system, it also allows for the computation of relevant

thermodynamic quantities in simulated systems. One quantity is the *potential of mean force*, a potential accounted for the average attraction and repulsion in the system, resulting in the particle separations found in the system.

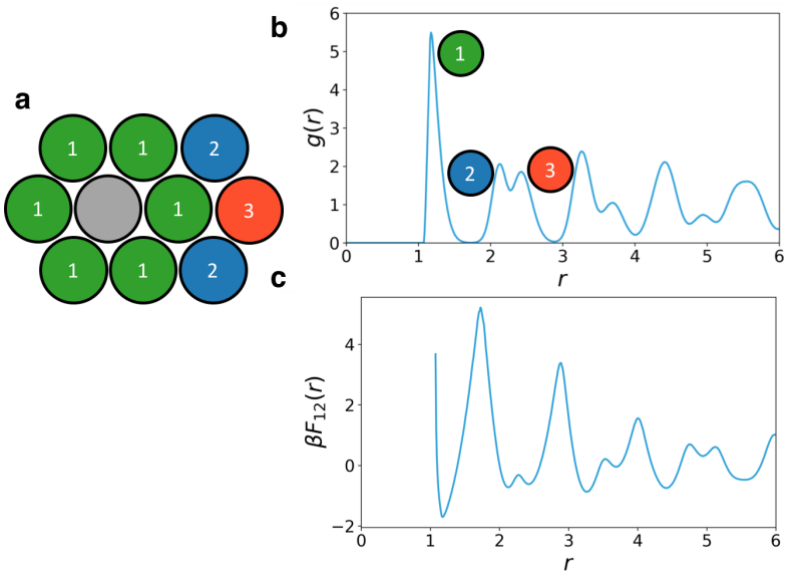


Figure 2-1 **a** schematic of the perfect hexagonal crystal for hard disks, with 1st, 2nd, and 3rd nearest-neighbor positions labelled. **b** Radial distribution function of a system of hard spheres at $\phi = 0.75$, a low-density solid phase. The $g(r)$ shows distinct structural features associated with the hexagonal lattice. **c** the potential of mean force, obtained *via* $\beta\Delta F_{12}(r) = -\ln\big(g(r)\big)$.

The radial distribution function is well-suited for isotropic systems, but cannot capture all the relevant information for anisotropic systems. The radial distribution function must be extended to account for both positions and orientations.

## 2.3 Potential of Mean Force and Torque

If the distances between particle pairs can be accounted for, why not the relative positions of the particles using $(x, y, z)$ coordinates? If so, what new information does that provide? By leveraging the power of statistical mechanics, we can relate the probability of a given distribution of particles with the free-energy of the relative configuration of those particles[60,82]:

$$\beta\Delta F_{12}(\Delta\xi_{12}) = -\ln\Big(H\big(d(\Delta\xi_{12})\big)\Big)J(\Delta\xi_{12}) + \beta\Delta\tilde{F}_{12}(\Delta\xi_{12})$$

$\Delta\xi_{12}$ accounts for the relative position and orientation of a pair of particles $i, j$; $\Delta F_{12}$ is the relative free-energy for the pair of particles; $H\left(d(\Delta\xi_{12})\right)$ uses the Heaviside step function to account for overlapping particles; $J(\Delta\xi_{12})$ is the Jacobian for the coordinate system of choice, and $\Delta\tilde{F}_{12}$ is the free-energy of the "sea particles" (all other particles in the system). In this way, we can see how the shifting of entropy density results in the lowering of the free-energy of the system, directing local and therefore global self-assembly.

Because the Potential of Mean Force and Torque (PMFT) is an extension of the RDF, the algorithm is implemented in much the same fashion. Once computed, the PMFT can be visualized and understood like any other free-energy landscape. The choice of coordinate system to compute the PMFT is very important, however. Take the following example of the PMFT for a system of hard hexagons in the solid phase ($\phi = 0.75$):

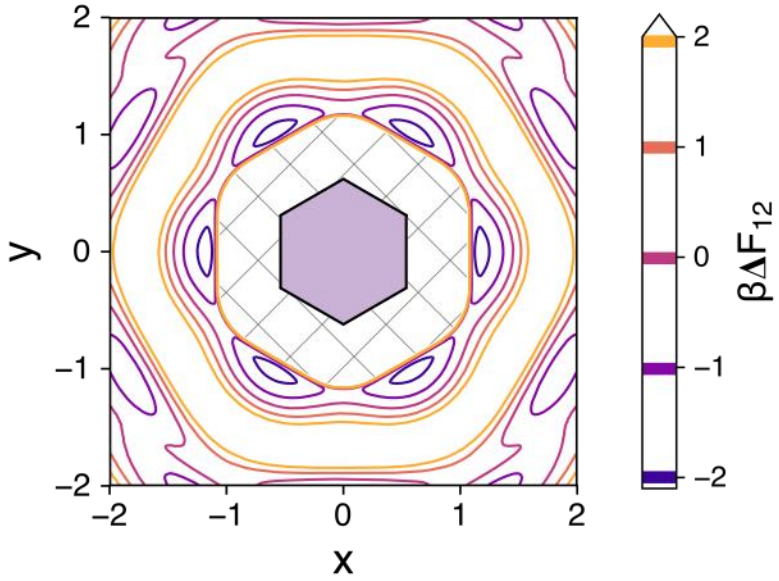


Figure 2-2 Potential of mean force and torque in two-dimensions $(x, y)$ computed for a system of hard hexagons at a density of $\phi = 0.75$. Regions of low-energy correspond to regions of high entropy density, representing the most probably local motifs.

Computing the PMFT in two-dimensions (Figure 2-2) integrates over the orientation of the paired particle $j$. To fully account for the positions and orientations of particles in two-dimensions, a three-dimensional coordinate system must be employed (Figure 2-3):

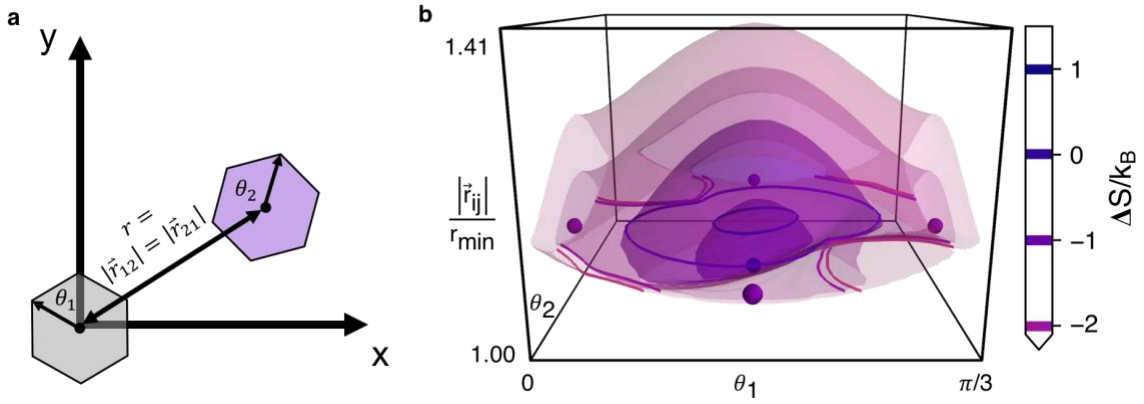


Figure 2-3 **a** Schematic explaining the relationship between the two-dimensional and three-dimensional coordinate systems $(x, y)$ and $(r, \theta_1, \theta_2)$. **b** The same system plotted in Figure 2-2 plotted in the three-dimensional coordinate system.

This three-dimensional coordinate system fully accounts for and can differentiate between the local geometries shown in Figure 2-3. I focus on two-dimensional physical systems and their two- and three-dimensional PMFTs because they exhibit the same physical behavior as three-dimensional physical systems without the added complexity of the third dimension. Note that three-dimensional systems, such as hard polyhedral, would require 6 dimensions to fully account for position and orientation: movement along and rotation about the $x, y, z$ axes. Like any other free energy measurement methods, the PMFT gives a difference in free energies. Thus, the choice of the base energy is critical if PMFTs are to be compared. I employ the ideal gas distribution as a natural zero-point for the PMFT, just as in the RDF: $\lim_{r \to \infty} \beta \Delta F_{12} = 0$.

### 2.3.1 Free-Energy Landscape Analysis and Disconnectivity Graphs

The PMFT can be interpreted as an entropy density distribution or as a free-energy landscape in the coordinate system of choice, much like the energy landscapes for molecules in modern DFT[101,102]. Just as free-energy landscapes from DFT can be analyzed to determine bond strength and location, so too can the free-energy landscapes obtained from PMFTs. The computed PMFT takes the form of a histogram, which can be interpreted as an image composed of either pixels (2D, shown in Figure 2-2) or "voxels" (3D, shown in Figure 2-3). While image analysis is a field full of new and compelling research problems, the relatively well-behaved landscapes that come from PMFT calculations allow for robust analysis and segmentation into free-energy basins through the use of the watershed cut method[103,104] (shown in Figure 2-4).

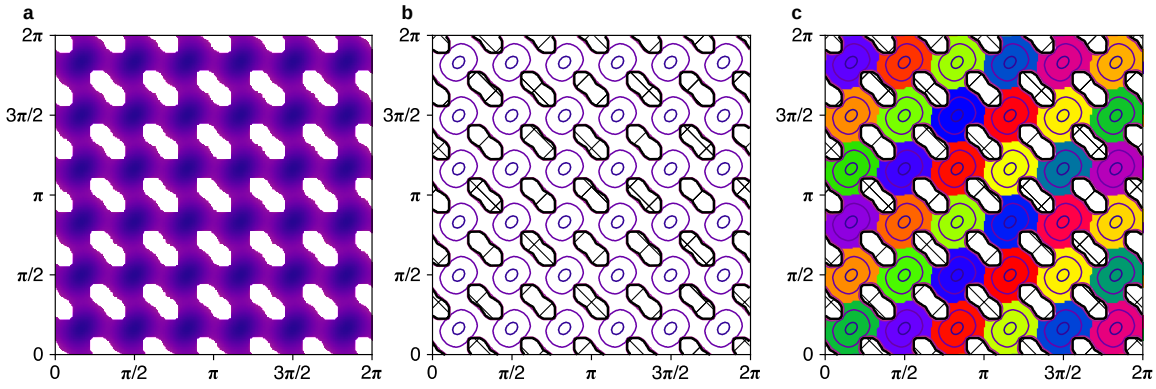


Figure 2-4 Summary of the entropic bond analysis pipeline: **a** The raw PMFT is passed through a Gaussian blur **b** (rendered here as contours) to remove any noise or artifacts before passing into the image segmentation algorithm **c**. The full range of the PMFT is shown: $\theta_1, \theta_1 \in [0, 2\pi]$, showing the 36 identical entropic bonds in systems of regular hexagons. Due to the periodic nature of these PMFTs, all other PMFTs shown in this these display a single periodic region e.g. $\theta_1, \theta_1 \in \left[0, \frac{\pi}{3}\right]$ for regular hexagons.

Automated image segmentation is required to reliably identify the different entropic bonding states. Watershed image segmentation[103,104] is well-suited to this application because it assigns each pixel/voxel of an image to a region

associated with an entropy-density maxima/free-energy minima by ``flooding'' the free-energy landscape starting at free-energy minima until these flooded regions meet, giving each pixel/voxel a unique label associated with a given minimum. As shown in Figure 2-4, the raw PMFT is analyzed to produce a mapping of each discrete geometric configuration to a unique bond. This mapping may then be used to render individual bonds, or track particle geometry during a simulation to compute bond lifetime distributions. Though watershed image segmentation is capable of automatically segmenting the image into different regions (bonds), the sckit-image implementation[104] used is most robust when given the approximate locations of the minima as determined by the lattice positions of the hard hexagons/elongated rhombs. Watershed image segmentation has the added benefit of providing information about the boundaries between bonds, allowing for identification of transition states between minima *via* network analysis techniques.

### 2.3.2 Disconnectivity Graphs

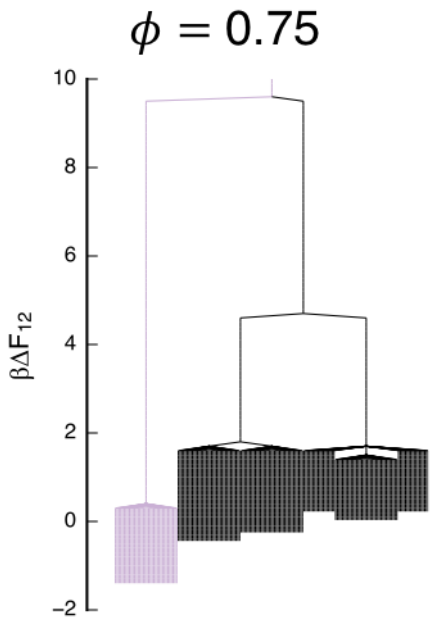


Figure 2-5 Example disconnectivity graph for a system of hard hexagons at $\phi = 0.75$ (free-energy landscape shown in Figure 2-3). Each leaf represents a free-energy basin, while each connection represents a transition-state energy required to be traversed to reach a connected leaf. Here, the purple leaves are the 36 nearest-neighbor configurations for hexagon systems, while the black leaves represent 2nd, 3rd, and 4th nearest-neighbor.

By creating a network from the free-energy minima and transition states, a *disconnectivity graph* can be constructed[105–107]. Such a graph reduces an $N$-dimensional energy landscape to a two-dimensional graph, allowing for connections between free-energy minima and their transition states to be visually analyzed. This is important as the "raw" PMFTs are relatively difficult to understand by eye, especially PMFTs in full $(r, \theta_1, \theta_2)$ coordinates rather than in local $(x, y)$ coordinates. Disconnectivity graphs deliver important insight into the ability for particle pairs to reconfigure in the dense fluid phase. Additionally, the use of disconnectivity graphs as an effective means to analyze PMFTs extends to the analysis of the six-dimensional PMFTs required to analyze systems of three-dimensional particles.

## 2.4 Order Parameters

Generally, and order parameter describes the degree of order or broken symmetry in a system[84]. Order parameters are especially useful to observe across phase transitions as can allow for phase identification as well as identify the kind of phase transition observed. Here a few order parameters used throughout this work are described in detail.

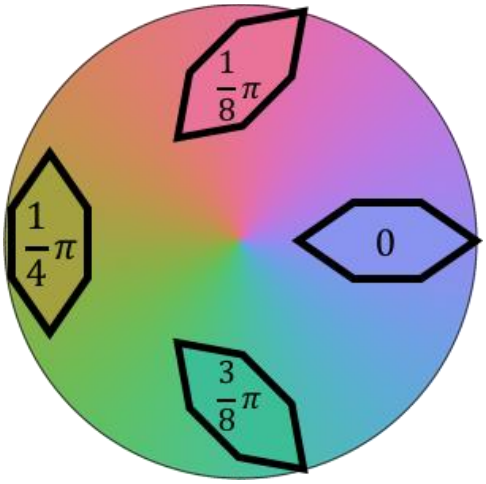


Figure 2-6 Cube ellipse color map[108], with two-fold symmetric hexagon to illustrate how the continuous colormap facilitates orientational analysis. This color map is used throughout this work for angle and orientation-related quantities.

### 2.4.1 Body orientation Order Parameter

For a two-dimensional system composed of particles with $k$-fold symmetry, the body orientation order parameter[108]

$$\xi_k^i = e^{\mathbf{i}k\theta_i}$$

accounts for the orientation of a particle with its symmetry. The orientation of a particle, $\theta_i$, is the angle that a particle in its local reference frame is rotated by into the global coordinate system of the simulation, as shown in Figure 2-7.

$$\theta_6^i = \theta(\xi_6^i) = \theta\left(e^{\mathbf{i}6\theta_i}\right)$$

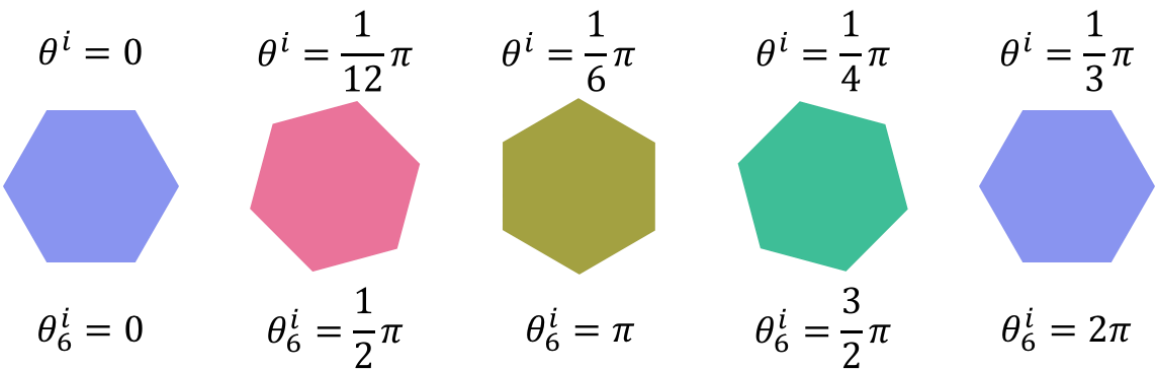


Figure 2-7 Use of the body orientational order parameter to color a hexagon by its orientation, as shown for 5 different orientations: **a** $\theta_6^i = 0$; **b** $\theta_6^i = \frac{1}{2}\pi$; **c** $\theta_6^i = \pi$; **d** $\theta_6^i = \frac{3}{2}\pi$; **e** $\theta_6^i = 2\pi$. Note that the entire color wheel is traversed in the equivalent of $\theta^i = 0 \rightarrow \frac{\pi}{3}$, due to the 6-fold symmetry of the body orientation order parameter.

### 2.4.2 Hexatic Order Parameter

In two-dimensional systems, the development of positional order[109,110] of nearest neighbor particles is an appropriate order parameter. The x-atic order parameter[108,109,111], $\psi_{k,n}^i$, is given by (also see Figure 2-8 and Figure 2-9):

$$\psi_{k,n}^i = \frac{1}{n}\sum_{j \in NN(i)} e^{\mathbf{i}k\theta_{ij}}$$

This order parameter accounts for the orientation (relative to the reference vector $\vec{v}_{\text{ref}} = (1,0)$) of the vector connecting particle $i$ to a particle $j$ in its $n$ nearest-neighbors: $j \in NN(i)$. $k$ accounts for the $k$-fold rotational symmetry of a particle, which is $k = 6$ for the *hexatic* order parameter.

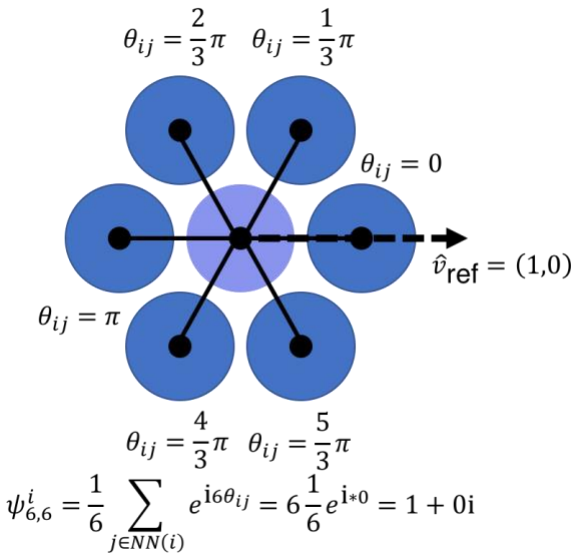


Figure 2-8 Hexatic order parameter calculation for a disk surrounded by 6 neighbors. The angle used in the computation of the order parameter is the difference between the interparticle vector (solid black line) and the reference vector, $\hat{v}_{\text{ref}} = (1,0)$ (dashed arrow). In this example, the neighbors are perfectly oriented in hexatic order, so that the magnitude of order parameter is 1: $\left|\psi^i_{6,6}\right| = 1$, while its orientation is $\theta_{\psi^6} = \theta(\psi) = 0$. Changing the reference vector to an arbitrary $\hat{v}_{\text{ref}} = (x, y)$ will change the complex hexatic orientation, $\theta_6$, but not the magnitude of the hexatic order parameter.

Accounting for this quantity as a complex number allows for the orientation and the strength of the order parameter to be computed per-particle. This aids in visualization of systems of particles, showing regions of hexatic order[109,110], as well as in identifying regions of defects. The average of the hexatic order parameter may also be computed as both a complex and a real number, delivering the direction and strength of the order parameter, allowing for the hexatic phase transition to be identified[109,110].

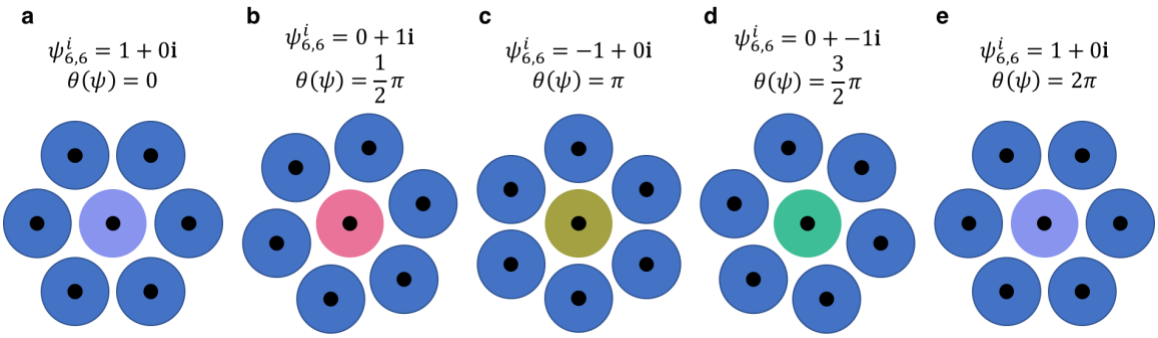


Figure 2-9 The complex orientation of the hexatic order parameter, $\theta_{\psi^6}(\psi_{6,6}^{i})$, allows individual particles to be colored by the orientation of their nearest-neighbors, as shown for 5 different orientations: **a** $(\theta(\psi)) = 0$; **b** $(\theta(\psi)) = \frac{1}{2}\pi$; **c** $(\theta(\psi)) = \pi$; **d** $(\theta(\psi)) = \frac{3}{2}\pi$; **e** $(\theta(\psi)) = 2\pi$. Note that the entire color wheel is traversed in the equivalent of $\theta^{i} = 0 \rightarrow \frac{\pi}{3}$, due to the 6-fold symmetry of the hexatic order parameter.

### 2.4.3 Orientation-Orientation "Hexatic" Order Parameter

An alternative hexatic order parameter[112] that takes into account the difference in orientation between neighboring particles can be computed as

$$\Psi_{k,n}^{i} = \frac{1}{n}\sum_{j \in NN(i)} \cos(k\theta_{ij})$$

In this case, $\theta_{ij}$ is not the angle of the interparticle vector, but rather the difference in orientations of particles $i, j$. As with the traditional hexatic order parameter, the orientation-orientation hexatic order parameter can be computed per-particle or averaged across the system as a whole, allowing for the detection of phase transitions. This particle order parameter is particularly useful in identifying the onset of random tiling phases, which a hexatic order parameter or orientation order parameter would fail to detect.

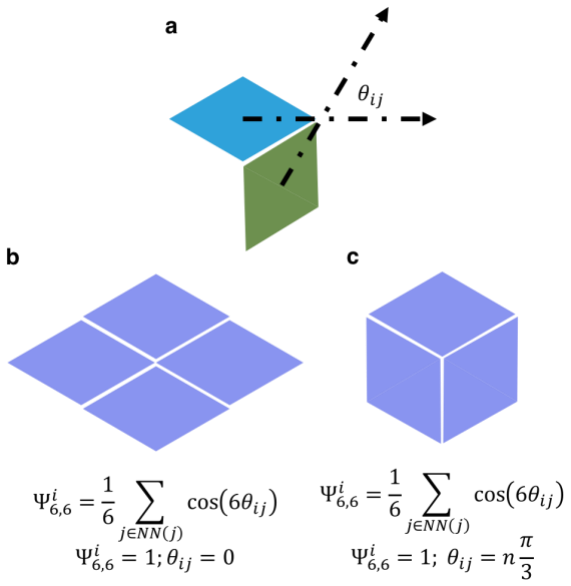


Figure 2-10 Schematic demonstrating the computation of the orientation-orientation hexatic order parameter. Rather than take the orientation of the vector between two particles, as in 2.4.2, the difference in particle orientation **a** provides the input for the computation of the order parameter. While such an order parameter does not distinguish between the **b** parallel and **c** rhombille phases, it distinguished them from a disordered fluid, useful in identifying disorder to order transitions.

### 2.4.4 Cubatic Order Parameter

The orientational order of three-dimensional shapes (polyhedra) must be taken into account, as with two-dimensional shapes. The nematic order parameter is one order parameter which does so, typically used to measure the degree of alignment of long, anisotropic particles in liquid-crystalline phases[113–115]. In this work, the *cubatic* order must be measured, referring to the alignment of a particle with the faces of a cube.

Previous research[33,90,91] utilized a Lagrange Polynomial to account for this order

$$P_4(\cos\theta) \equiv \sum_i \frac{(35\cos^4\theta_i - 30\cos^2\theta_i + 3)}{8}$$

where $\theta_i$ is the angle between the global cubatic director and the particle orientation. This $P_4$ order parameter does not account for true cubatic order, but rather accounts for order around the poles and equator of a sphere (Figure 2-11).

The true cubatic order parameter requires the use of fourth-order tensors to fully account for particle orientation[113].

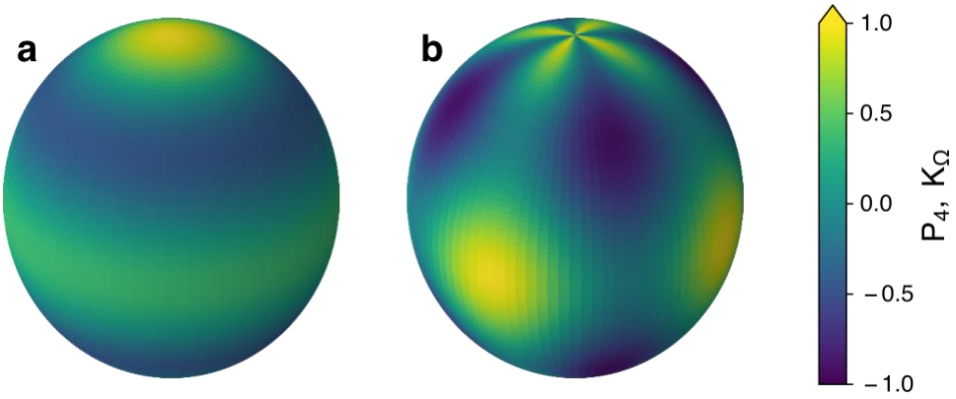


Figure 2-11 Renderings of **a** Legendre polynomial- $(P_4)$ and **b** 4th-order tensor-based $(K_\Omega)$ cubatic order parameters. The value of the order parameter is a function of the relative orientation of a particle to the orientation of the cubatic director. In this example, the cubatic director is oriented in the $(1,0,0),(0,1,0),(0,0,1)$ (toward the bright spots in **b**). The value of the order parameter is then given by the point at which the orientation director of a particle passes through the sphere. Dark regions correspond to low values of the order parameter, while bright regions correspond to high value of the order parameter. Note the difference in order parameter value for polar and equatorial orientations in the Legendre polynomial based order parameter, as well as the delocalization around the equator. The 4th-order tensor is able to properly distinguish cubatic order in a system of particles.

Coloring individual particles by $K_\Omega$ enables the identification of particles in alignment with the cubatic director, or are defective in an ordered structure. Unlike the hexatic order parameter, both the $P_4$ and $K_\Omega$ compare an individual particle's orientation to that of a global cubatic director, rendering these methods unsuitable for identification of individual grains in a polycrystalline system.

## 2.5 Pair motif analysis

In Chapter 4, I analyze the motifs preferred by particle pairs in the dense fluid phase. An anisotropic particle is defined by its position and its orientation, $(\vec{v}_i, \vec{q}_i)$, where $\vec{v}_i$ is a vector to particle $i$, while $\vec{q}_i$ is a quaternion representing the orientation of particle $i$. For a pair of particles, $(i,j)$, we can express the relative position of $j$ to $i$ with the inverse quaternion operation:

$$\vec{r}_{ij} = \vec{r}_j - \vec{r}_i$$

$$\vec{r}_{ij,\text{local}} = \vec{q}_i^* \cdot \vec{r}_{ij} \cdot \vec{q}_i$$

$$\hat{v}_{ij} = \frac{\vec{r}_{ij,\text{local}}}{\left|\vec{r}_{ij,\text{local}}\right|}$$

We can also express the relative orientation of particle $j$ to particle $i$ as a unit vector in a similar fashion:

$$\hat{u}_{ij} = \vec{q}_i^* \cdot \vec{q}_j \cdot (0,0,1) \cdot \vec{q}_j^* \cdot \vec{q}_i$$

By computing $\hat{v}_{ij}$, $\hat{u}_{ij}$ for a pair of particles, we obtain four unit vectors that may be combined to analyze the pair motifs in $\mathbb{R}^{13}$: $\left(\left|\vec{r}_{ij,\text{local}}\right|, \hat{v}_{ij}, \hat{u}_{ij}, \hat{v}_{ji}, \hat{u}_{ji}\right)$. Analysis of a vector in $\mathbb{R}^{13}$ provides a challenge, especially since native visualization of $> 3$ dimensions is impossible. Instead, I employ machine learning methods to reduce the dimensionality of this vector, taking a vector in $\mathbb{R}^{13} \rightarrow \mathbb{R}^2$. I then employ machine learning-based clustering techniques to identify similar pair motifs. Please see Figure 2-12 for examples of this analysis method.

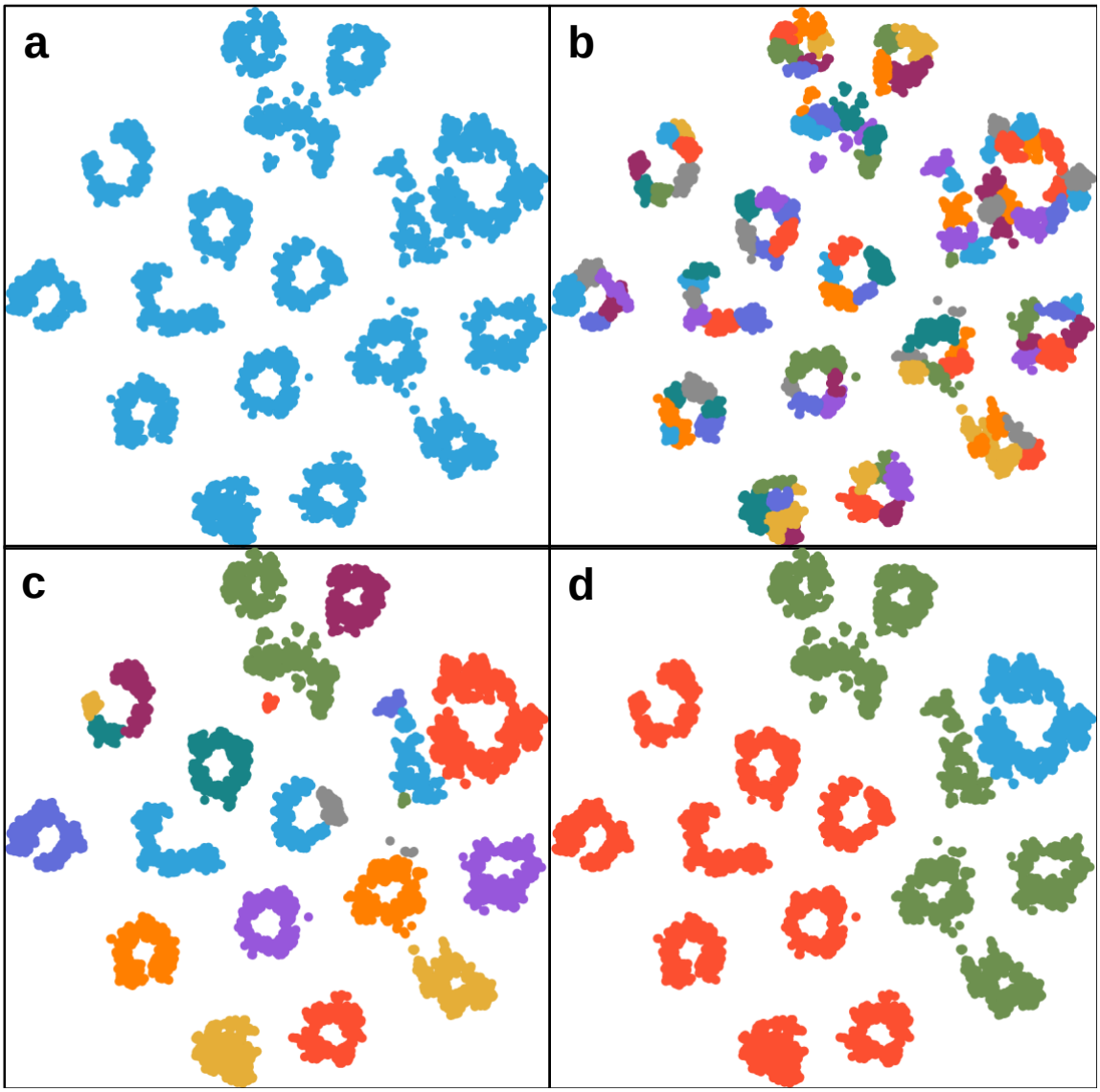


Figure 2-12 Example of **a** the t-SNE distribution of the fluid-phase pair motifs for a system of hard hexagonal-face polyhedra. This distribution is **b** split into clusters using Gaussian Mixture Models (120 different clusters), which are then **c** merged to create clusters with a high probability of containing similar motifs (24 clusters). These clusters are then **d** categorized into three different motifs.

### 2.5.1 t-Distributed Stochastic Neighbor Embedding (tSNE)

The analysis of vectors in $\mathbb{R} > 3$ is inherently difficult due to the difficulty in visualizing more than three dimensions. Machine learning provides a class of methods that reduce the dimensionality of a data set. In particular, the t-distributed stochastic neighbor embedding (t-SNE)[116–118] provides a powerful method to embed a high-dimensionality distribution in a lower dimension. The t-

SNE is particularly useful as it retains the proximity of points in the higher-dimension in the lower-dimensional embedding. The t-SNE does this by considering the higher-dimensional datapoints, $\vec{X}_i$, and computing the probabilities that two of these datapoints are neighbors. It then creates a mapping from the higher-dimensional data, $\vec{X}_i$, to a lower dimension, $\vec{x}_i$ while retaining the neighbor probabilities. The usage of the Student-t distribution allows this method to spatially separate dissimilar points in $\vec{x}$. In this thesis, the dimensionality reduction takes vectors in $\mathbb{R}^{13} \rightarrow \mathbb{R}^2$. An example of such a t-SNE in $\mathbb{R}^2$ in shown in Figure 2-12.

### 2.5.2 Gaussian Mixture Models (GMM) Clustering

Many different machine learning techniques exist to cluster vectors. I choose Gaussian Mixture Models (GMM)[119–121] to cluster the t-SNE distribution. GMM as its name suggests, GMMs use Gaussian distributions to cluster points, grouping clusters that have a high probability of being similar. GMMs are very fast, allowing them to be efficient for larger datasets[118]. While Gaussian distributions are convex, they can be adapted to cluster non-convex clusters through the use of cluster merging[121]. This method of cluster merging has previously been used in the machine learning analysis of different crystal structures[119]. I use this combined GMM and Shannon-entropy based merging technique to cluster local motifs that I then label according to motif type. Please see Figure 2-12**b**-**d** for examples of the GMM merging analysis.

## 2.6 Other Analysis Methods

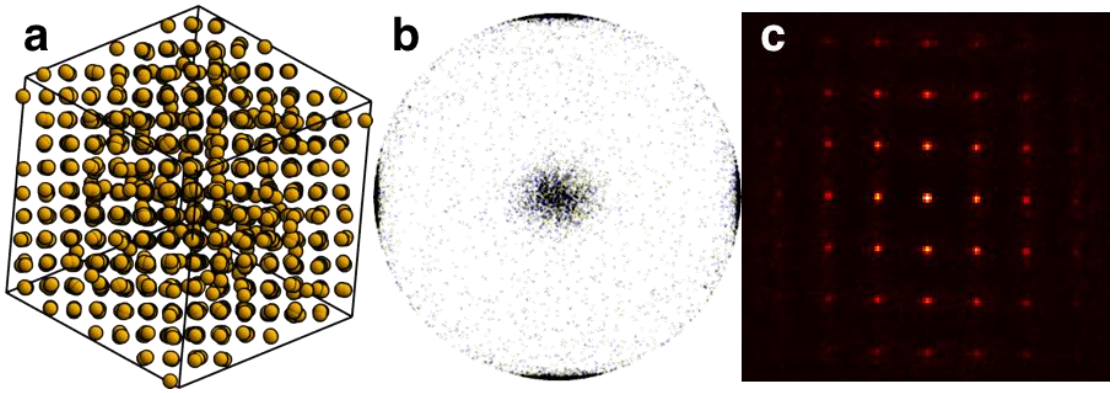


Figure 2-13 **a** Example analysis of a system of polyhedra, represented by spheres. **b** shows the bond order diagram, showing the cumulative positions of the nearest-neighbors of each sphere, while **c** the fourier transform of the positions in **a** delivers a diffraction pattern, showing evidence of long-range translational order by the existence of Bragg peaks. Both **b** and **c** are viewing direction dependent, allowing for powerful crystal analysis and detection.

### 2.6.1"Bond" Order Diagram

In three-dimensional systems, the relative orientation of the nearest neighbors is very useful in identifying the ordering of a system of particles[34], as seen in the computation of the hexatic order parameter in 2.4.2. To quantify the local ordering of the nearest neighbors, the interparticle vector is represented as a dot on the surface of a sphere, where each dot represents the intersection of the bond vector with the surface of the sphere, seen in Figure 2-13 **b**. This kind of plot is known as a "bond order diagram"[34], where a "bond" is simply the vector between a particle $i$ and particle $j$ in the nearest-neighbors of particle $i$: $j \in NN(i)$. These "bonds" are not bonds in the traditional sense, nor are they the entropic bonds defined in this thesis.

### 2.6.2 Diffraction Patterns

Crystallographers rely on x-ray and electron diffraction patterns to identify the crystal structures of experimental systems[122], not only because until recently

atomic resolution microscopy was unavailable, but also because of the robust, unique fingerprint the diffraction pattern provides for a structure. Taking advantage of the mathematical nature of the diffraction pattern i.e. the diffraction pattern is the Fourier transform of the atomic positions, the analogous single-crystal diffraction patterns for assemblies of simulated particles may be computed[34]. These diffraction patterns allow for quick identification of the type of periodic structure present in self-assembled systems (refer to the example in Figure 2-13 **c**).

### 2.6.3 Alluvial Diagrams

Finally, I collapse the "spatial" information encoded in the PMFT into a similar fashion to the disconnectivity plots *via* alluvial diagrams[123]. These diagrams show the flow of quantities from one region to another, most often used to map the change of quantities in large networks. These diagrams show the way in which changing the shape of a particle changes the size of the region in PMFT-space that belongs to a particular entropic bond.

### 2.6.4 Bond Tracking

As discussed in Section 2.1.1, Metropolis MC resembles MD simulation in the Brownian limit. Because of this similarity, it is possible to track particle configurations between simulation frames (an example schematic shown in Figure 2-14). Over the course of an MC simulation, consecutive frames are compared, and each particle pair is assigned a bond from the bond map generated *via* image analysis of the PMFT. By comparing bonds between consecutive frames, the length of time (as measured in MC sweeps) a given pair

is in a given bond is computed. By constructing a histogram from these individual bond lifetimes, the probability distribution of bond lifetimes (Bond Lifetime Distribution) is computed, allowing for comparison of these bonds to those in hydrogen bonding systems (Figure 2-15).

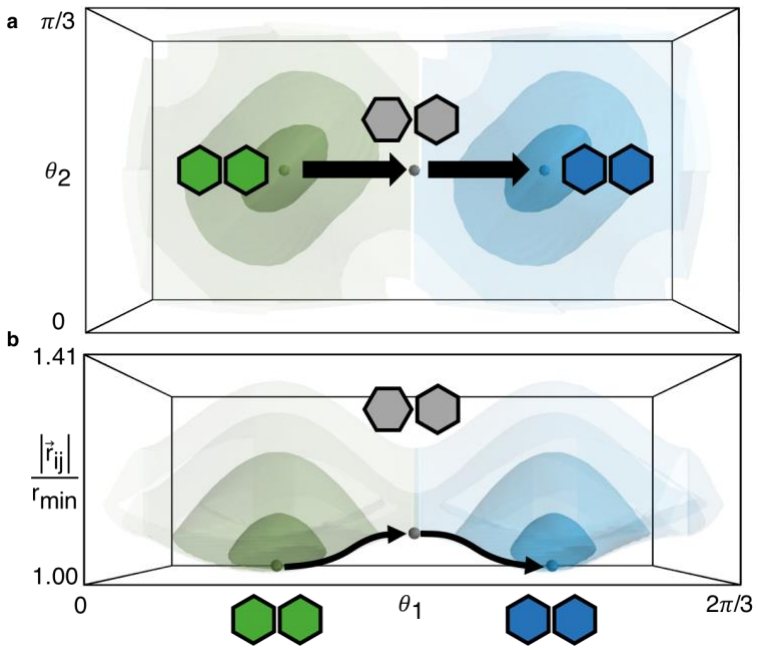


Figure 2-14 Schematic showing a pair of hard hexagons, and their pair configurations (inset) in the $(r, \theta_1, \theta_2)$ PMFT. Two of the minimal PMFTs $\left(\theta_1, \theta_2 \in \left[0, \frac{1}{3}\right]\right)$ are paired, allowing the visualization of a bonding transition from one ground state (green) to another (blue) through a transition state (grey) along a hypothetical reaction coordinate.

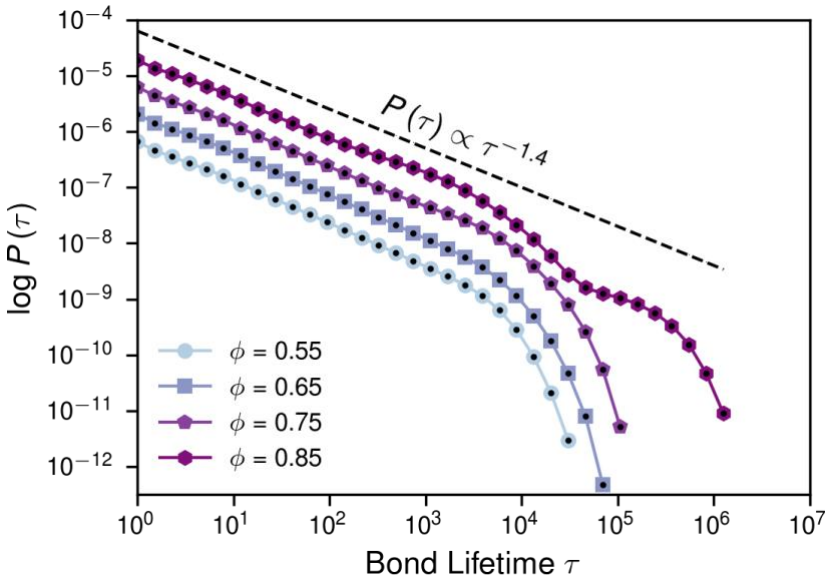


Figure 2-15 Example of a bond lifetime distribution, in this case for four systems of hard hexagons at densities $\phi = [0.55, 0.65, 0.75, 0.85]$. Each curve is separated by a decade for clarity, allowing for identification and analysis of the different features present in the distributions.

## 2.7 Software Packages

### 2.7.1 Simulation: HOOMD-Blue

HOOMD-blue[87,93,124–128], originally an acronym for *Highly Optimized Object-oriented Molecular Dynamics – Blue Edition*, is a powerful simulation engine built to leverage the computing power of graphical processing units (GPUs). HOOMD-blue is currently celebrating its 10th anniversary, and is currently in version 2.1.8. Over the last decade, many improvements to HOOMD-blue were made, including the addition of the *Hard Particle Monte Carlo* (HPMC) module[93]. This module allows users to use HOOMD-blue's powerful scripting interface to run Monte Carlo simulations of polygons and polyhedra, taking advantage of the parallel computing resources available, not only GPUs, but also arrays of CPUs connected with MPI.

### 2.7.2 Analysis: Freud

The systems studied in this work required the development of many analysis routines, including new algorithms and new implementations of existing algorithms. These methods are now collected in a software suite dubbed *Freud*[129,130] after the father of psychoanalysis. The development of this software package and the methods therein constitute a significant portion of the work in this dissertation; indeed, the ability to compute the PMFT would not have been possible without the time and effort spent in implementing it as a part of *Freud*. Additionally, the modular framework of *Freud* enables rapid prototyping and implementation of code, allowing for quick, efficient addition of analysis routines, such as order parameter computation, identification of local motifs, and other useful metrics. *Freud* is still under development, with many users in the Glotzer Group, other groups at the University of Michigan, and at other universities.

### 2.7.3 Other Software

Both HOOMD-blue and Freud inherit from and contribute to the popular python scientific computing community[104,131–135]. In the past decade, Python has become the *de facto* language of scientific computing due to its nature as a scripting language. This allows users to glue together existing computing packages with their own analysis methods, providing an incredibly powerful and flexible analysis environment. Both HOOMD-blue and Freud use NumPy[131,132] as an underlying data structure framework, allowing users to pass-in, extract, and manipulate data as required for their research. This facilitated the computation of PMFTs and allowed for the interoperability between HOOMD-blue and Freud to track hard

particles in entropic bonds. Analysis of entropic bonds would have been impossible without Scikit-image[104,118], a relatively new, and very powerful, image analysis library. The pair motif analysis was enabled by the collection of machine learning methods in Scikit-learn[118]. MatPlotLib[136] and Mayavi[137] provide plotting libraries, again leaning on the scientific python stack. Without these libraries, it would have been much more onerous to even attempt to plot any of the data in this dissertation, let alone gain a deeper understanding into the nature of the entropic bond.

# Chapter 3

# Shape Allophiles Improve Entropic Assembly

*Note: this chapter is adapted from* Shape Allophiles Improve Entropic Assembly[138], *published in* Soft Matter, 2015. *All figures reproduced from Ref. 1 with permission from the Royal Society of Chemistry.*

## 3.1 Introduction

Self-assembly and shape complementarity (allophily) play important roles in many systems, especially biological systems in which the way proteins, enzymes, and DNA fit together geometrical play a critical role in the self-assemble behavior[139–142]. The way in which biological systems fit together in geometric complementary way inspires the investigation of “allophilic” geometries[28,139,143–147], named due to the way in which the geometries are designed to “like” each other. Allophilic particles are designed to fit together like puzzle pieces, creating hierarchical structures. Lock-and-key colloids[28,29,37,148,149] are examples of allophiles as they are designed to exploit shape and entropic depletion forces for self-assembly. Biological systems rely on inter- and intra-molecular forces to guide self-assembly while lock-and-key colloids reach similar assembles solely with entropy. Here I demonstrate the ability for allophilic patterning to direct the self-assembly of a desired structure in a quantifiable manner, *via* analysis of the PMFT into entropic bonds.

## 3.2 Methods

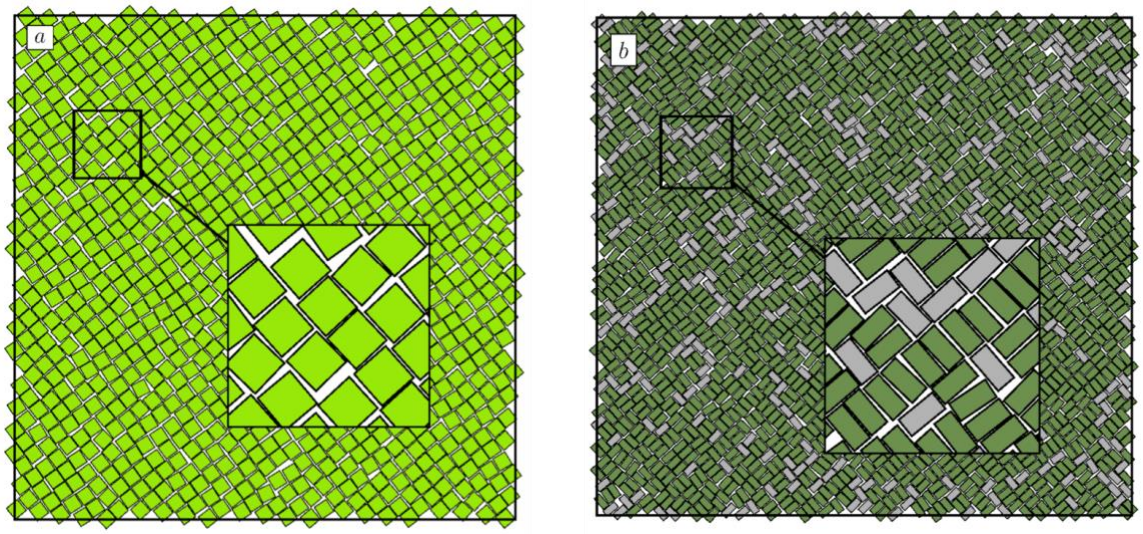


Figure 3-1 Hard squares (*a*) self-assemble a square lattice, while hard 2:1 aspect-ratio rectangles (*b*) instead self-assemble a random tiling (the random domino or parquet tiling).

I start with hard squares, modelled in the *NPT* thermodynamic ensemble, and note that these squares self-assemble a square lattice (see Figure 3-1**a**)[36,150,151]. Taking these squares as “parent” shapes, I choose “child” shapes that combine to form the parent shape, in this case 2:1 ratio rectangles (shown in Figure 3-1**b**) and right-isosceles triangles. Both shapes are ideal for our investigations as neither self-assemble the square lattice: 2:1 hard rectangles self-assemble the random domino (parquet) tiling[90,152,153] (shown in Figure 3-1**b** and detailed in Figure 3-2), while right isosceles triangles do not self-assemble an ordered solid (Figure 3-9**a**).

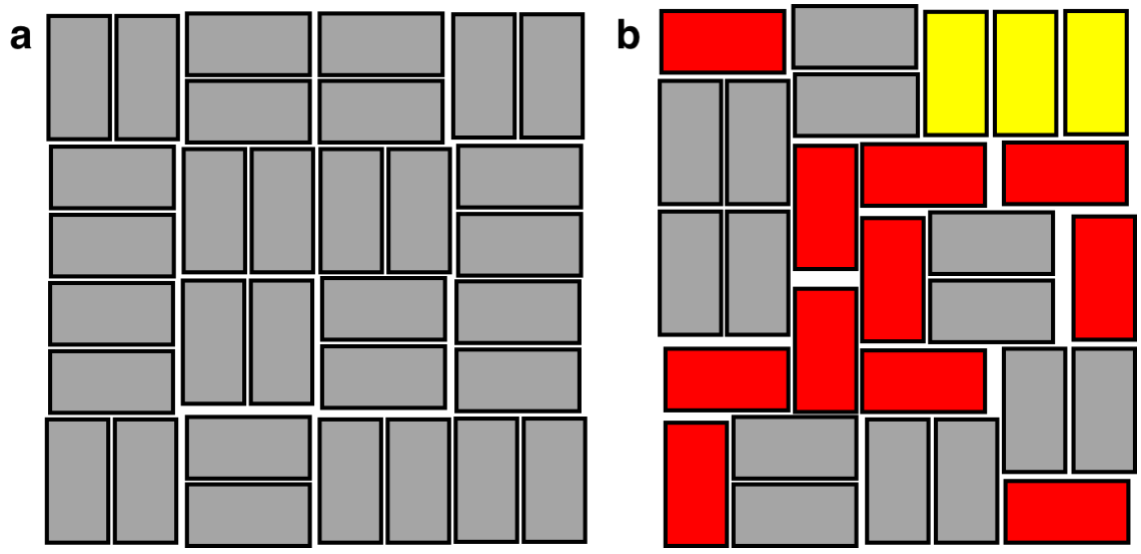


Figure 3-2 Schematic showing the differences in the square lattice **a** and the parquet tiling **b**. Red rectangles represent unpaired rectangles, unique to the parquet tiling, while the yellow rectangles are ambiguously paired. Both are defects in the square tiling.

I pattern the child shapes using triangle waves to create a complementary interface. Triangle waves have two natural variables to tune to optimize self-assembly behavior: amplitude and wavenumber. I allow the amplitude to vary $A = [0, 0.5L]$, reported as a fraction of $0.5L$: $A \in [0,1]$ ensuring the shapes are all simple polygons. The wavenumber, $n_k$, is the number of half wavelengths across the edge of a shape; even wavenumbers create congruent shapes (homophiles) while odd wavenumbers create incongruent shapes (allophiles), shown in Figure 3-3.

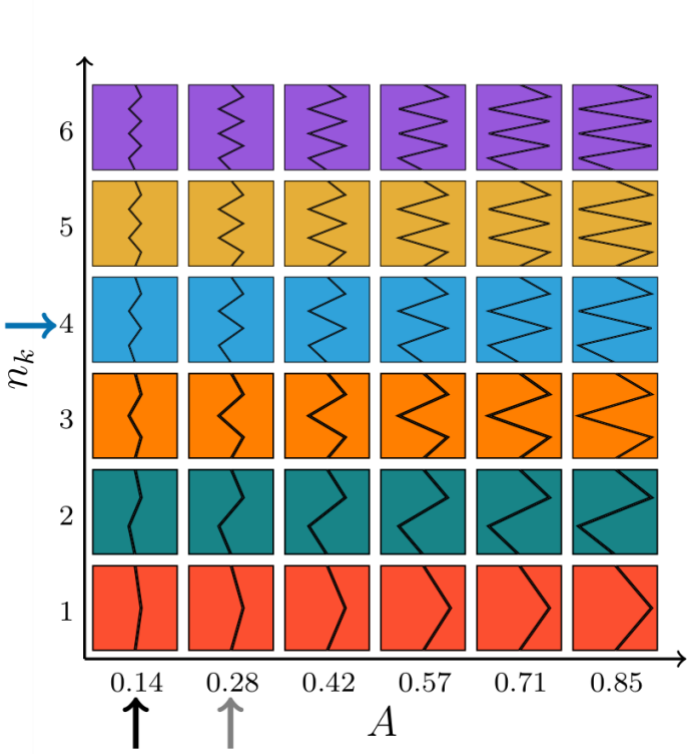


Figure 3-3 Triangle wave patterning is applied to rectangles to create shape complementarity. $A$ is the amplitude of the triangle wave, while $n_k$ is the wavenumber, or the number of half-wavelengths. Only integer values of $n_k$ are considered. Three cuts through this space, $A = 0.14, 0.28; n_k = 4$ are considered in this work.

These systems are simulated in HOOMD-blue[87,93,126] using the HPMC[93] integrator. To compute the orientation correlation function[110,154,155] and the PMFT, I investigate systems of $N = 10{,}082$ particles, simulated with MPI domain decomposition on 32 cores each on the University of Michigan Flux cluster and the XSEDE Stampede computing cluster[156,157].

## 3.3 Results and discussion

I take three cuts through the phase space formed by $n_k$ and $A$: $n_k = 4$ and $A = 0.14, 0.28$. By investigating the assembly propensity and the effects the shape has on the PMFT and entropic bond formation, I can determine design rules to control the self-assembly of shape allophiles.

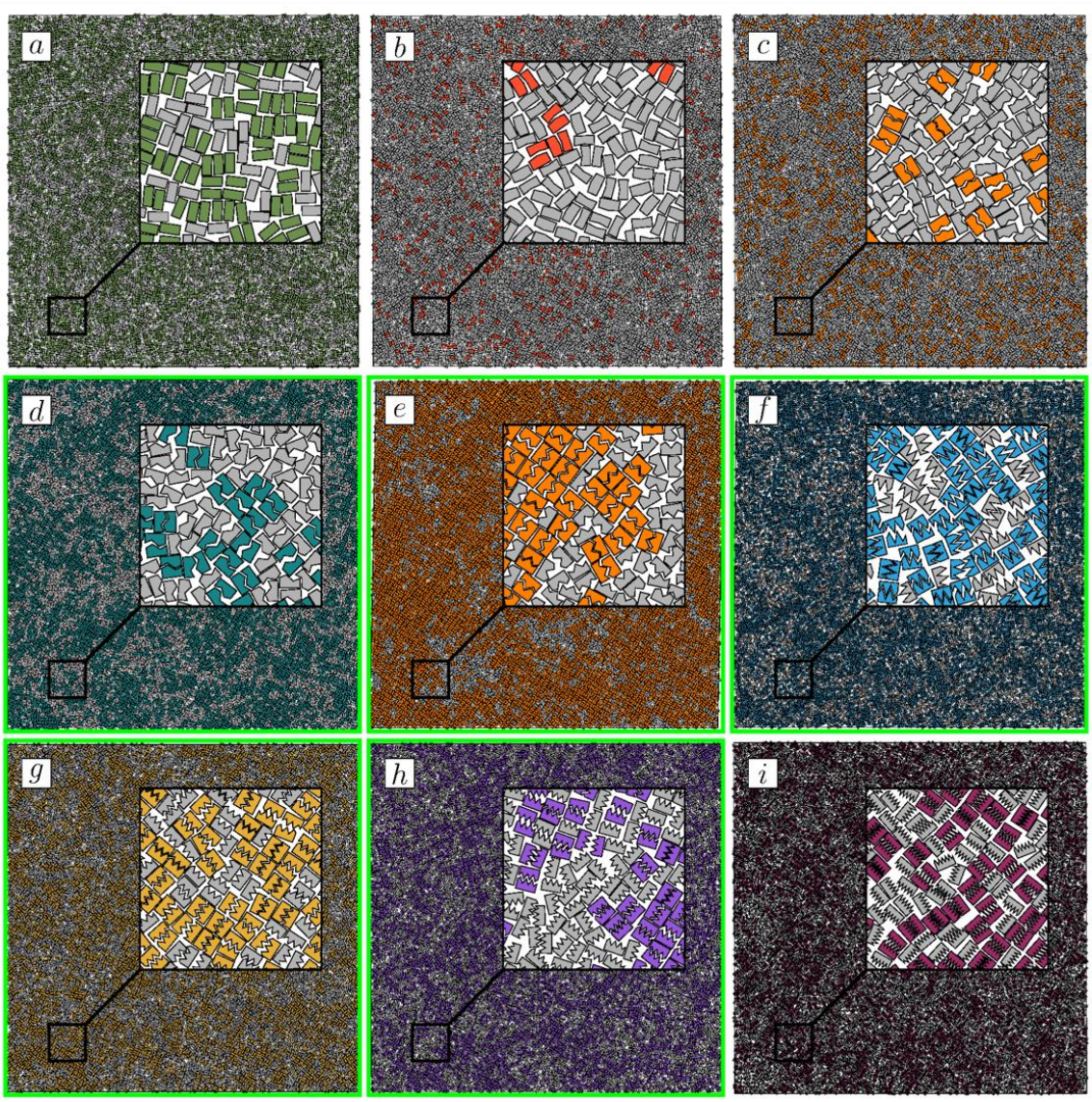


Figure 3-4 Array of the lowest density solid self-assembled equilibrium structures for (*a*) rectangles ($\beta L^2 P = 9.0$) and allophilic rectangles with (*b*) $n_k = 1, A = 0.14$ ($\beta L^2 P = 10.0$), (*c*) $n_k = 3, A = 0.14$ ($\beta L^2 P = 11.8$), (*d*) $n_k = 2, A = 0.28$ ($\beta L^2 P = 12.6$), (*e*) $n_k = 3, A = 0.28$ ($\beta L^2 P = 13.2$), (*f*) $n_k = 4, A = 0.57$ ($\beta L^2 P = 8.0$), (*g*) $n_k = 5, A = 0.28$ ($\beta L^2 P = 11.2$), (*h*) $n_k = 6, A = 0.28$ ($\beta L^2 P = 9.8$), (*i*) $n_k = 10, A = 0.28$ ($\beta L^2 P = 9.2$). Wavenumbers increase left to right, while amplitude increases top to bottom. Bonded shapes are colored as in Figure 3-1; otherwise, they are colored grey. Shapes that improve the assembly of the square lattice relative to 2:1 rectangles are outlined in green. Values for assembly propensity $f_b$, as well as the pressures, are plotted and compared in Figure 3-5.

The first measure of success of allophilic patterning is the fraction of particles that correctly pair, or the assembly propensity of the system. I employ a simple metric to determine assembly propensity: two particles are paired if the distance between them is below a threshold, and if the interparticle vector is within $\theta \approx$

$0.1\pi$ of being perfect. Simple addition of triangle waves is not enough to increase assembly propensity: all $A = 0.14$ are not significantly better than raw rectangles. Additionally, lower values of $n_k$ are ineffective at improving the assembly propensity, actually increasing the number of unpaired particle. However, at larger values of $n_k, A$ the assembly propensity increases to above 70%, indicating successful assembly.

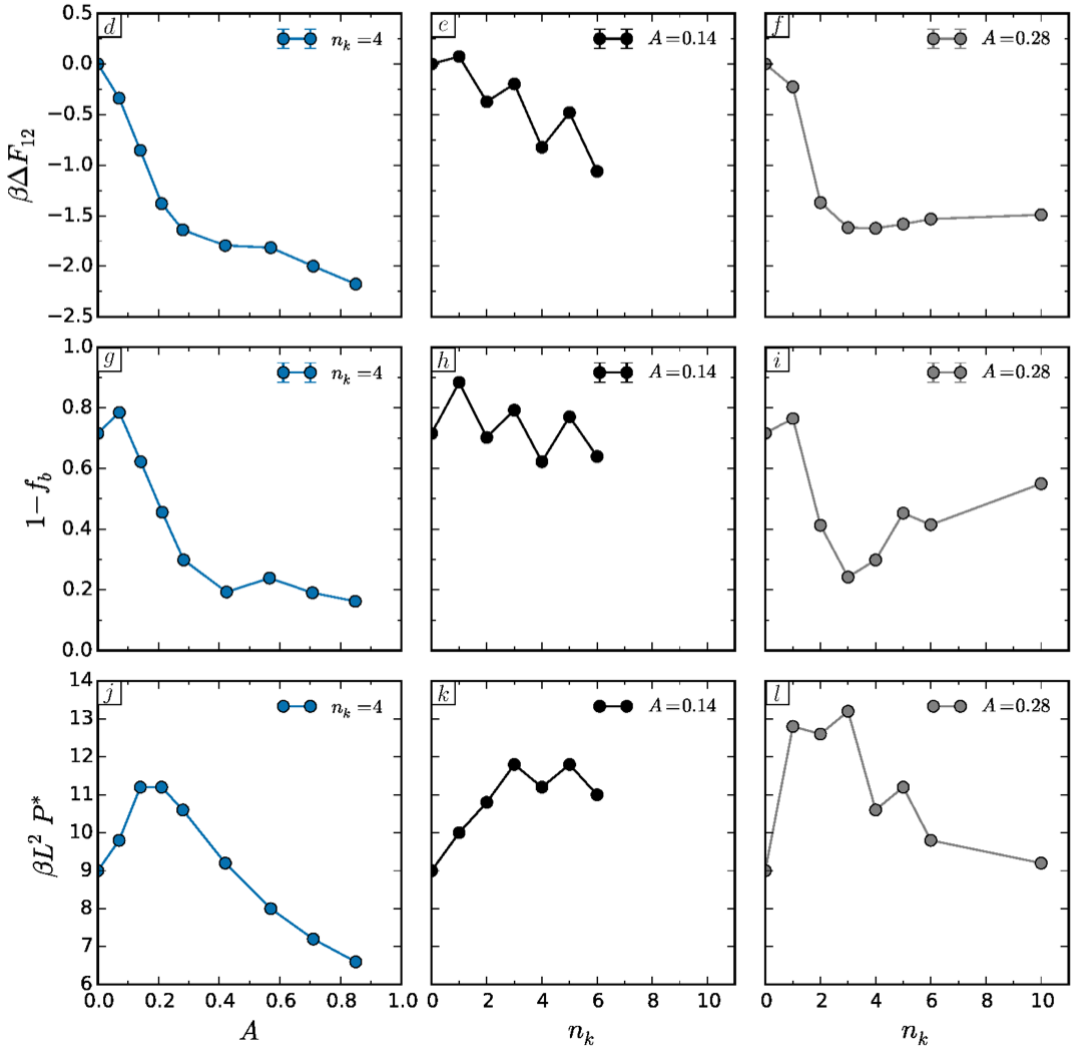


Figure 3-5 Comparison of the relative free-energy of the primary bonding well, $\beta\Delta F_{12}$, the number of defects (complement to the assembly propensity, $(1-f_b)$, and the lowest solid pressure, $\beta L^2 P^*$ at $A = 0.14, 0.28; n_k = 4$. (d and g) show a direct correlation between the increase in the directional entropic force and the increase in properly assembled particles due to an increase in $A$, while (e, f, h, i) show a threshold-like nature of $A$ for the increase in the DEF, as well as the existence of optimal values for $n_k$. Error bars are reported as the standard deviation of the average for 4 replicate simulations at the same state point. Error for (d-f) is $O(0.005)$ while that for (g-i) is $O(0.0005)$, smaller than the size of the markers used. No error bars reported for pressure as pressure is an independent variable in the simulation.

I analyze the 2D PMFT to understand the effect that $n_k, A$ have on the free-energy landscape and resulting bonds. Figure 3-6 shows the free-energy landscape for a 2:1 rectangle and an allophilic rectangle with $n_k = 4, A = 0.42$. The addition of the allophilic patterning has a significant effect on the regions of the landscape that are attractive or repulsive. The edge-to-edge attraction greatly

increases, while the secondary minima associated with the L-shaped motif disappears.

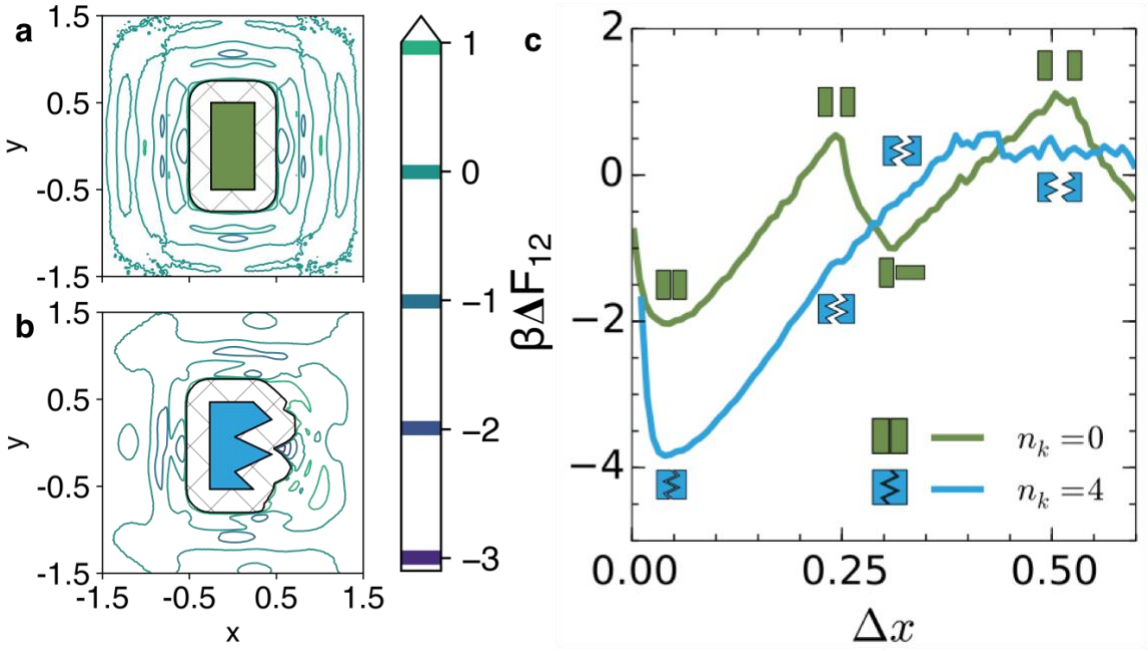


Figure 3-6 2D PMFT for **a** hard rectangles and **b** $n_k = 4, A = 0.42$. **c** cross-sections through the bonding wells ($y = 0$); for convenience $\Delta x$ is the distance from the closest approach of two hard particles. Schematics of the local configurations at each $\Delta x$ included to aid in the understanding of the PMFT. Note the increase in depth of the primary bonding well due to allophilic shaping, as well as removal of the local minima associated with the L-motif in hard rectangles.

The amplitude, $A$, has the strongest effect on the depth of the entropic bonding well, producing a difference in free-energy $\beta\Delta F_{12} > 2$ at the highest amplitudes investigated, shown in Figure 3-5. As $A$ increases, the region associated with the primary bonding well increases in size, eliminating the region associated with the random domino well, effectively biasing the system against the formation of this motif. However, this effect eventually plateaus, due in part to the increased propensity to misbind, shown in Figure 3-7.

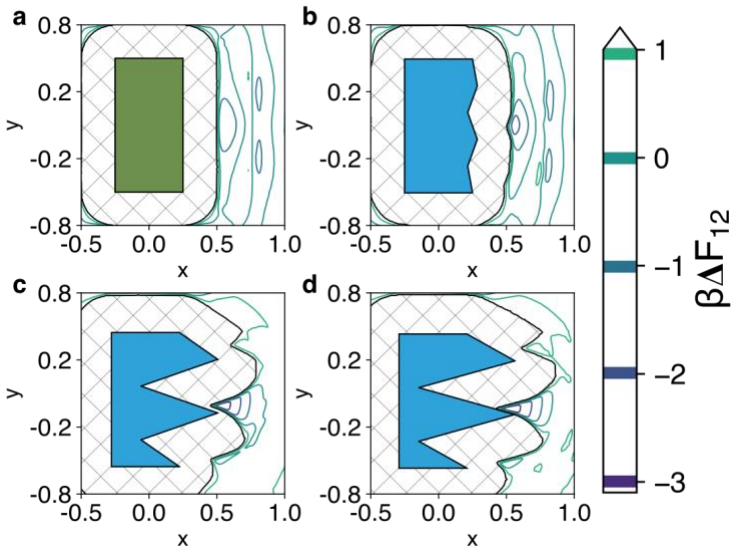


Figure 3-7 PMFTs for **a** $A = 0.42$, **b** $A = 0.57$, **c** $A = 0.71$, and **d** $A = 0.85$ at $n_k = 4$. As the value of $A$ increases, the emergence of secondary bonding wells results in the increase in misbonding, preventing a further increase in $f_b$ that should be expected given the increase in the depth of the bonding well, shown in Figure 3-5.

Interestingly, even and odd values of $n_k$ have little impact on the assembly propensity of allophilic particles once the threshold value for $A$ is met, even though systems with odd $n_k$ only have $\frac{N}{2}$ particles with which to bind. This contradicts intuition, as it is expected that $f_b$ should decrease for odd $n_k$, as observed in particle with a $A$ values below the threshold, shown in Figure 3-5 e, h, k. Instead, past the $A$ threshold, the DEF interactions are strong enough to correctly guide the pairing of complementary particles, so that the decreased number of pairs with which to bind does not play a significant role[73]. In fact, the most successful allophilic value was for $n_k = 3, A = 0.28$, shown in Figure 3-4 and Figure 3-5.

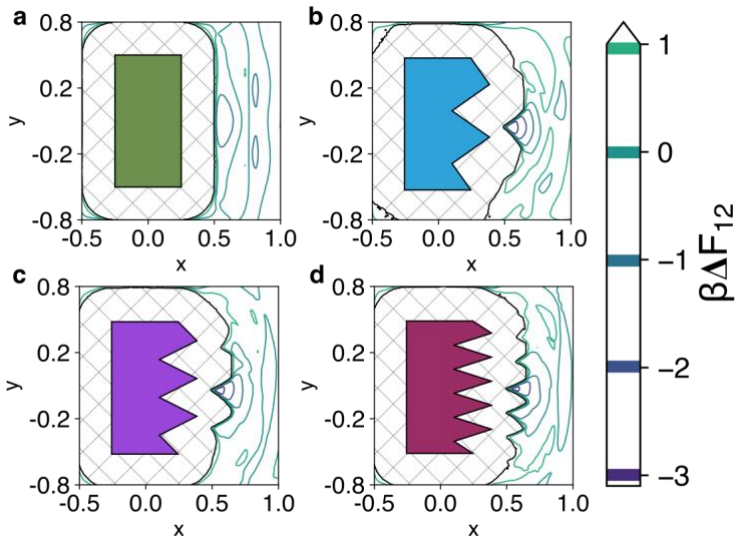


Figure 3-8 PMFTs for **a** rectangles, **b** $n_k = 4$, **c** $n_k = 6$, and **d** $n_k = 10$ at $A = 0.28$. The emergence of the secondary bonding wells in **c, d** indicate that high values of $n_k$ reduce the selectivity of the allophilic patterning. The re-emergence of the bonding well associated with the L-motif in **c, d** indicate that the smaller spacing between triangle-wave teeth poorly mimics a flat face, also reducing the effectiveness of allophilic patterning at high values of $n_k$.

As $n_k$ increases past $n_k = 4$, the assembly propensity starts to decrease. Analysis of the PMFTs, shown in Figure 3-8, show the increase in $n_k$ causes the introduction of low-energy bonding wells associated with mispairing of particles. Additionally, the free-energy well associated with the L-motif in hard rectangles begins to reappear, indicating that the close proximity of the "teeth" can poorly mimic a flat face, enough to decrease the assembly propensity of the system. After analysis of the PMFTs, I establish the following allophilic design rules:

1. A moderate amplitude is sufficient to induce and entropic drive to self-assemble, $O(15\%)$ of particle size
2. An intermediate wavenumber induces the entropic drive to self-assemble without creating the propensity to misbind, in these systems $A \approx 3{,}4$.

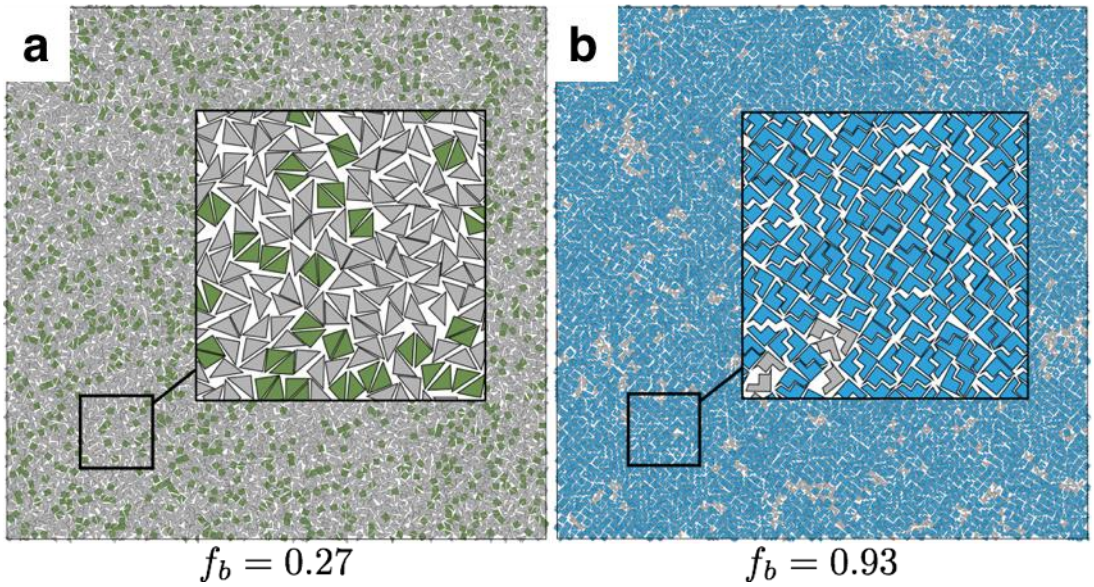


Figure 3-9 **a** right-isosceles triangles do not self-assemble an ordered solid. **b** application of allophilic patterning greatly increases the ability for the system to self-assemble the desired square lattice.

I put the design rules to the test on a system of right-isosceles triangles. These triangles do not self-assemble any ordered solid phase, not even a random phase like the 2:1 rectangles. Analysis of the 2D and 3D PMFTs shown significant competition between local motifs to form entropic bonds, especially within the regions corresponding to base-to-hypotenuse configurations.

I add a $n_k = 4, A = 0.28$ triangle wave pattern to the triangle to direct its self-assembly. The effect on the PMFT is pronounced: The primary bonding well is considerably deepened, limiting its ability to convert to other bonds, while the defect configurations are considerably higher in free energy.

When these patterned triangles self-assemble, an assembly propensity of 93% is achieved, indicating the considerable effectiveness of this method.

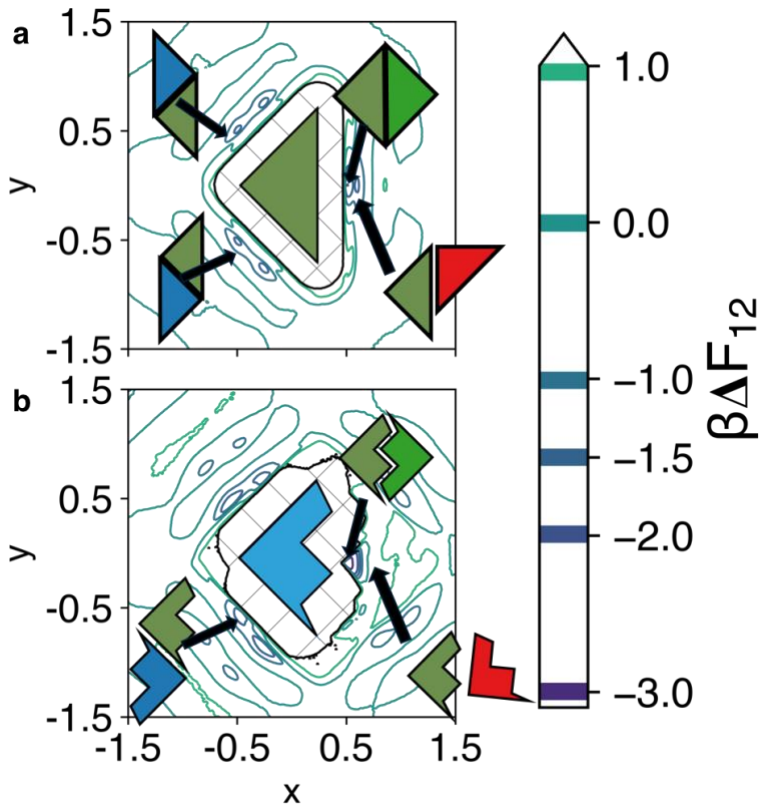


Figure 3-10 Two-dimensional PMFTs for **a** right-isosceles triangles and **b** allophilic triangles with $n_k = 4, A = 0.28$. Right-isosceles triangles have two free-energy wells in close proximity, preventing the successful self-assembly of the square lattice. The defect well disappears with the application of allophilic patterning.

## 3.4 Conclusion

Allophilic patterning is a very effective way to control the self-assembly of hard particles, without requiring the use of chemical functionalization of other intrinsic interparticle interactions. It achieves this by altering the extant entropic bonds in the system to reinforce desired local motifs while discouraging disruptive local motifs. The design of entropic bonds *via* shape modification with allophilic patterning is yet another tool for scientists and engineers to control and self-assembly. Such complementary geometries are likely very important in naturally occurring systems, with feature sizes $O(15\%)$ of particle size able to influence assembly behavior. Additionally, while previous studies not that vertices are

entropically repulsive[60,82,158], they can be effectively attractive through allophilic patterning, allowing for the creation of motifs required for a plasmonic response in anisotropic particles[159,160]. Further investigation into shape complementarity in other, more complex systems should be undertaken to better understand how to best design and control allophilic interfaces.

# Chapter 4

# Hierarchical Self-Assembly of Cube Slices

## 4.1 Introduction

In Chapter 3 I demonstrate how allophilic patterning can control self-assembly by leverage the hierarchical self-assembly of congruent derivatives of squares: 2:1 rectangles and right-isosceles triangles[138]. Neither shape self-assembled a square lattice, instead forming a random tiling (rectangles) or a disordered solid (triangles). By analyzing the emergent directional entropic forces in that system, I can understand and modify its self-assembly behavior. It is natural to then ask a similar question about the hierarchical self-assembly behavior of three-dimensional systems, specifically the extension of the previously considered hard square system, the hard cube (shown in Figure 4-1).

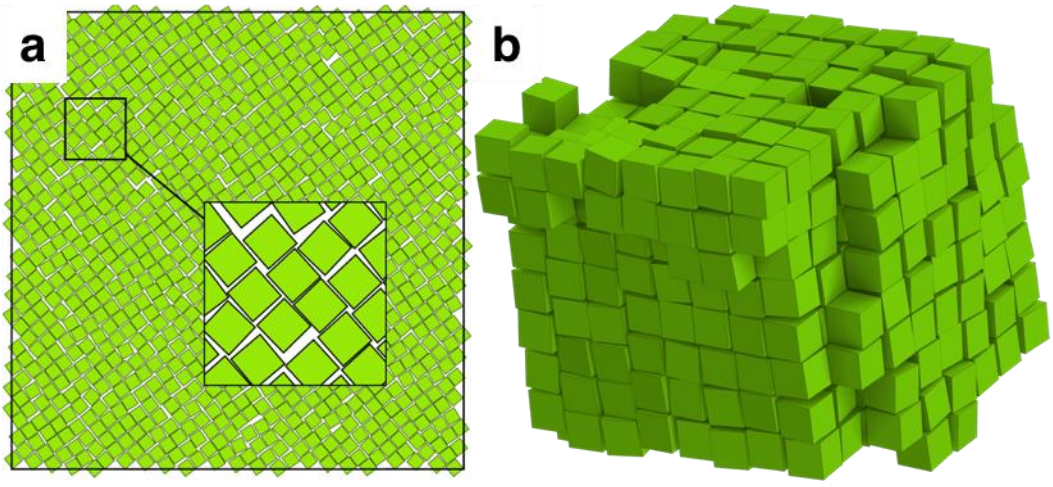


Figure 4-1 **a** two-dimensional hard squares, considered in Chapter 3, are extended to **b** three-dimensional cubes.

Here I investigate the hierarchical assembly of a simple cubic lattice from a family of congruent hard cube derivatives: prisms, general polyhedra, and so-called supercubes (shapes that require > 2 to re-assemble a cube). For each class, I consider two examples of each: rectangular (RP) and right-isosceles triangular prisms (TP), in a direct analog to the previous two-dimensional study; central cut shapes forming a rhombic (RFP) or hexagonal cut face (HFP); and shapes requiring three (S3) or six (S6) members to re-assemble the cube, shown in Figure 4-2. I identify which shapes successfully assemble the desired crystal structure, and analyze the pair motifs that form as a result of the emergent directional entropic forces. This provides us with insight into the features of these shapes that aid or inhibit the hierarchical self-assembly, leading to better design of such shapes.

Hierarchical self-assembly is a well-studied phenomenon with a wide range of application[161–166], including nanoparticle, colloidal, and biological systems. The choice of "force" with which to guide self-assembly is system dependent; therefore, having as many mechanisms to guide hierarchical assembly is very important, allowing scientists and engineers as many design choices as possible. While chemical functionalization is a powerful tool, technical challenges and limiting factors[167] make investigation into other mechanisms, such as shape manipulation, important.

Hard cubes[36,168–171] are known to self-assemble a cubic crystal, with a fluid-crystal coexistence at a reduced pressure $P^* = 6.16$[36]. Previous investigation into systems of hard rectangular prisms identified a rich phase behavior[172], including

a smectic phase at $P^* \approx 20.75$, a columnar phase at $P^* \approx 30.68$, and a cubic crystal at $P^* \approx 50.97$[90]. More complicated hierarchical self-assembly of the "supercube" structure has also been observed[34], suggesting the influence of the crystal lattice structure on the local assembly behavior of hard particles. Due to the similarities and differences between these three-dimensional systems and the previously studied two-dimensional systems, a better understanding of the pair motifs that form in the fluid phase due to emergent, directional entropic forces, and how these motifs either encourage or inhibit the self-assembly of an ordered structure will yield important information regarding the design of nanoparticles and colloids for hierarchical self-assembly.

## 4.2 Methods

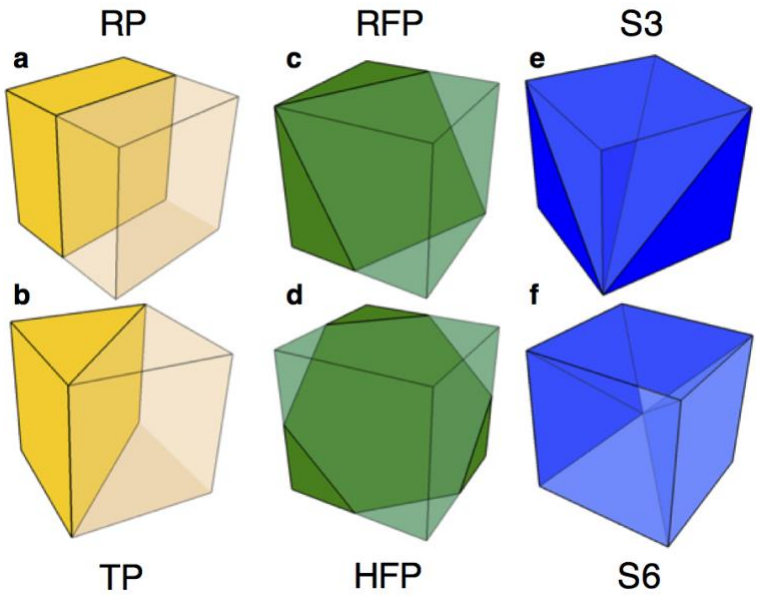


Figure 4-2 Illustration of shapes studied in this paper: **a** rectangular prisms (RP)*[90]; **b** right-isosceles triangular prisms (TP); **c** rhomb-faced polyhedra (RFP); **d** hexagonal-faced polyhedra (HFP); **e** 3-piece supercubes (S3); and **f** 6-piece supercubes (S6)*[34]. The cube formed by the assembled shapes is rendered with one (or more) of the pieces rendered transparent to better show the faces that touch to form the assembled cube. These decompositions are chosen as they yield congruent slices (each resulting slice is the same). Shapes marked with a star have been previously studied.

I consider three classes of polyhedral (prisms, pairs, and “supercubes”), each class with two representatives, shown in Figure 4-2. Analysis of rectangular prisms and the “supercube” S6 shape are included as a control due to their known phase behavior. Systems of $N = 2000$ hard polyhedra are simulated in the *NPT* thermodynamic ensemble using HOOMD-blue[87,93,125,126] with HPMC[93] on CPUs. These systems are initialized on a low-density ($\phi = 0.2$) lattice, are thermalized to a low-density fluid, then compressed at a constant pressure and run for at least $300 \cdot 10^6$ MC sweeps to equilibrate. All measurements are taken in equilibrated systems.

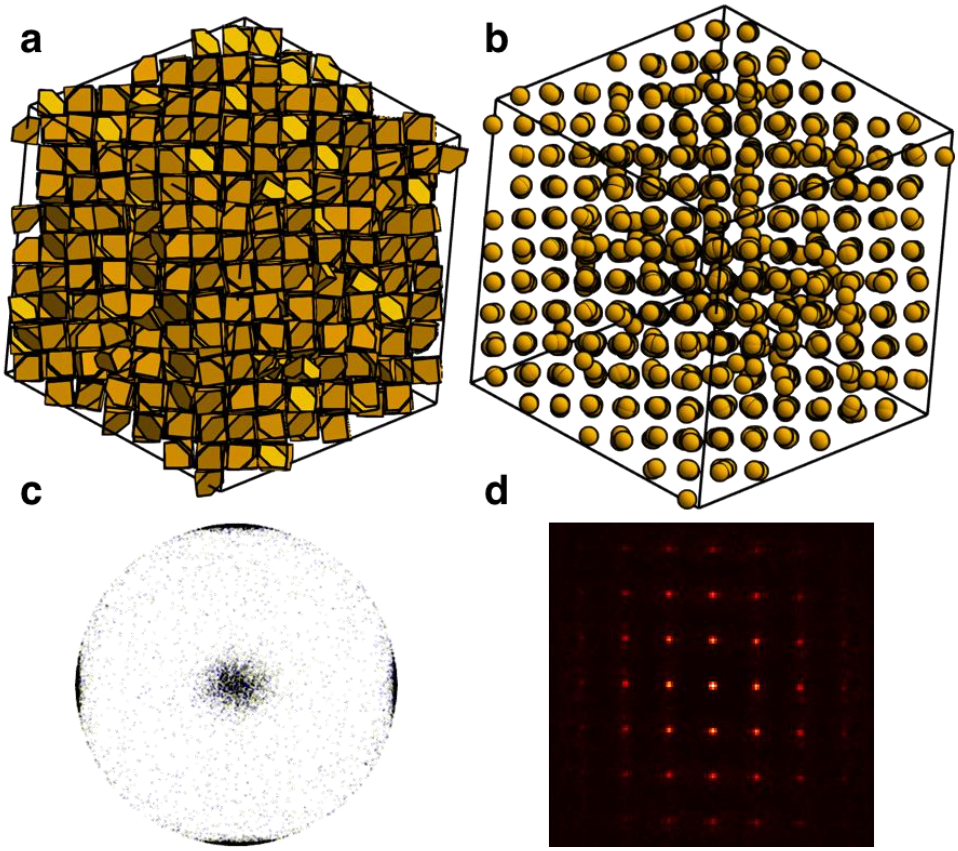


Figure 4-3 **a** image of the self-assembled cubic lattice of the HFP shape. **b** the same system in **a**, rendered as spheres, with the center-of-mass of the HFP shifted to the center of the cube (on the cut face of the HFP). The choice of viewing angle in **a** and **b** show the simple cubic structure. This angle is also used in calculating the **c** bond-order diagram and **d** diffraction pattern. These two metrics also show the cubic lattice, the bond-order diagram showing neighbors positioned in the directions of the faces of a cube, and the diffraction pattern showing cubic periodicity. Please refer to Chapter 2.4.4 for more information regarding the bond-order diagram and diffraction pattern.

I determine the self-assembled structure by visual analysis (Figure 4-3**a**,**b**), along with calculating the bond-order diagram (Figure 4-3**c**) and diffraction pattern (Figure 4-3**d**). Considering both the actual positions and orientations of the polyhedra (Figure 4-3**a**) as well as the centers-of-mass of the parent cube (Figure 4-3**b**) provides visual evidence of the simple cubic structure. This visual analysis also enables calculation of the bond-order diagram (Figure 4-3**c**), accounting for the average positions of neighboring polyhedra, as well as

calculation of the diffraction pattern (Figure 4-3**d**). The Bragg peaks in the diffraction pattern provide evidence of long-range translational order.

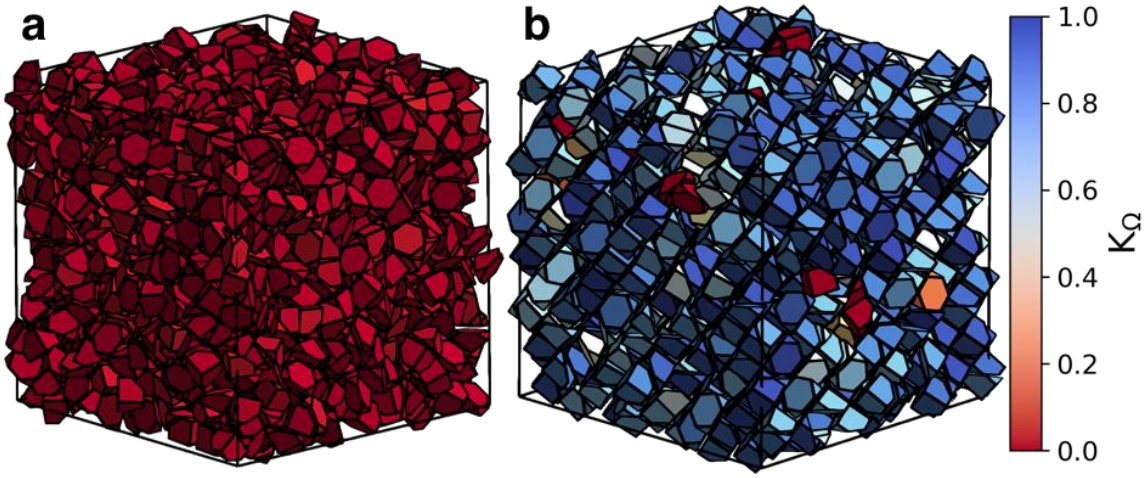


Figure 4-4 Self-assemblies of HFP shapes in **a** the disordered fluid and **b** ordered simple cubic phases.Each individual shape colored by the cubatic order parameter, $K_\Omega$. The cubatic director is computed for the entire system, and the alignment of each shape to the cubatic director provides the measure of the local cubatic order. To facilitate understanding, I let $K_\Omega \to 0$ be red, and $K_\Omega \to 1$ be blue).

I also compute the cubatic order parameter, $K_\Omega$, shown in Figure 4-4, to measure the degree of orientational order in the system (please see Chapter 2.4.4 for a detailed explanation of this calculation). Unlike the bond-order diagram, which accounts for the relative position of a neighbor to a particle, the cubatic order parameter accounts for the orientation of all particles in the system. This order parameter is chosen because the shapes under consideration must be ordered in a cubic fashion in the simple cubic system. Additionally, it is known that orientational rather than translational order develops first in RP systems, requiring the use of an orientation-based order parameter to identify intermediate phases between a fluid and simple cubic crystal. The existence of a cubatic phase in 2:1 rectangular prisms and related systems is also currently under

debate, and calculation of this order parameter will provide evidence of such a phase.

To analyze the pair motifs found in the fluid phase, I must compute the local geometric configuration of particle pairs, as described in Chapter 2.5. I then use the t-distributed stochastic neighbor embedding dimensionality reduction technique (t-SNE)[116,117] to allow for the clustering of these motifs *via* Gaussian Mixture Methods[119–121]. Further analysis of these clusters into categories yields insight into the motifs preferred by the system in the fluid phase, and how these motifs facilitate or inhibit the self-assembly of the desired simple cubic phase. Here I perform the t-SNE analysis on a set of 8000 vectors sampled from 10 independent simulation trajectory frames. To obtain the population average of the motifs, I average across three independent simulations at the same thermodynamic statepoint, *NPT*.

## 4.3 Results and discussion

I start by analyzing the control systems (those previously studied): the 2:1 aspect ratio rectangular prisms (RP), and the square pyramid supercubes (S6). Because RP systems first break symmetry by adopting orientational order rather than translational order[90], I use the cubatic order parameter, $K_\Omega$, instead of the t-SNE analysis, as $K_\Omega$ provides a more robust measure of the relevant order.

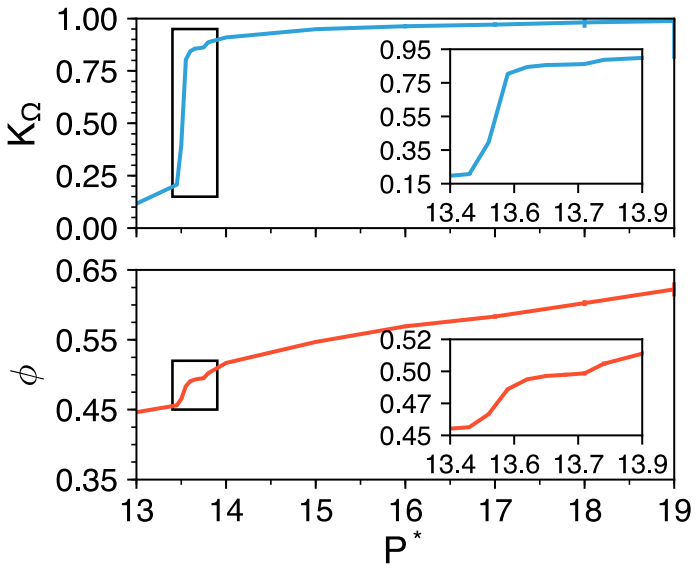


Figure 4-5 Cubatic order parameter, $K_\Omega$, and the equation of state for 2:1 rectangular prisms (RP), showing the existence of the previously unreported cubatic phase, evidenced by the simultaneous increase in $K_\Omega$ accompanied by an increase in system density $\phi$ at $P^* \approx 13.5$. The slight increase in $K_\Omega$ with an increase in $\phi$ at $P^* = 13.8$ shows the transition from the cubatic phase to a smectic phase. The zoomed insight highlights the fluid-cubatic-smectic phase transitions. Please see Figure 4-6 for images of these phases.

I calculate the density and cubatic order parameter, $K_\Omega$, over a range of pressures, $P^*$, yielding the equation of state with associated $K_\Omega$, shown in Figure 4-5. I observe a previously unreported phase transition between the known fluid ($P^* < 13.5$) and smectic($P^* > 13.8$) phases. This phase is a cubatic phase, evidenced by the rapid increase in $K_\Omega$ in this region of the equation of state ($13.5 < P^* < 13.65$).

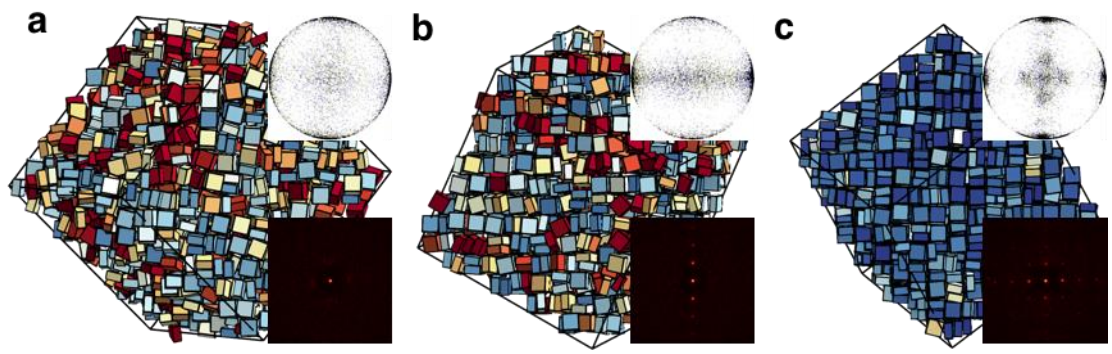


Figure 4-6 Comparison of the **a** cubatic ($P^* = 13.65$), **b** smectic ($P^* = 14.0$), and **c** cubic ($P^* = 21.0$) phases. Each RP is colored by its cubtic order (red: $K_\Omega \to 0$, blue: $K_\Omega \to 1$). The bond-order diagrams (inset upper-right) show order with the six sides of a cube, with an additional equatorial band in **b**, showing the smectic phase. No long-range translational order is present in the cubatic phase (**a**), as evidenced by the lack of peaks in the diffraction pattern; both the smectic and cubic phases show sharp peaks in the diffraction pattern showing existence of long-range translational order.

The difference between the cubatic, smectic, and cubic phases is shown in Figure 4-6. The cubatic phase (Figure 4-6**a**) shows bond order with the six sides of a cube, with no Bragg peaks in the diffraction pattern. The smectic phase (Figure 4-6**b**) shows clear evidence of layers, in both the bond order diagram (darker equatorial band) and in the diffraction pattern with the development of Bragg peaks. The cubic phase (Figure 4-6**c**) shows strong cubic order, and long-range order, evidenced by Bragg peaks in multiple directions.

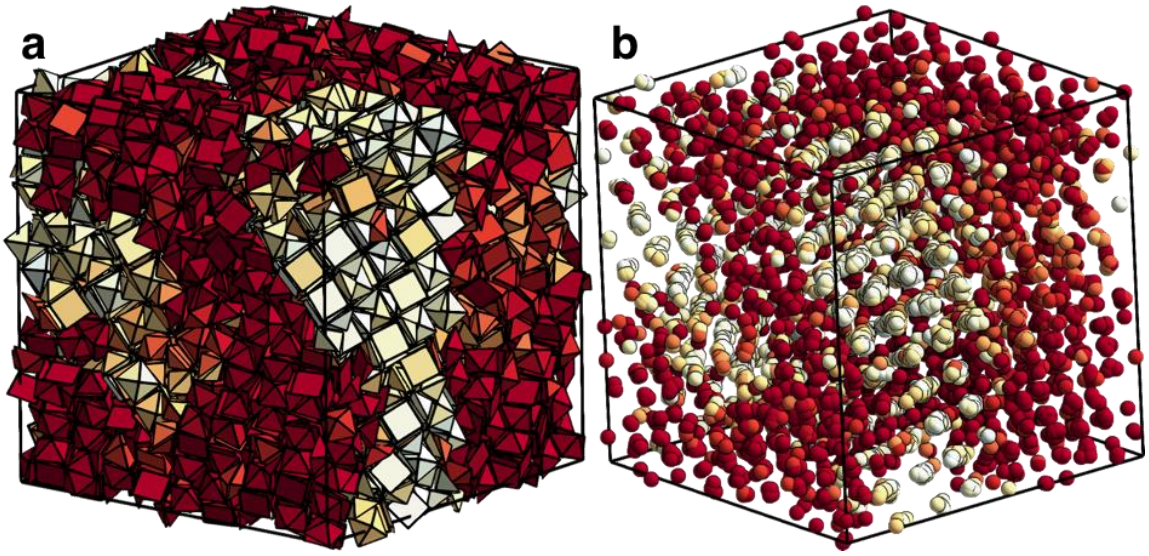


Figure 4-7 View of the self-assembled supercube structure for the S6 shape at a pressure $P^* = 53.0$, showing the nucleation of two different crystallites (red and white). **a** shows the actual polyhedra while **b** shows the center-of-mass shifted to the tip of the square pyramid, showing the simple cubic crystal structure.

I now consider the square pyramid (S6) shape. As in Ref. 34[34], I also observe the self-assembly of the supercube, finding that this shape is prone to forming polycrystalline assemblies, shown in Figure 4-7. To understand what local motifs form during self-assembly leading to this behavior, I employ the t-SNE technique with GMM-based clustering (see Figure 4-8).

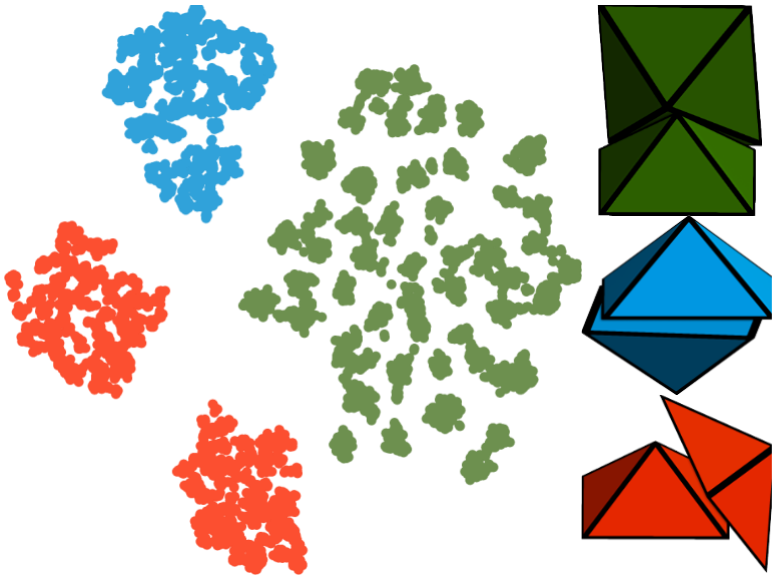

Figure 4-8 t-SNE analysis and classification for the S6 shape. This shape only exhibits three of the four possible geometric pair motifs: cut-face paired (green), square-face paired (blue), and misaligned (red); this shape does not form the "compatible" motif.

The S6 shape forms three different categories of motif in the dense fluid phase: the cut-face pair (blue), the square face pair (red), and the misaligned motif (green). Analyzing the population fraction of these motifs (shown in Figure 4-9), I find that the cut-face motif is most prevalent, forming $\approx 48\%$ of the time. This is perhaps surprising, given that the size of the triangular face is smaller than the square face. Clearly, this indicates the importance of emergence in the directional entropic forces directing the self-assembly of these hard particles. This relatively high population fraction may also explain the formation of multiple crystallites, as the high fraction of pairs should result in the formation of multiple nucleation sites without the guarantee that any local cubic nucleus will be appropriately oriented to other nuclei.

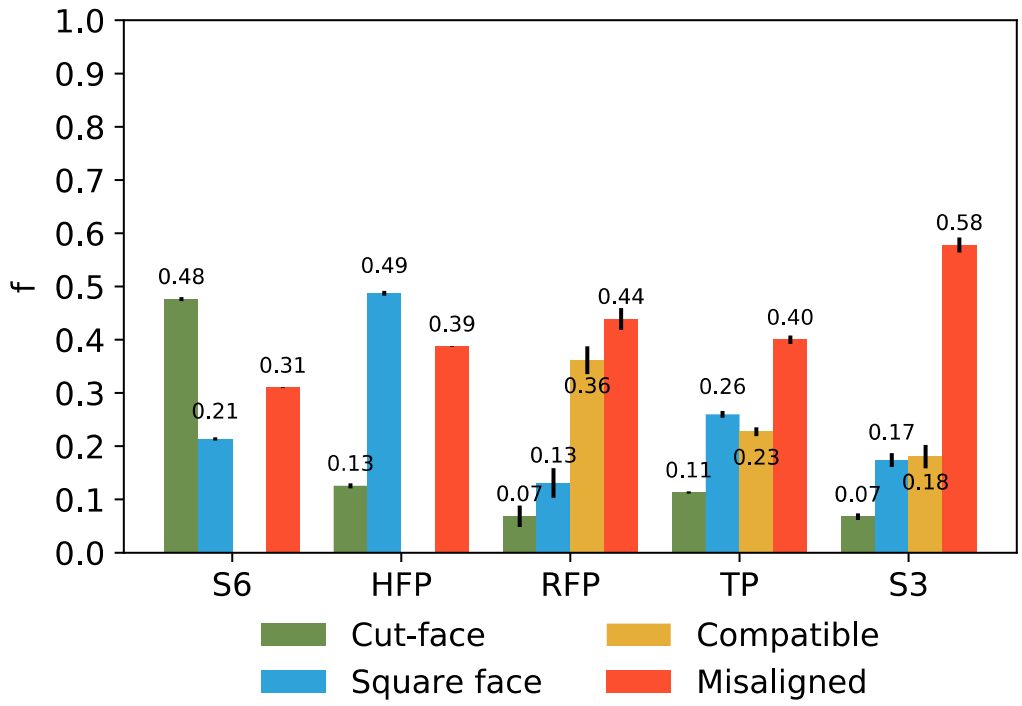


Figure 4-9 Comparison of the fraction of pair motifs found in the dense fluid phase for S6, HFP, RFP, TP, and S3 shapes. Note that S6 and HFP shapes do not form the "compatible" motif, and that the S3 shape is not observed to self-assemble the cubic crystal lattice.

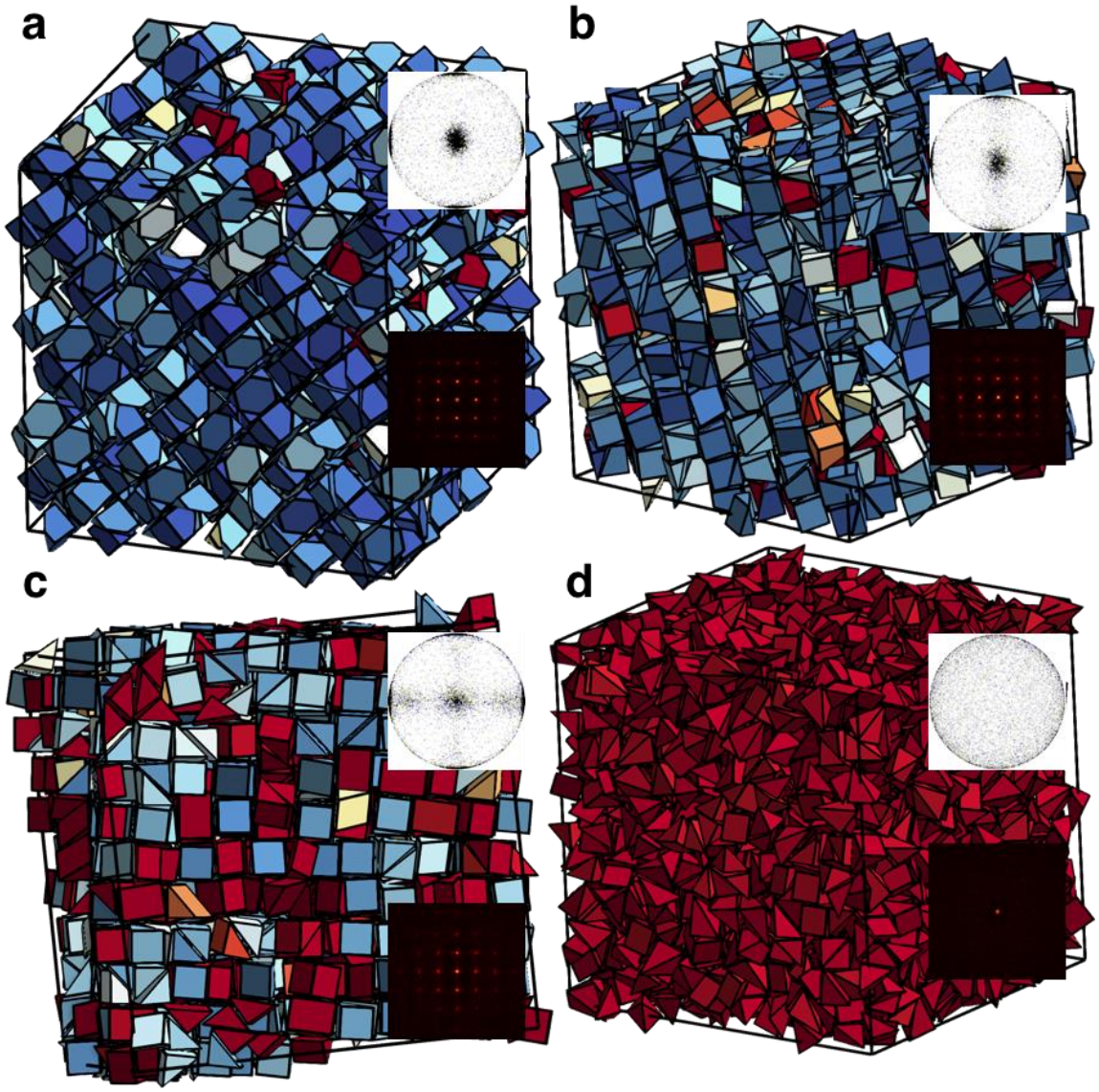


Figure 4-10 Equilibrium self-assemblies colored by the cubatic order parameter (red: $K_\Omega \to 0$, blue: $K_\Omega \to 1$). Inset bond-order diagrams (top) and diffraction patterns (bottom) of **a** HFP ($P^* = 21.0$), **b** RFP ($P^* = 24.0$), **c** TP ($P^* = 18.0$), and **d** S3 ($P^* = 36.0$). Note that only the S3 shape fails to self-assemble into an ordered simple cubic crystal.

I perform the same t-SNE and GMM analysis on the remaining cube derivatives: HFP, RFP, TP, and S3. First, I note that of these shapes, only the S3 shape fails to self-assemble the simple cubic lattice (see Figure 4-10**d** for assembly, and Figure 4-11 for the t-SNE plot). As shown in Figure 4-9, over half of the S3 motifs

are misaligned. This makes the formation of nuclei, and the final simple cubic crystal, prohibitively difficult.

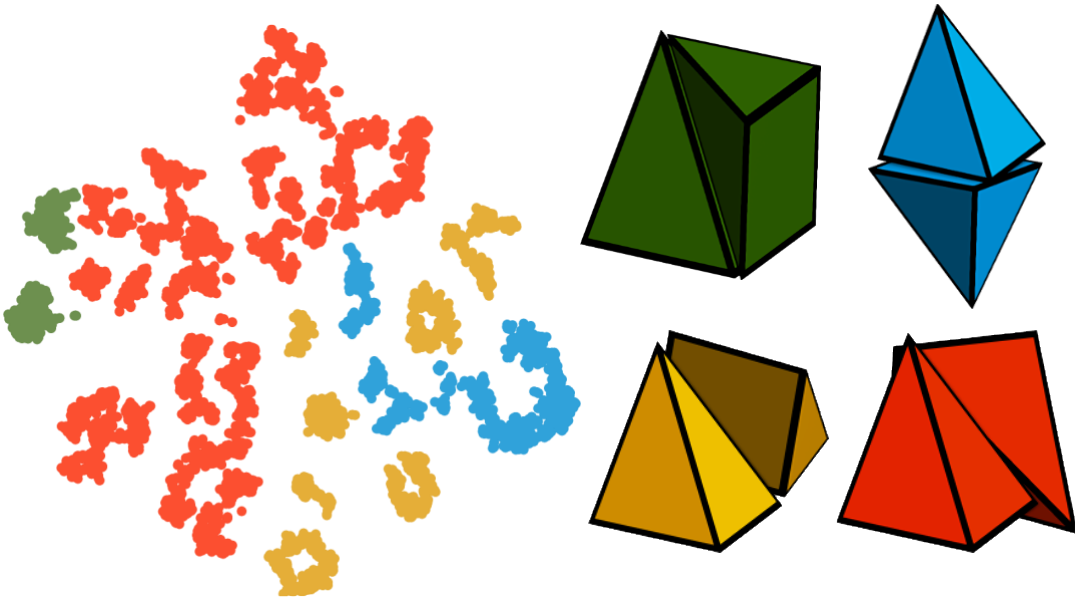

Figure 4-11 t-SNE analysis of the fluid phase for the S3 supercube shape. Color-coded representative motifs are included to the right for convenience: cut-face (green), square-face (blue), compatible (yellow), and misaligned (red).

Both the general polyhedral shapes, HFP and RFP, successfully self-assembly the simple cubic lattice (Figure 4-10**a**, **b**). Similar to the S6 shape, the HFP shape does not exhibit “compatible” motifs, only exhibiting motifs that directly contribute to or compete with the correct self-assembled structure (Figure 4-12**a**). This is a result of the symmetry of the HFP shape. Not only does the cut face have three equivalent alignments, but also the faces that result from square faces are congruent. These congruent faces thus do not exhibit a preference for alignment. In contrast, the RFP shape does exhibit “compatible” motifs. These motifs result from the mismatch between faces. While the cut-face itself has two-fold symmetry, there is only one way to align the cut faces to assemble a cube. Additionally, all three faces resulting from square faces are not congruent.

Looking at the example motifs in Figure 4-12**b**, the bottom face is a square, while the other large faces are not. Additionally, these faces are chiral, requiring one left-handed and one right-handed face to “correctly” pair. These differences result in the lower population fractions of cut-face paired and square face paired for RFP relative to HFP (Figure 4-9). However, as both shapes successfully self-assemble the simple cubic lattice, the differences between the RFP and HFP shapes are not enough to prevent the self-assembly of the desired structure.

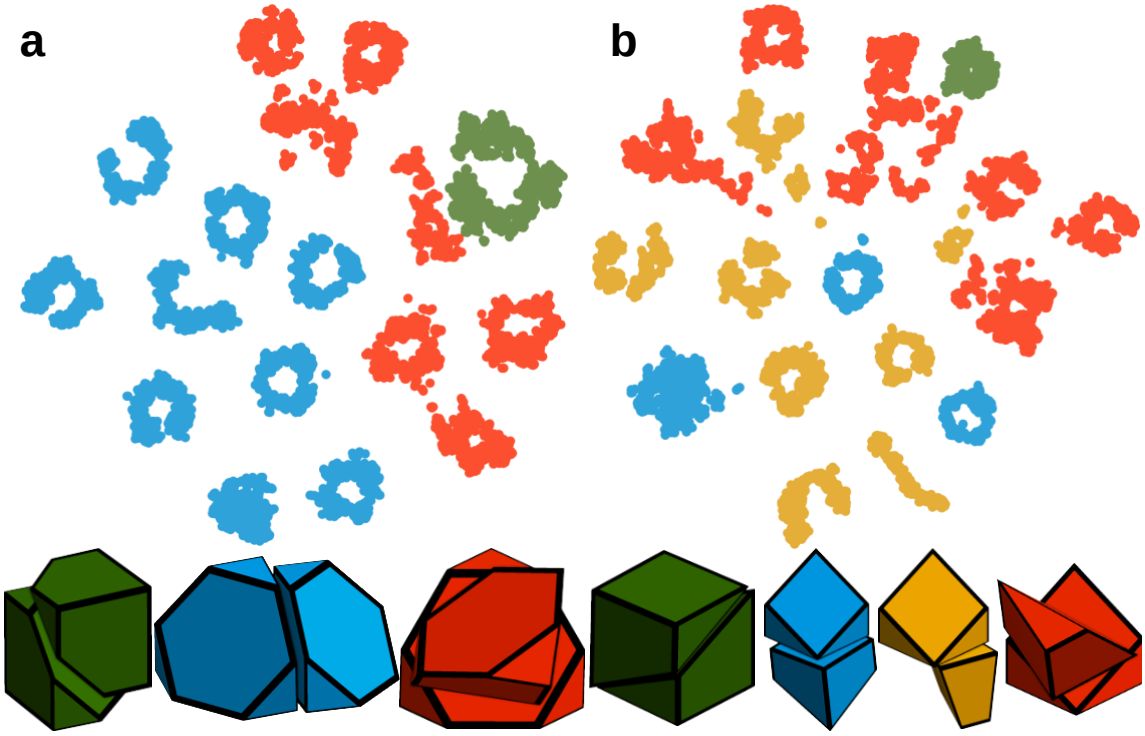


Figure 4-12 Comparison of the t-SNE analysis of the fluid phase pair motifs for **a** HFP and **b** RFP. Color-coded representative motifs are included below: cut-face (green), square-face (blue), compatible (yellow), and misaligned (red). Note that the HFP does not exhibit a “compatible” motif because its three faces originating from the square faces of the cube are congruent. This is in contrast to the RFP: the square face is not congruent with the other faces originating from square faces (**b**, yellow motif). Also note that the two large square faces originating from the square faces are not congruent; being chiral, one left-handed face must pair with a right-handed face to form a square-face pair (red motif), while two left-handed or two right-handed faces will form a compatible pair (yellow motif).

The right-isosceles triangular prism (TP) also successfully self-assembles the cubic lattice (shown in Figure 4-10**c**). As seen in the self-assembled system, bond-order diagram, and diffraction pattern, the self-assembly is not as robust as

the assemblies for either RFP and HFP shape. However, the self-assembly is far more successful than its two-dimensional counterpart[138]. Analysis of the fluid-phase motifs (Figure 4-13) provides a deeper understanding why. Like the RFP, the TP forms all four categories of motif: cut-face paired, square face paired, compatible, and misaligned. The two-dimensional right-isosceles triangles[138] may only form cut-edge pairs and base-edge pairs, analogs of the cut-face paired and square face paired motifs. The additional dimension for the TP adds the additional "compatible" motif, driving the system to an ordered rather than disordered solid phase, shown by the fraction of misaligned motifs in the fluid phase, $f < 0.5$ (Figure 4-9).

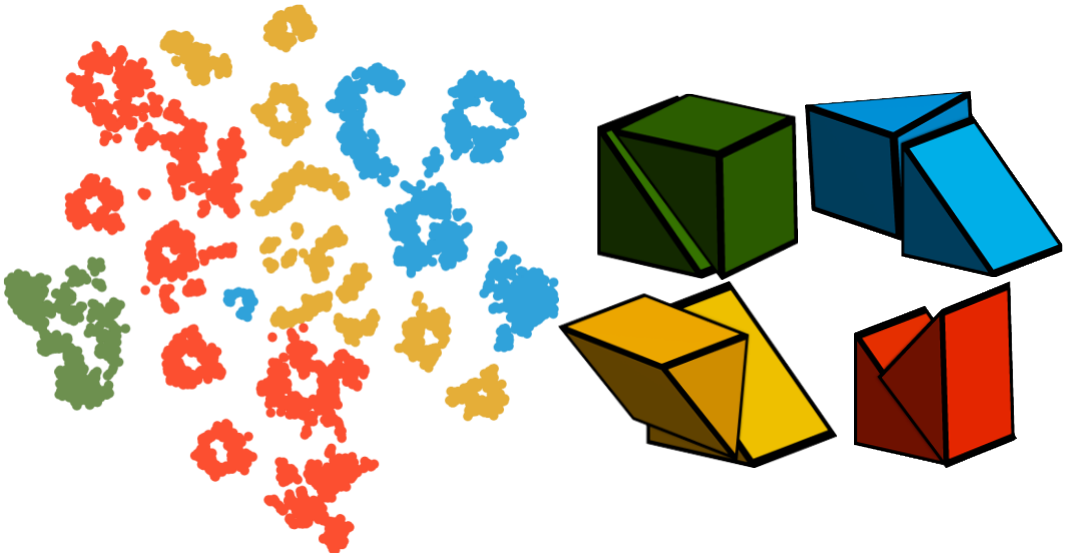

Figure 4-13 t-SNE analysis of the fluid phase for right-isosceles triangular prisms (TP). Color-coded representative motifs are included to the right: cut-face (green), square-face (blue), compatible (yellow), and misaligned (red).

The quantification of these motifs is based on previous investigation into assembly pathway engineering[166]. Ref. 166 suggested that when local motifs form and compete with the target structure, the assembly of the target structure will be hindered or even prevented. These observations reflect and reinforce this

conclusion, as the S3 shape did not self-assemble the target crystal, and the S3 shape is the only shape investigated that has a fluid phase dominated by the misaligned motifs (see Figure 4-9, Figure 4-11). I summarize these observations of the self-assembly behavior in the following design rules:

1. Shapes should maximize the number of correct ways to assemble intermediate motifs, minimizing the number of ways into incorrectly assemble intermediate motifs
2. Shapes should possess “selectivity”; particle faces should be different enough to prevent local motif “confusion”

Both the HFP and S6 shapes demonstrate the synergy of these design rules: both shapes avoid compatible motifs, so that there is no confusion about motifs that lead to the final crystal. While compatible motifs are present in both RFP and TP shapes, these motifs do not compete with the final crystal structure. This is not the case for the S3 shape. This shape exemplifies the antithesis of these design rules. The faces resulting from the original square faces are congruent; however, they are very similar in size to the cut-faces, resulting in motif confusion, introducing competition between correct and incorrect motifs. Additionally, the cut-faces are similar but not congruent, introducing further competition between correct and incorrect motifs, further decreasing the drive toward self-assembly of the correct crystal structure.

## 4.4 Conclusion

I investigated the hierarchical self-assembly behavior of a family of hard cube derivatives, determining the success and failure of their ability to assemble a

simple cubic lattice. I report evidence for the existence of a cubatic phase for 2:1 aspect ratio rectangular prisms, as well as verifying the self-assembly of square pyramids into the “supercubic” crystal structure. In our investigation of these six shapes, I quantify the pair motifs that form in the dense fluid phase, relating these geometries to their ability to self-assemble the desired crystal structure. By grouping these motifs into categories contributing to or competing with successful self-assembly, I gain a deeper understanding into effect that particle shape has on the final crystal structure.

Further investigation into entropy-driven hierarchical self-assembly of anisotropic particles should be considered. Here I only attempt the self-assembly into a simple structure. Further investigation of hierarchical self-assembly of other simple (BCC, FCC) and more complex ($\beta$-Mn, quasicrystals) structures will provide a better understanding of the limitations of entropy-driven hierarchical self-assembly. Allophilic shaping, currently only considered in two-dimensional systems[138], should be investigated for polyhedral systems, allowing for similar manipulation of the crystal structure obtained *via* self-assembly. The analysis considered here should be extended with calculation of the potential of mean force and torque[60,173]. This will provide additional insight into the effective driving force to form the preferred pair motifs, as well as the topology of the effective free-energy landscape. This insight will enable the design of shapes more effective at hierarchical self-assembly, providing scientists and engineers more tools to create novel materials with previously unavailable properties.

# Chapter 5

# Nature of the Entropic Bond in Particle Assemblies

*Note: this chapter is adapted from* Nature of the Entropic Bond in Particle Assemblies[173], *submitted to* Nature *in* 2018.

Having observed the existence of an emergent directional entropic force arising due to the shape of and crowding of nanoparticles and colloids[34,72] in Chapter 3 and Chapter 4, and that this force may be quantified through the Potential of Mean Force and Torque[60,82] (see Chapter 2.3), the similarities between these forces and traditional forces that govern chemical bonding cannot be ignored[174–177]. It is natural to wonder if there exists an analogous *entropic bond* that forms due to the directional entropic force to the chemical bonds form due to electromagnetic and quantum-mechanical forces. To demonstrate the existence of the entropic bond, I relate the observed phenomena to the analogous hydrogen bond in classical chemistry. I quantify the effects of both system density and particle shape on entropic bonds. I demonstrate the ability for these bonds to be quantified in a similar manner to chemical functionalization on nanoparticles and manipulated in similar ways.

## 5.1 Introduction

The *International Union of Pure and Applied Chemistry* defines the chemical bond as[178]:

*When forces acting between two atoms or groups of atoms lead to the formation of a stable independent molecular entity, a chemical bond is considered to exist between these atoms or groups. The principal characteristic of a bond in a molecule is the existence of a region between the nuclei of constant potential contours that allows the potential energy to improve substantially by atomic contraction at the expense of only a small increase in kinetic energy. Not only directed covalent bonds characteristic of organic compounds, but also bonds such as those existing between sodium cations and chloride anions in a crystal of sodium chloride or the bonds binding aluminium to six molecules of water in its environment, and even weak bonds that link two molecules of O2 into O4, are to be attributed to chemical bonds*.

This definition covers *all* chemical bonds, from ionic and covalent bonds to hydrogen bonds. Hydrogen bonds are particularly interesting given their more temporal nature and lower strength than other types of chemical bonds[176–178]. Interestingly, this definition does not require the use of electrons, electromagnetic fields, or quantum mechanics, leading to the question about the minimal model required for a chemical bond.

As noted in Chapter 1, scientists and engineers have been investigating the self-assembly of nanoparticle and colloidal systems, using a variety of mechanisms to attract and “bind” particles together. Some methods leverage chemical bonds to link particles *via* chemical functionalization such as with thiol[179] or DNA coatings[180,181], using complementary strands to bind when in close proximity. These particles have effective *enthalpic* patches[83], enthalpic due to the release in energy from the formation chemical bonds between particles. Other methods utilize particle geometry itself to create colloidal valence, such as with lock-and-key colloids[28,37,182,183], and with other shape-complementary particles[147,184]. Hydrogen bonds are responsible for some of the most important structures and phenomena in nature. From the DNA double-helix to the expansion of ice upon

freezing, the unique properties of water that derive from hydrogen bonding are in many ways responsible for life as we know it. Unlike the stronger chemical bonds (metallic, ionic, and covalent), hydrogen bonds are unique in that they can rearrange and reconfigure at biologically relevant temperature, while still directing the formation of complex structures[185–188]. This temporal nature leads to a measureable *bond lifetime*[185,189–191].

## 5.2 Methods

I investigated systems of perfectly hard polygons to determine the nature of the entropic bond. Because shape is the independent variable of interest, these particles must be both perfectly hard and perfectly sharp to avoid any confounding effects due to interparticle potentials and rounding. The phase behavior of hard, hexagonal platelets is well-known[108], and provides an excellent place to start our investigation. Hexagons are beneficial to study as they have significant mobility in their solid phase, allowing for measurement of bond lifetimes in both fluid and solid phases. Given the existing knowledge of the equation of state and phase behavior of hard hexagons, I simulated in the *NVT* thermodynamic ensemble.

Hard hexagons are also geometrically related to systems of hard, elongated rhombs (see Figure 5-6), an experimental system whose behavior is also well-established[179]. This shape is of particular interest as it can assemble two different ordered crystals, yet entropically self-assembles only one, despite a vanishingly small difference in free-energy. By altering the shape of these elongated rhombs,

the effect of shape on emergent entropic bonds can be established and compared to experimental results.

Because the equation of state for these systems is not established, I use the *NPT* thermodynamic ensemble to avoid any phase coexistence. I will explain why entropic self-assemble only yields one ordered phase, as well as compute the required interaction bias to self-assemble the other crystal phase using entropic bonds, further establishing entropic bonds.

The choice of state point at which to compare PMFTs is just as critical. At what thermodynamic value e.g. $P^*$ should the PMFTs be compared? In this study, the PMFTs for hard hexagons are analyzed at different densities $\phi$, to determine the impact that crowding has on the emergent directional entropic force. For elongated rhombs, it is the forces present in a system at the point of self-assembly that need to be compared; therefore, it is most appropriate to compare these systems at the highest $P^*$ in the fluid phase possible.

To compare hard polygonal systems and their emergent entropic bonds to systems of hydrogen bonds, I must be able to discern when a pair of particles is bound. Molecular systems exhibiting hydrogen bonding use energetic or geometric limits to determine when a bond is formed or broken: two or more atoms, molecules, etc. are in a bond if these particles have a potential energy less than some value, or are in the bounds of a particular geometric arrangement (which correspond to some energetic limits). Similar limits must be calculated for our systems of entropically-bound particles.

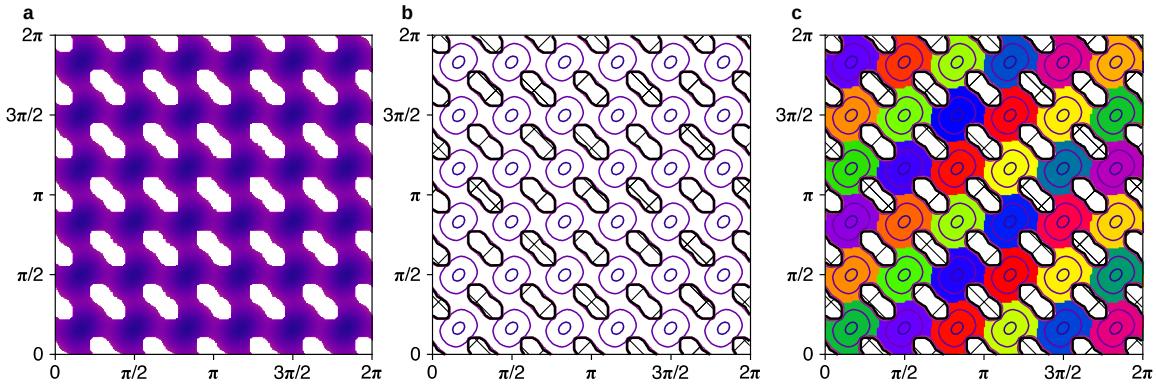


Figure 5-1 Summary of the entropic bond analysis pipeline: **a** The raw PMFT is passed through a Gaussian blur **b** (rendered here as contours) to remove any noise or artifacts before passing into the image segmentation algorithm. **c** The full range of the PMFT is shown: $\theta_1, \theta_1 \in [0, 2\pi]$, showing the 36 identical entropic bonds in systems of regular hexagons. Due to the periodic nature of these PMFTs, all other PMFTs shown in this these display a single periodic region e.g. $\theta_1, \theta_1 \in \left[0, \frac{\pi}{3}\right]$ for regular hexagons. This figure is also shown in Chapter 2.3.1.

I use the PMFT to compute the entropy-density landscape (shown in Figure 5-1), analogous to calculations of electron density in DFT calculations. Analysis of this landscape allows for the minima, transition states, and maxima to be determined, putting geometric limits derived from energetic limits on the emergent entropic bonds, just like in systems with hydrogen bonding. Please see Chapter 2.3.1 for more information regarding the PMFT and the calculation of the Entropic Bond.

## 5.3 Results

Sampling of systems at equilibrium yield the emergent, directional entropic force as measured by the PMFT. As discussed in Chapter 2.3.1, the two-dimensional PMFT integrates over the paired-particle orientation, failing to distinguish between local motifs that intuition suggest should be attractive and repulsive, as shown in Figure 5-2.

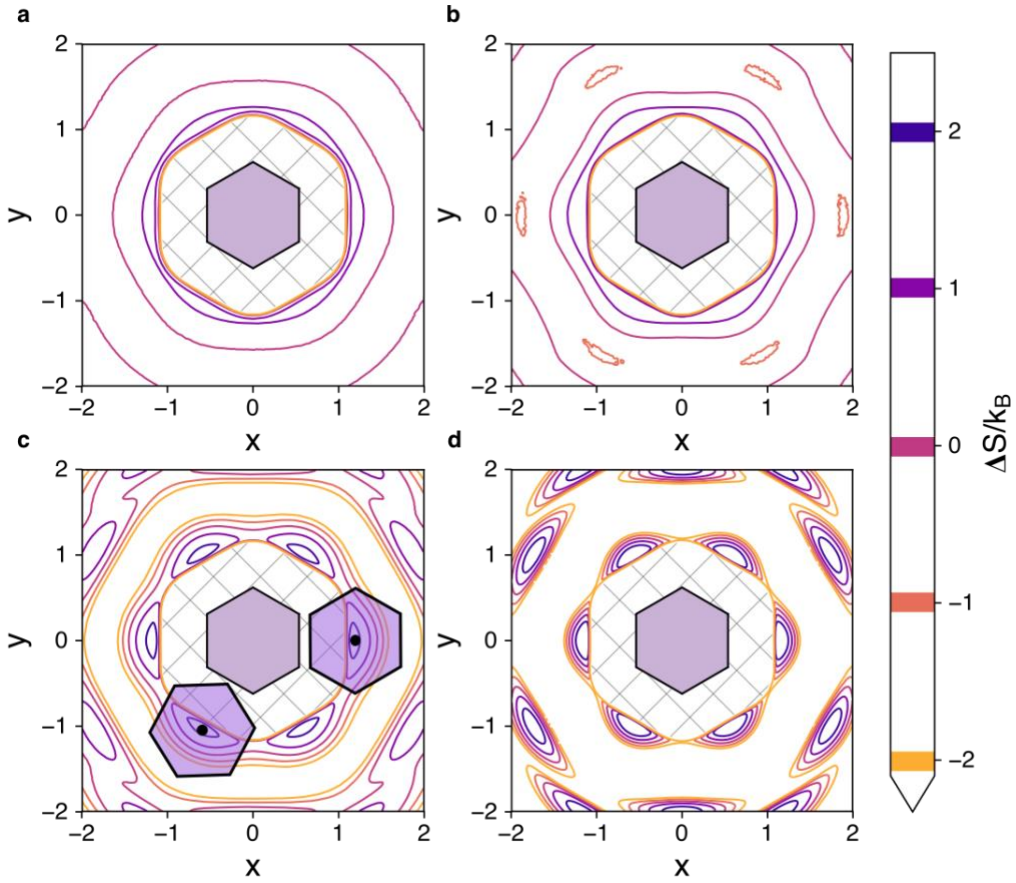


Figure 5-2 Two-dimensional PMFTs in the $(x, y)$ coordinate system for systems of hard hexagons at **a** $\phi = 0.55$, **b** $\phi = 0.65$, **c** $\phi = 0.75$, and **d** $\phi = 0.85$. At low density (**a**), there is very little attraction or repulsion between hexagons. As density increases, regions of effective attraction and repulsion begin to develop. For example, in **b** the dark purple ``ring'' around the geometrically forbidden ring aligns with the edges of the hexagon, showing that these edges are effectively attractive, while the rings that develop further out correspond to low-entropy configurations that are not favorable and are effectively repulsive. Once in the solid phase, these regions of attraction and repulsion (high-entropy regions and low-entropy regions) are more distinct. At a density of $\phi = 0.75$ (**c**), configurations of paired particles in face-to-face and vertex-to-face configurations demonstrate how this two-dimensional coordinate system integrates over paired-particle orientations, as both configurations fall into a single high-entropy region. In the solid phases, the inter-neighbor regions are of very low-entropy, so that transitions between 1$^{st}$ nearest-neighbors and 2$^{nd}$ nearest-neighbors become less likely.

Computing the three-dimensional PMFT yields a free-energy landscape that properly distinguishes between these motifs, allowing for the identification of ground states (free-energy minima) and transition states (local maxima) between different entropic bonds.

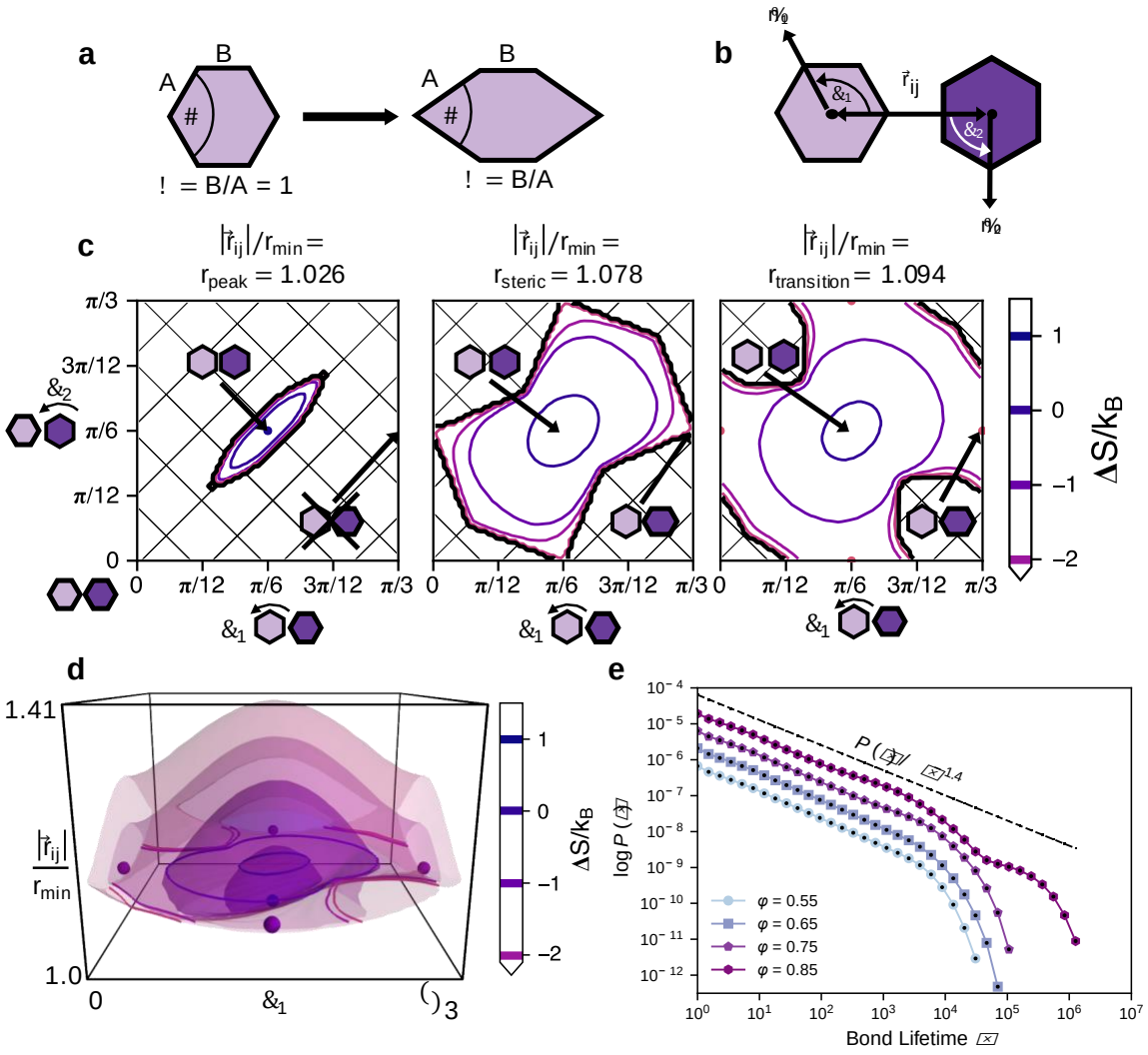


Figure 5-3: **a** Transformation of a regular hexagon $(\alpha = 120°, \gamma = 1)$ into an elongated rhomb $(\alpha = 68°, \gamma)$ $\gamma$ is the ratio of sides $B$ and $A$, a tunable shape parameter to study the influence of shape on entropic bonds; $\gamma = 2/3$ for this schematic and in Figure 5-6. **b** Coordinate system describing directional entropic forces in two-dimensional systems: $(r, \theta_1, \theta_2)$. $\theta_1$ is the angle between the orientation of particle $i$ and the interparticle vector $\vec{r}_{ij}$ (and *vice versa* for $\theta_2$). This coordinate system distinguishes between pair orientations integrated over in the $(x, y)$ coordinate system (see Figure 5-2**c** for an example). **c** Contour plots of excess entropy density $\Delta S(r, \theta_1, \theta_2)$ at three distances $r$ for hard hexagons at packing fraction $\phi = 0.75$: $r_{\text{peak}} = 1.026$ contains the highest excess entropy $(\max(\Delta S))$ in the landscape, corresponding to the edge-aligned pair configuration, shown as a dot at the preferred motif $\left(r = 1.026, \theta_1 = \frac{\pi}{6}, \theta_2 = \frac{\pi}{6}\right)$; $r_{\text{steric}} = 1.078$ is the closest distance that particle pairs may freely rotate, breaking an entropic bond. The negative excess entropy of this configuration indicates that such configurations are unfavorable; $r_{\text{transition}} = 1.094$ contains the transition states between entropic bonds, indicated with dots at the vertex-to-edge configuration $\left(r = 1.094, \theta_1 = \left[0, \frac{\pi}{3}\right], \theta_2 = \left[0, \frac{\pi}{3}\right]\right)$. See Figure 5-4 for plots at $\phi = 0.55, 0, .65, 0.85$ (see Figure 5-5 for a schematic of an entropic bonding transition). Hashmarks indicate pair configurations forbidden due to geometric overlap. Colorbar indicates constant $\Delta S$ contours corresponding to isosurfaces in panel **d**. Due to the symmetry of regular hexagons (panel **b**), the entropy density landscape is periodic, repeating every $\frac{\pi}{3}$; thus, the range of the landscapes is restricted to $\theta_1, \theta_2 \in \left[0, \frac{\pi}{3}\right]$. **D** Excess entropy density isosurfaces in $(r, \theta_1, \theta_2)$. Markers (filled sphere) indicate $\max(\Delta S)$at $r = 1.026$ and transition states at $r = 1.094$. **e** Bond lifetime distribution for hard regular hexagons at four densities $\phi = 0.55, 0, .65, 0.75, 0.85$, corresponding to low-density fluid, high-

density fluid, low-density solid, and high-density solid phases, respectively. Each data series is shifted by a decade for visual clarity. For each data set, statistical error calculated from four independent samples is smaller than plot markers. The line added above the data shows the power-law decay behavior of entropic bonds at short times.

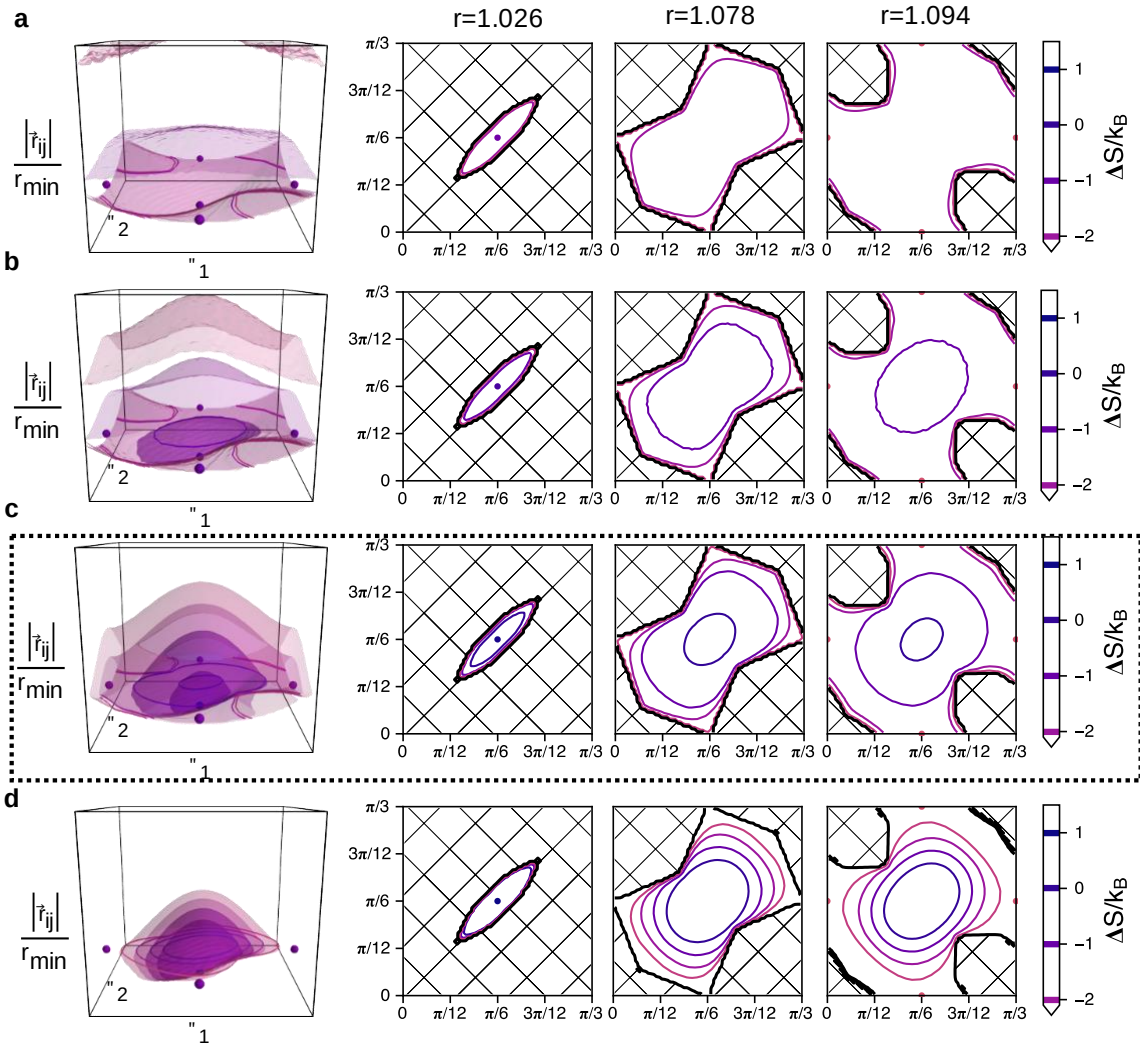


Figure 5-4 Three-dimensional PMFTs in the $(r, \theta_1, \theta_2)$ coordinate system for systems of hard hexagons at **a** $\phi = 0.55$, **b** $\phi = 0.65$, **c** $\phi = 0.75$ (shown in Figure 5-3, outlined here in a dashed line), and **d** $\phi = 0.85$. The far-left column shows a 3D rendering of isosurfaces of constant-entropy density, while the right three columns show slices through the three-dimensional space perpendicular to the r-dimension. The isosurface renderings contain markers for the maximum entropy (centered) and entropy associated with entropic bond transitions (centered on the faces). The cross-sections in the far-right column $r = 1.094$ are rendered within the three-dimensional rendering (far-left column) for visual aid.

Image segmentation (Figure 5-1) of the entropy density landscape for hard hexagons show well-defined regions in $(r, \theta_1, \theta_2)$ coordinates corresponding to distinct entropic bonds (see Chapter 2.3.1 for more information). Each identical region has the edge-to-edge configuration as its ground state. This is the motif

that minimizes the free volume of pair (shown in Figure 5-3**c**), as would intuitively be expected. Comparison across densities (Figure 5-4) shows the increase in entropy (decrease in free-energy) for this motif as density increases, as ought to be expected.

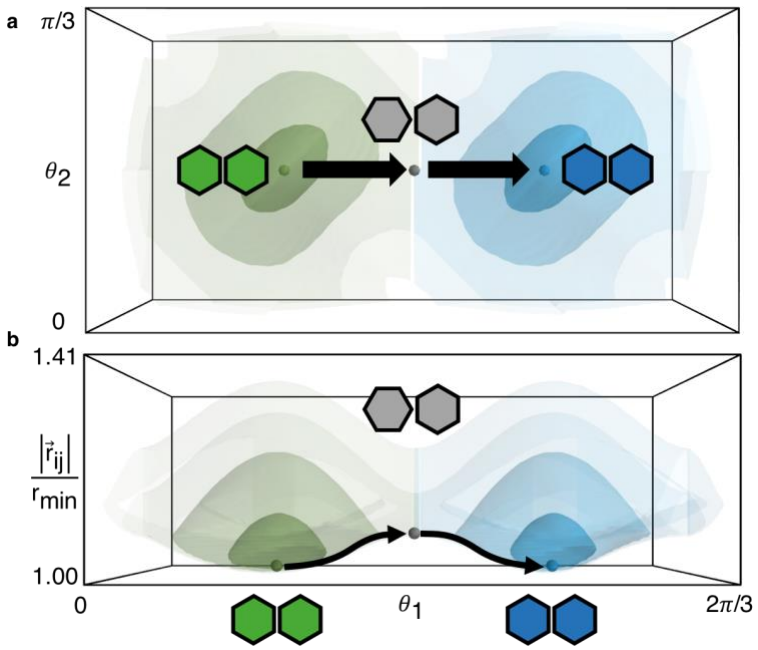


Figure 5-5 Schematic of entropic bond transition between two entropy-density maximum/free-energy minimum states of the lower-density solid hard hexagon system $\phi = 0.75$. Watershed image segmentation (see Figure 5-1, Chapter 2.3.1, Figure 2-4)determines which voxels belong to each bond (here shown in green and blue), while the transition state (shown in grey) is identified by determining the highest entropy-density/lowest free-energy state on the interface of the two bonds. Both a top-view **a** and a side-view **b** of the free-energy landscape is included, and a proposed reaction coordinate is provided, showing one possible pathway particles may take to reconfigure from one bond configuration to another.

Chemical bonds, especially hydrogen bonds, have characteristic bond-lifetime distributions that are still the subject of new research[189]. If entropic bonds are chemical bonds, they should possess similar distributions. Tracking of particle pairs throughout consecutive MC trajectory frames yields the bond lifetime distribution, shown in Figure 5-3**e**.

The bond lifetime distribution for systems of hard hexagons exhibit both power-law and exponential behavior. First, I observe a general increase in probability for

longer bond lifetimes as density increases. As discussed in hydrogen bonding literature, the power-law behavior corresponds to diffusive behavior of the hard particles, which should be density-independent for small timescales. The exponential decay observed for long timescales is explained by the need for particle pairs to climb out of a free-energy well. The functional form of these distributions agrees with the functional form of the bond lifetime distributions for hydrogen bonding in systems of liquid water. Given the overall similarity to existing systems of hydrogen bonds, I conclude that the observed behavior is in agreement with that of bonding.

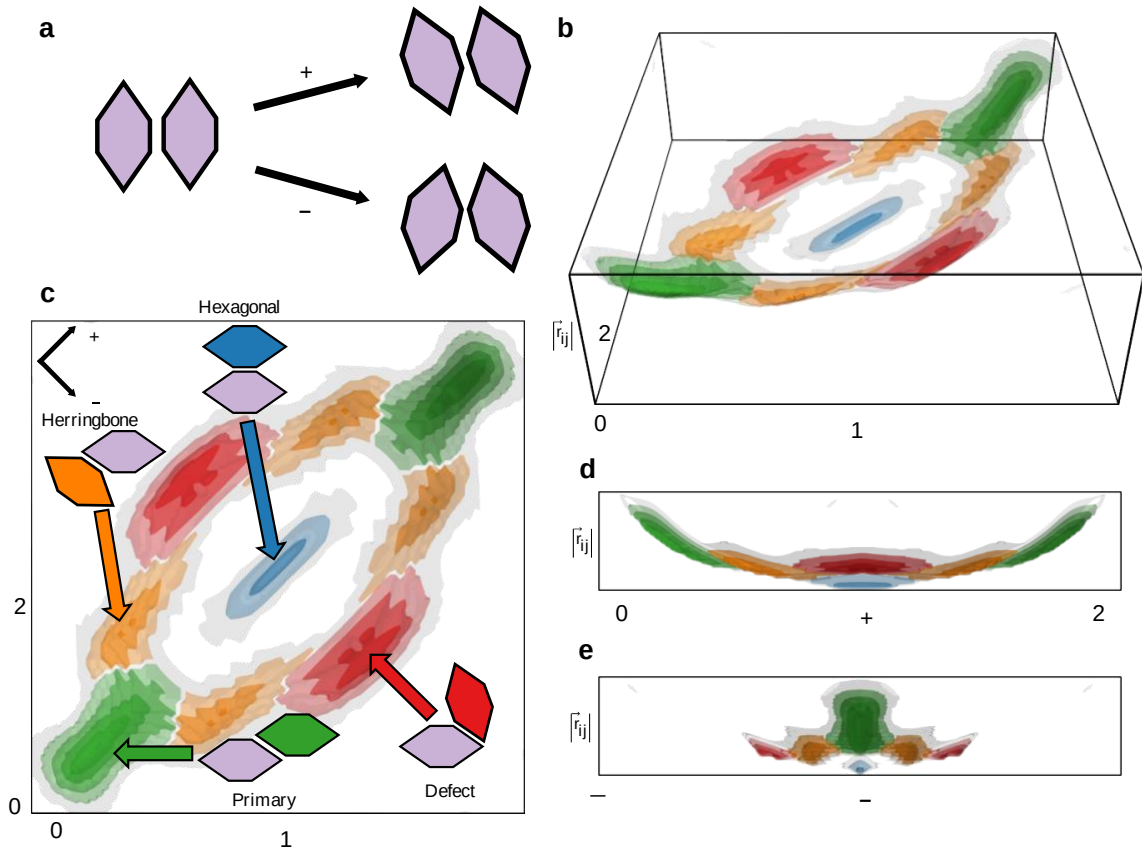


Figure 5-6 **a** Schematic illustrating alternate coordinates for particle orientation associated with particle libration: $\theta_+$ and $\theta_-$. $\theta_+$ accounts for shearing motion, and $\theta_-$ accounts for twisting motion. **b** Isometric view of entropy density landscape, with the different regions corresponding to different entropic bonds colored by bond type. **c** Top view of the entropy-density landscape shown in **b**, with entropic bond motifs labeled as follows: *primary* bonds (green), present in both hexagonal and herringbone lattices; *hexagonal* bonds (blue), present only in the hexagonal lattice; *herringbone* bonds (orange), present only in the herringbone lattice; and *defect* bonds (red), which are antagonistic to either crystal lattice. Note that due to the symmetry of elongated rhombs, the entropy density landscape is periodic, repeating every $\pi$; thus, the range of the landscapes is restricted to $\theta_1, \theta_2 \in [0, \pi]$. Excess entropy density isosurfaces indicate regions corresponding to each bond type (isosurfaces corresponding to $\frac{\Delta S}{k_B} = [2.5, 2, 1.5, 1, 0.5]$ shown in lighter coloring). $\frac{\Delta S}{k_B} = 0$ is indicated with a grey isosurface for reference. **D** Orthographic view of $(r, \theta_+, \theta_-)$ showing the curvature of the entropy density landscape in $r$. The greater elongation along the $(0,0) \rightarrow (\pi,\pi)$ compared to $(0,\pi) \rightarrow (\pi,0)$. **e** indicates greater ability for shear libration, as opposed to twist libration. See Figure 5-7 for PMFTs for $\gamma = \frac{1}{2}, \frac{2}{3}, 1, \frac{2}{3}, 2$.

Having established the effect system density has on entropic bonds, we now must understand the impact of particle shape on entropic bonding. I start by deforming our base shape into an *elongated rhomb*, a shape previously investigated in simulation and experiment[83]. To alter a regular hexagon into an elongated rhomb, opening angle $\alpha$ is closed from $\alpha = 120°$ to $\alpha = 68°$, matching

experimental $LnF_3$ platelets. The shape parameter $\gamma = \frac{B}{A}$ is introduced to manipulate the shape of the elongated rhomb and measure its effect on the measured PMFT.

Immediately, the effect on the PMFT is pronounced. Gone is the 6-fold symmetry of the hexagon, reduced to 2-fold symmetry. While there are still a total of 36 bonds in the region $\theta_1 : [0,2\pi]$; $\theta_2 : [0,2\pi]$, they are no longer identical. There are now four different types of bonds, shown in Figure 5-6. These regions correspond to the four ground state motifs avail to the system, named after their membership to the possible crystals: primary bonds, which appear in both crystals; hexagonal bonds, only appearing in the hexagonal crystal; herringbone bonds, only appearing in the herringbone crystal; and defect bonds, motifs that disrupt the ability for a crystal to form.

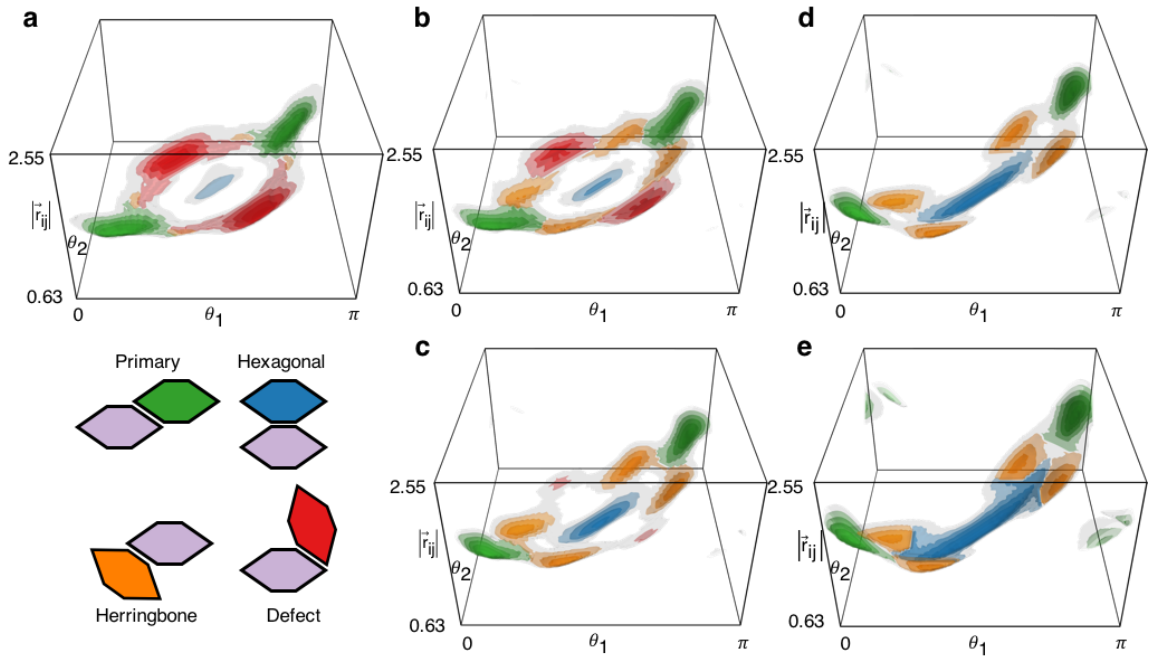


Figure 5-7 Isosurfaces of entropically favorable configurations of elongated rhombs, colored by bond (schematic of bonds included to aid in understanding these free-energy landscapes) for **a** $\gamma = \frac{1}{2}$, **b** $\gamma = \frac{2}{3}$, **c** $\gamma = 1$, **d** $\gamma = \frac{3}{2}$, and **e** $\gamma = 2$ at pressures $P^* = [16.0,14.9,13.5,12.6,12.1]$, respectively. Due to the symmetry of elongated rhombs the entropy density landscape is periodic, repeating every $\pi$; thus, the range of the landscapes is restricted to $\theta_1, \theta_2 \in [0, \pi]$. Excess entropy density isosurfaces indicate regions corresponding to each bond type (isosurfaces corresponding to $\frac{\Delta S}{k_B} = [2.5, 2, 1.5, 1, 0.5]$ shown in lighter coloring). $\Delta S = 0$ is indicated with a gray isosurface for reference. The dimensions of the box are set to include the simplest symmetry ($\theta_1, \theta_2 : [0, \pi]$), while the range for values of $|\vec{r}_{ij}|$ is set to the closest approach for all shapes considered $(\vec{r}_{ij} = 0.63)$ and the farthest distance for which an entropic bond corresponding to a nearest-neighbors position for any of the shapes considered $(\vec{r}_{ij} = 2.55)$.

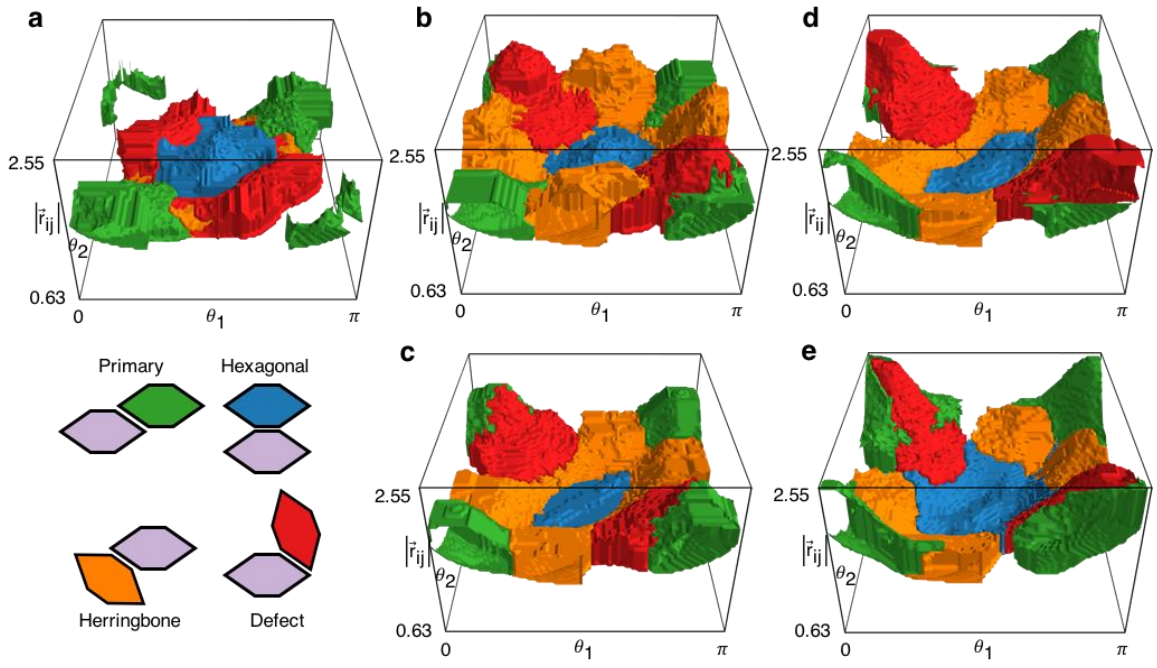


Figure 5-8 Borders of regions belonging to the four different types of bonds in elongated rhomb systems, colored by bond (schematic of bonds included to aid in understanding these free-energy landscapes) for **a** $\gamma = \frac{1}{2}$, **b** $\gamma = \frac{2}{3}$, **c** $\gamma = 1$, **d** $\gamma = \frac{3}{2}$, and **e** $\gamma = 2$ at pressures $P^* = [16.0,14.9,13.5,12.6,12.1]$, respectively. Due to the symmetry of elongated rhombs the entropy density landscape is periodic, repeating every $\pi$; thus, the range of the landscapes is restricted to $\theta_1, \theta_2 \in [0, \pi]$. The dimensions of the box are set to include the simplest symmetry ($\theta_1, \theta_2 : [0, \pi]$), while the range for values of $|\vec{r}_{ij}|$ is set to the closest approach for all shapes considered $(\vec{r}_{ij} = 0.63)$ and the farthest distance for which an entropic bond corresponding to a nearest-neighbors position for any of the shapes considered $(\vec{r}_{ij} = 2.55)$. These regions are used in the calculation of the alluvial diagram (Figure 5-10).

Analysis of the free-energy landscape (Figure 5-7) *via* disconnectivity graphs reveal the reason the hexagonal crystal is always formed in entropy-driven self-assembly. First, I compare the motifs which differ in the two crystal lattices: in every shape, the hexagonal bond is relatively deeper than that for the herringbone bond, even if the herringbone bond is lower in free energy. This means that the hexagonal bond is relatively more stable than the herringbone bond.

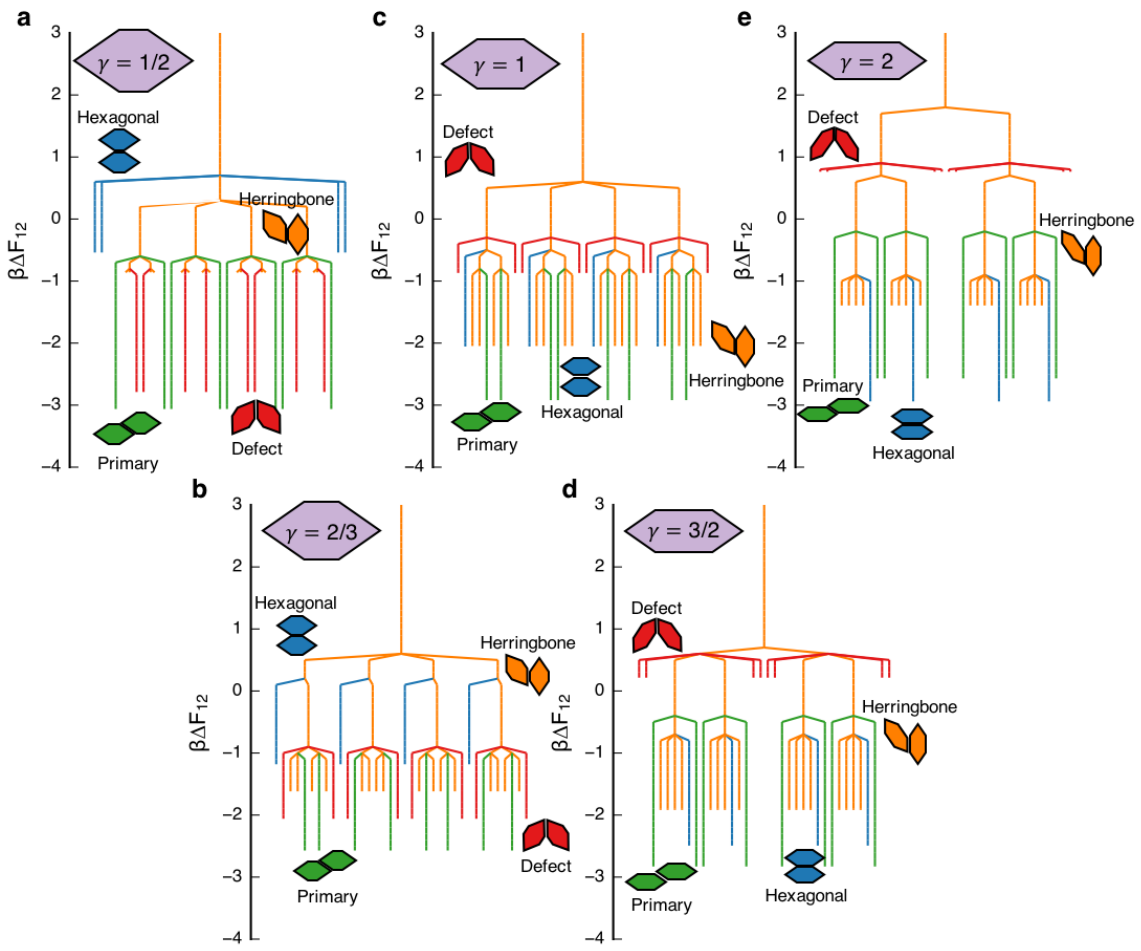


Figure 5-9 Disconnectivity graphs indicating free-energy landscape topology for elongated rhombs at **a** $\gamma = 1/2$; $P = 16.0$, **b** $\gamma = 2/3$; $P = 14.9$, **c** $\gamma = 1$; $P = 13.5$, **d** $\gamma = 3/2$; $P = 12.6$, and **e** $\gamma = 2$; $P = 12.1$. Each leaf represents an entropic bonding motif found at free-energy minima on the landscape, while each node is the free-energy of the meta-basin connecting leaves or nodes. Each line is colored by its corresponding bonding motif. Traversing the graph provides information about the relative free-energy increase required to break a bond, as well as which bonds may directly convert. For example, consider **a** $\gamma = 1/2$: while the relative free energy of a herringbone bond is lower than that of a hexagonal bond, the free energy required to break the herringbone bond is much less than that of the hexagonal bond, indicating that the hexagonal bond is more stable than the herringbone bond, which is more likely to convert to a defect or primary bond. Analysis shows that the combination of bond free energy and the relative free energy required to break a bond lead to the preference for hexagonal bonds over herringbone bonds, leading to the entropy-driven self-assembly of the hexagonal lattice.

This becomes more important when taking the entire local environment of a platelet in a crystal. Each platelet in the hexagonal lattice must form four primary bonds and two hexagonal bonds, which are of lower energy for every $\gamma$ than the four herringbone bonds and two primary bonds found per platelet in the

herringbone lattice (please see Figure 5-12). This explains the heavy preference for the hexagonal lattice over the herringbone lattice.

Analysis of the alluvial diagram (Figure 5-10) also points to the importance of the ground state free-energy of bonds in determining the self-assembled phase. Other than the great increase in the relative volume belonging to herringbone bonds from $\gamma = \frac{1}{2} \rightarrow \frac{2}{3}$, the size of each bonding region is relatively constant for all $\gamma$, indicating that the size of the geometric region belonging to a bond does not govern the self-assembly behavior or the final structure of the system.

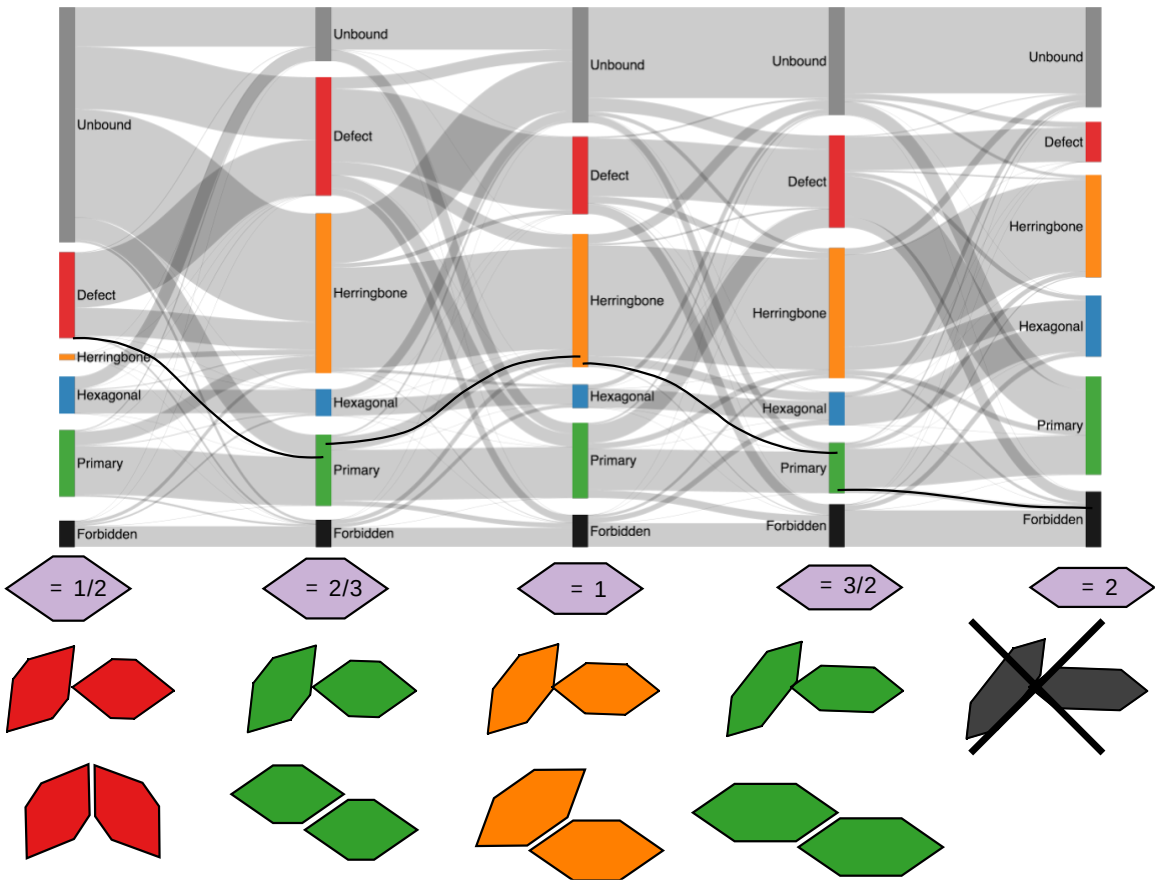


Figure 5-10 Alluvial diagram indicating particle shape modification of bonded state structure in $(r, \theta_1, \theta_2)$ space for elongated rhombs at $P^* = [16.0,14.9,13.5,12.6,12.1]$ for shape parameters $\gamma = \left[\frac{1}{2}, \frac{2}{3}, 1, \frac{3}{2}, 2\right]$. Bar sizes correspond to phase space volume associated with each bond type. Grey lines associate ``flows'' within and between bond types as particle shape changes. Additional bars indicate regions of phase space that change from being associated with bonds to nonbonded or geometrically forbidden states, keeping total phase space volume constant across all shapes. Examples below each shape indicate the same voxel in $(r, \theta_1, \theta_2)$ for each shape, and the corresponding bond, demonstrating how the bonds change as a function of particle shape. The most striking observation is the considerable increase in the voxels belonging to the herringbone bond from $\gamma = \frac{1}{2} \rightarrow \frac{2}{3}$, followed by the reduction in defect voxels from $\gamma = \frac{3}{2} \rightarrow 2$. Observation of the flow between bonding regions as $\gamma$ changes shows that particle shape has a significant impact on entropic bonding regions, suggesting the ability to strategically engineer entropic bonds *via* shape manipulation. See Figure 5-8 for the entropic bonding regions used to compute the alluvial diagram.

Having established that the free-energy associated with the ground state of an entropic bond is the quantity of interested, I use these bond energies to predict the interaction bias $\varepsilon$ required self-assemble the herringbone crystal.

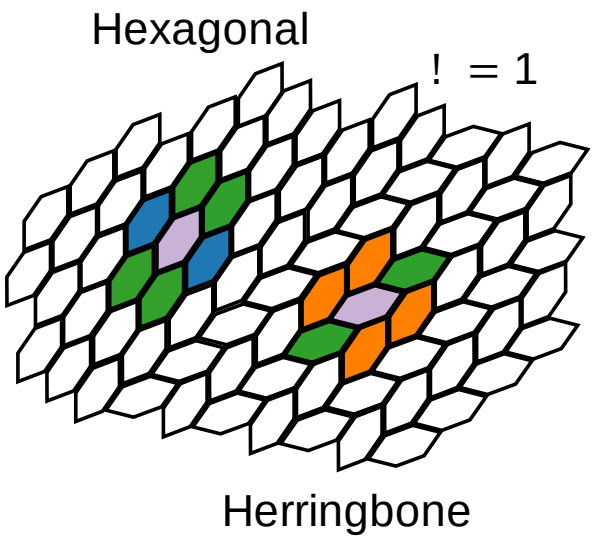


Figure 5-11 Comparison of the hexagonal (lighter blue) and herringbone (lighter orange) lattices at $\gamma = 1$, showing that both lattices tile space at $\gamma = 1$. For both lattices one particle (purple) and the particles to which it forms bonds are highlighted by the color of the bond (Figure 5-6): hexagonal (darker blue), primary (green), and herringbone (darker orange). Note that each particle forms 4 primary bonds and 2 hexagonal bonds in the hexagonal lattice, while each particle forms 4 herringbone bonds and 2 primary bonds in the herringbone lattice.

The equations are worked out here[179].

$$\Delta F = 0 = \Delta F_{\text{l,herringbone}} - \Delta F_{\text{l,hexagonal}}$$

$$= \left(2\Delta F_{\text{primary}} + 4\Delta F_{\text{herringbone}}\right) - \left(4\Delta F_{\text{primary}} + 2\Delta F_{\text{hexagonal}}\right)$$

$$= 4\Delta F_{\text{herringbone}} - \left(2\Delta F_{\text{primary}} + 2\Delta F_{\text{hexagonal}}\right)$$

$$\therefore (1 - \varepsilon) = \frac{2\Delta F_{\text{herringbone}}}{\left(\Delta F_{\text{primary}} + \Delta F_{\text{hexagonal}}\right)}$$

Comparing against the interaction bias determined in simulation (see Figure 5-10), I find good agreement both in terms of magnitude and functional form of the interaction bias. The imperfect alignment can be explained by particle geometry; as these particles are geometric shapes and not point particles, it will be impossible to fully divorce the emergent effect of shape on the assembly behavior of the system. The agreement between the entropic and enthalpic interaction bias, $\varepsilon_S$ and $\varepsilon_H$ indicate that manipulation of particle shape indeed

alters the energetic interactions in the system in a similar manner to chemical functionalization, strengthening the argument that entropic bonds form in systems of hard, anisotropic particles. Further investigation into systems with both entropic and enthalpic interactions should be conducted to better understand how these interactions impact each other.

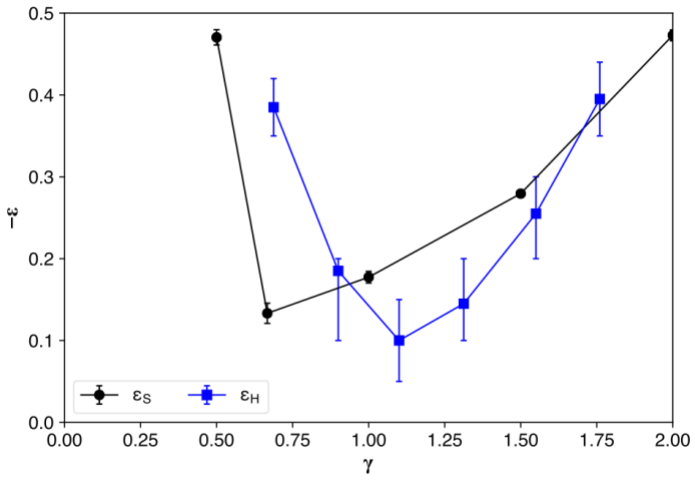


Figure 5-12 Comparison of the enthalpic interaction bias[179] $\varepsilon_H$ and entropic interaction bias $\varepsilon_S$ required to self assemble an alternating/herringbone lattice. Because the simulations used to compute $\varepsilon_H$ account for nanoplatelet shape, $\varepsilon_H$ implicitly contains both entropic and enthalpic contributions. Thus, the difference in the biases results from the addition of enthalpic interactions as shown in Ref. 179[179]. The fact that $-\varepsilon > 0 \; \forall \; \gamma$ indicates that the hexagonal lattice should self assemble for all $\gamma$, as observed in both this study and in Ref. 179[179]. The similarity in functional form and magnitude for both $\varepsilon_H$ and $\varepsilon_S$ indicate that manipulation of nanoplatelet shape alters entropic bonds, resulting in similar changes to the interaction bias as manipulation of the bias *via* chemical functionalization.

## 5.4 Conclusion

I have established that emergent directional entropic forces result in a phenomenon that shares characteristics with hydrogen bonds in systems of liquid water: free-energy calculations can limit the region associated with a local motif to a specific geometric region, and the probability that a pair of particles remains in that region has the same functional form as that of systems exhibiting hydrogen bonding. Additionally, the differences between ground state free-

energy associated with local motifs can account for the self-assembly behavior of hard particle systems, predicting similar interaction bias as those obtained with systems with chemical functionalization/enthalpic patches. Due to the overwhelming similarity between this phenomena and chemical bonds, I establish the existence of an emergent entropic bond.

# Chapter 6

# Entropic Bonds and Phase Transitions in Two-Dimensional Systems

## 6.1 Introduction

The assembly behavior of hard polygon systems is applicable to a variety of real-world systems, at both the molecular[112,192–196] and nano-/colloidal-scale[80,83,179,197–202]. As discussed in previous chapters, such driving force toward self-assembly arises from *enthalpic*[112,192,196,197] and/or *entropic*[60,82,138,173,179] interactions. Viewing such interactions as bonds facilitates analogy with intermolecular interactions. For example, shape manipulation alters the strength of entropic bonds, serving as an alternative to chemical functionalization while achieving a similar interaction bias[173,179].

Among polygons, the self-assembly behavior of rhombs is of particular interest[203–207] because of their application to the study of molecular tilings[112,192–194,197]. A rhombus (shown in Figure 6-1) may fill space in one of three different patterns: parallel, herringbone, or rhombille. Previous studies show that hard rhombuses self-assemble a random tiling phase in the absence of other interactions[112,192,193]. This RTP is a mixture of the three different tilings[112], shown in Figure 6-1. Manipulation of enthalpic or entropic interactions alters the preferred self-assembled structure[112]. For example, any of the three tilings may

be directed to form *via* addition of specific interactions between different sides of the hard rhombus. Similarly, manipulating the acute angle $\alpha$ alters the thermodynamically preferred structure. Experimental studies of hard rhombs also indicate the importance of shape on self-assembly behavior: colloidal scale rhombs exhibit unexpected phases, including hexatic and rotator phases, due in part to the rounding of their vertices[197]. Similarly, altering the aspect ratio of the rhombs *via* elongation, similarly alters the observed self-assembly behavior[173,179].

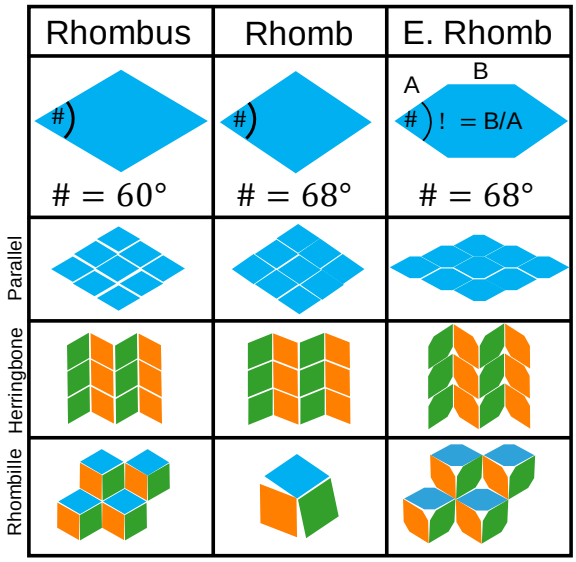


Figure 6-1 Table showing the difference between a rhombus ($\alpha = 60°$), a rhomb ($\alpha \neq 60°$), and elongated rhomb ($\alpha \neq 60°, \gamma > 0$). Also shown are the different tiling motifs they may form. Elongated rhombs are defined by their aspect ratio, $\gamma = \frac{B}{A}$, in addition to the acute angle $\alpha$. In this figure, shapes are colored by their orientation to aid in identification of the orientations found in the different tiling motifs. In this study, only rhombs with $\alpha = 68°$ are considered, while investigating different aspect ratios: $\gamma = \left[0, \frac{1}{4}, \frac{1}{3}, \frac{5}{12}, \frac{1}{2}, 1\right]$. Note that the herringbone tiling is only space filling for $\gamma = 0,1$. While free space exists in the rhombille motif for the elongated rhombs, the additional side reduces the strained induced from $\alpha \neq 60°$, providing an avenue to stabilize this motif, required for the formation of the RTP.

Here I investigate the self-assembly behavior of hard, elongated rhombs, demonstrating the ability to alter the number and type of phase transitions observed by manipulating particle shape, specifically by altering the aspect ratio $\gamma$. The 1$^{st}$-order phase transition from a fluid to a parallel ordered solid observed for elongated rhombs with an aspect ratio of $\gamma > 0.5$[173] changes as $\gamma$ decreases,

giving rise to an intermediate random tiling phase (RTP), with an observed fluid-to-RTP transition, and a 1st-order RTP-to-ordered phase transition. To better understand the underlying entropic mechanism resulting in this behavior, I calculate the potential of mean force and torque (PMFT) in the dense fluid phase for these elongated rhombs, determining the emergent entropic bonds that result in the formation of the RTP. Analyzing this free-energy landscape with the language of entropic bonding provides a deeper understanding of the underlying self-assembly mechanism, helping to explain the observed phase behavior.

## 6.2 Methods

Systems of hard, elongated rhombs are simulated in the $NPT$ ensemble using HOOMD-blue[87,93,125,126] with HPMC[93]. $N = 16{,}384$ particles are initialized in the parallel lattice and run to equilibrium at the target pressure. Hard particles start in the parallel crystal lattice at a density of $\phi = 0.8$. The pressure is set at the final desired scaled pressure, $P^* = \beta P \sigma^2$ where $\sigma^2 = A_{\text{rhomb}} = 1.0$. These systems run to equilibrium, as determined by system volume fluctuations. I calculate the equation of state by averaging over decorrelated simulation frames in equilibrium.

Visual analysis of these systems utilizes the body-orientation order parameter[108] (shown in Figure 6-2) to color each particle, allowing for visual identification of phases. The body-orientation order parameter is calculated as $\xi_k^i = e^{ik\theta_i}$, where $\theta_i$ is the orientation of particle $i$, and $k$ is the symmetry of the particle. For these elongated rhomb systems, $k = 2$. The orientation-orientation hexatic order parameter, $\Psi_{6,6}$[112]. This order parameter differs from the hexatic order parameter

that uses the orientation of the nearest neighbors of particle $i$[108,110], instead using the real part of the difference in the orientation of a particle and its $N$ nearest neighbors: $\Psi_{6,6} = \frac{1}{6}\sum_{j\in \mathrm{NN}(i)}^{N} \cos\left(6 \cdot \theta_{ij}\right)$, where $\theta_{ij} = \theta_i - \theta_j$. While the body-orientational order parameter, $\xi_k^i$, provides for visual determination of the phase, the orientation-orientation hexatic order parameter, $\Psi_{6,6}$, quantifies these phases. $\Psi_{6,6} \to 0$ corresponds to the fluid phase, while $\Psi_{6,6} \to 1$ corresponds to the parallel ordered solid phase. Intermediate values of $\Psi_{6,6}$: $0.5 \leq \Psi_{6,6} \leq 0.75$ correspond to the RTP, due to the strong preference for locally-aligned orientational order.

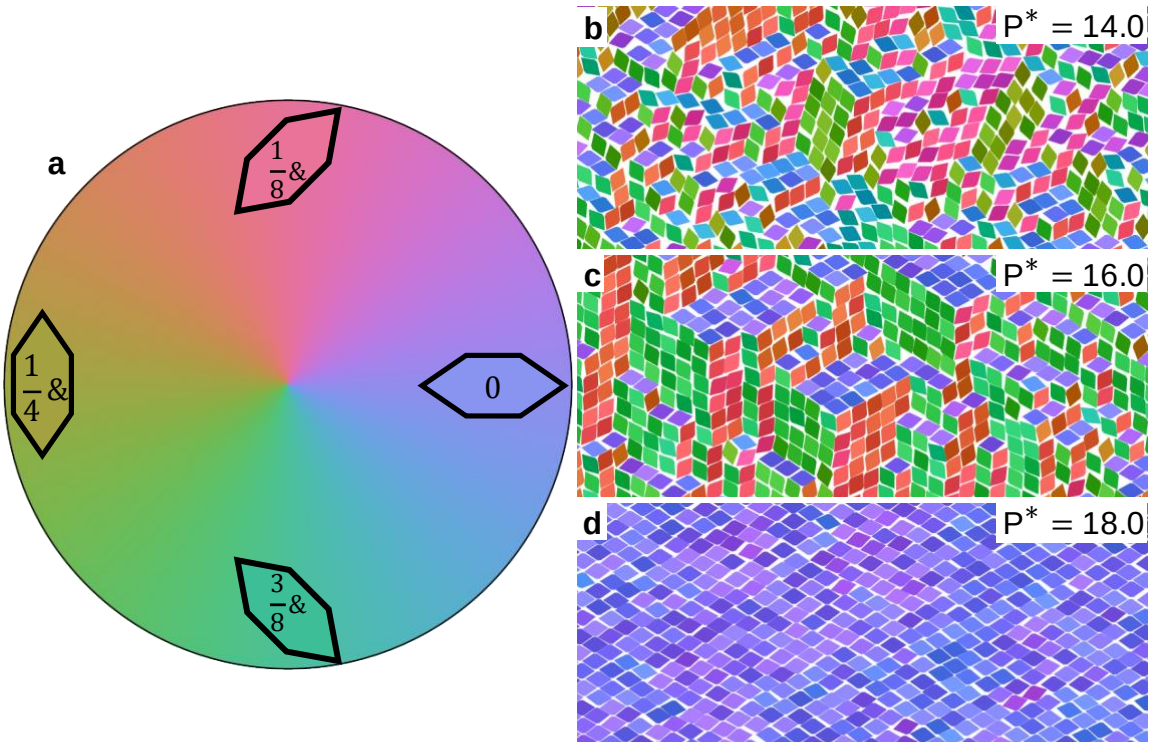


Figure 6-2 **a** Body-orientation order parameter $\left(\xi_2^i\right)$ on the cube ellipse color wheel used to visually analyze and identify phases found in systems of elongated rhombs (here shown for $\gamma = \frac{1}{4}$): **b** fluid, **c** RTP, and **d** parallel phase. The fluid and parallel phases are observed in all values $\gamma$ investigated here, while the RTP phase is only observed for $0 \leq \gamma \leq \frac{1}{3}$.

Analysis of the equation of state identifies the phase transitions present. 1st-order phase transitions accompany discontinuities in the equation of state, while equations of state lacking discontinuities are identified as having a continuous phase transition. I estimate the range of pressures over which the phase changes for continuous transitions by fitting a 1st-order polynomial ($P^* = m\phi + b$) to the regions of the equation of state before, during, and after the transition (shown in Figure 6-3). Intersections between these polynomials are the bounds for the phase transition. The midpoint between the intersections is the center of the continuous phase transition window.

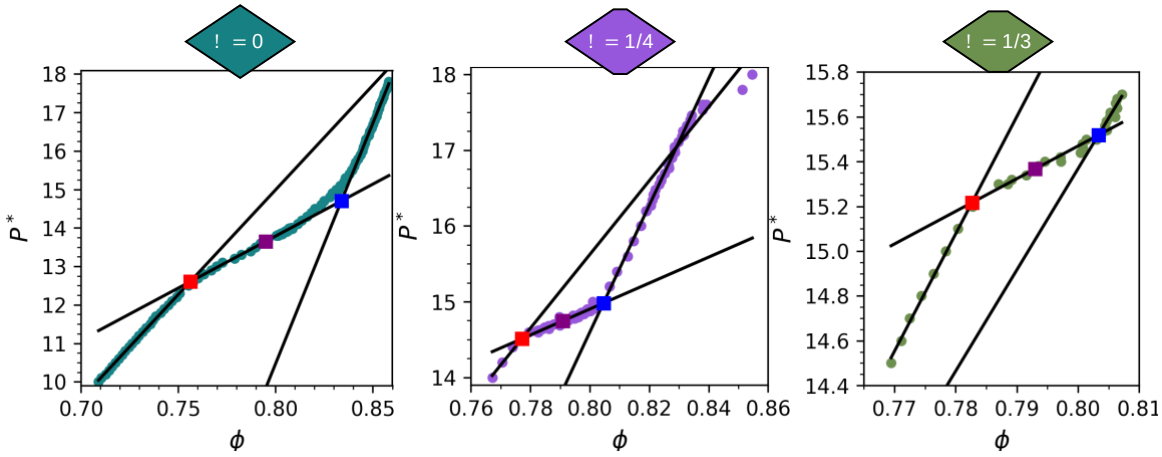


Figure 6-3 Use of 1st-order polynomials to fit the equation of state for $\gamma = 0, \frac{1}{4}, \frac{1}{3}$ to identify the continuous phase transition window. The polynomial fits are shown as black lines, with intersections marking the bounds of the transition: red marking the start of the transition, and blue marking the end of the transition. The midpoint on the second curve (marked in purple) is the center of the transition window. The phase diagram (Figure 6-5) plots the center of the transition window with error bars extending from the beginning (red) to the ending (blue) of the phase transition.

The potential of mean force and torque (PMFT) provides a measure of the emergent directional entropic forces present in these systems[60,82,138,173]. I sample the equilibrium distributions of the dense fluid-phase, calculating the PMFT in the $(r, \theta_1, \theta_2)$ coordinate system. Watershed image segmentation[104] yields a free-

energy (entropy density) landscape, with each voxel belonging to a specific entropic bonding motif, as shown in Figure 6-4**a**. The ideal gas distribution serves to normalize the PMFTs, with the free-energy of the ideal gas being assigned a value of zero: $\beta\Delta F_{12} = 0$. Thus, regions of the PMFT with $\beta\Delta F_{12} < 0$ correspond to preferred arrangements (more likely than an ideal gas), while $\beta\Delta F_{12} > 0$ correspond to less-likely geometric arrangements. The densest stable fluid most effectively provides information about the directional entropic forces leading to the self-assembled structures. As a result, the PMFT must be calculated as close to the fluid phase transition as possible i.e. in the densest/highest pressure fluid observed. This is trivial for the 1st-order fluid-to-crystal transitions $\left(\gamma > \frac{1}{3}\right)$, but is more challenging for the continuous phase transitions $\left(\gamma \leq \frac{1}{3}\right)$. However, the continuous phase transition implies that any changes to the strength of the directional entropic forces by the PMFT, as well as any changes to the topology of the free-energy landscape, should be minimal as the fluid transitions to the RTP. Thus, I choose a $P^*$ in the transition region close to the lower-end of the transition at which to calculate the PMFT: $\gamma = 0, P^* = 12.3; \gamma = \frac{1}{3}, P^* = 14.6; \gamma = \frac{1}{4}, P^* = 15.3$.

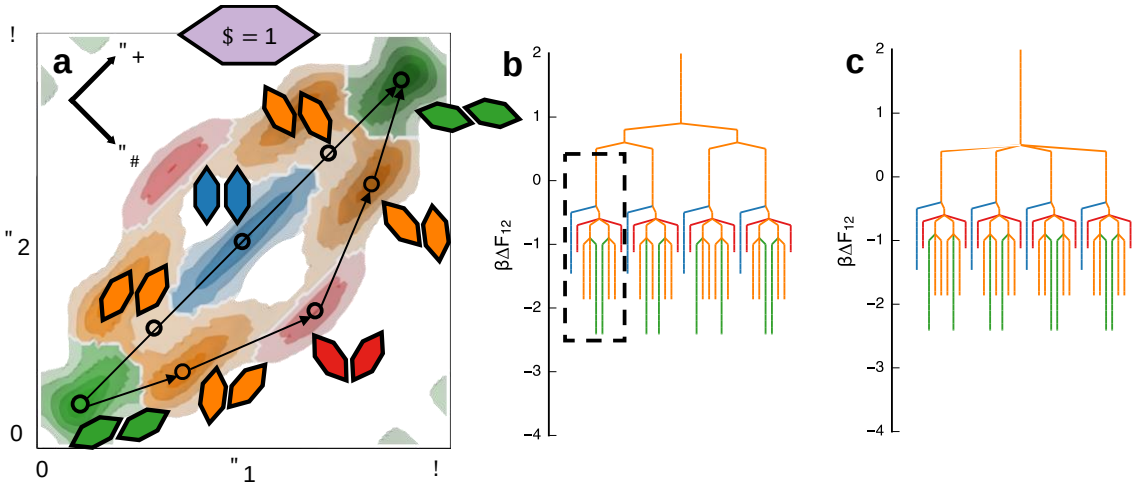


Figure 6-4 Example of an entropic bonding transition for $\gamma = 1$. **a** Orthographic view of the $(\theta_1, \theta_2)$ plane of the PMFT, showing two different transition paths between two primary bonds: one through the hexagonal bond, and one through the rhombille bond. Schematics of the bonding motifs are inset. Entropic bonding regions are colored by the bonding motif: primary (green), hexagonal (blue), herringbone (orange), and rhombille (red). Constant energy isosurfaces are shown, corresponding to $\beta\Delta F_{12} = [-2, -1.5, -1, -0.5]$, with lower free energies shown in increasingly darker colors. $\theta_1$ and $\theta_2$ are limited to $[0, \pi]$ due to the two-fold symmetry of the rhomb ($k = 2$). Note the transition through the hexagonal bond follows the $\theta_+$ (shear) direction, indicating that both elongated rhombs rotate counter-clockwise to transition between the three bonds. Disconnectivity graphs **b** excluding and **c** including 2nd nearest-neighbor motifs. The transitions shown in **a** are shown in the dashed box in **b**. To transition to either a hexagonal or rhombille bond, the primary bond must pass through the region belonging to the herringbone bond. However, the transition through the herringbone bond is of higher free energy for the primary-to-hexagonal transition than for the primary-to-rhombille transition. Note the difference between **b** and **c**: inclusion of the 2nd nearest-neighbors in **c** change the connectivity and free-energy of the transition between herringbone motifs, indicating the transitions involving 2nd nearest-neighbors are more energetically favorable than those only involving 1st nearest-neighbors.

Disconnectivity graph analysis[105,208,209] of the free-energy landscapes (see the example in Figure 6-4) provides for comparison between entropic bonding states and transition states for different shape parameters. The three-dimensional PMFT is reduced to a two-dimensional graph: local free-energy minima are represented as leaves, and connected meta-basins are represented as nodes connected the minima. Disconnectivity graph analysis may consider or exclude 2nd nearest-neighbor motifs, providing information about the importance of 2nd nearest-neighbors in fluid-phase motif rearrangement. Analysis of both the free energy of an entropic bond, as well as the relative increase in free energy

required to break a bond, provide information about the stability of these entropic bonds and how they influence the final self-assembled structure.

## 6.3 Results and Discussion

Elongated rhombs $\left(\gamma = \left[0, \frac{1}{4}, \frac{1}{3}, \frac{5}{12}, \frac{1}{2}, 1\right], \alpha = 68°\right)$ form three different phases, depending on the state point: fluid (Figure 6-2**b**), RTP (Figure 6-2**c**), and an ordered parallel solid (Figure 6-2**d**). The parallel solid is a centered rectangular crystal lattice, shown in Figure 6-1. The RTP forms as an intermediate phase between the fluid and solid phases for $\gamma: 0 \leq \gamma \leq \frac{1}{3}$. Table 1 and Table 2 show the pressures and phase transitions present in each investigated shape.

Table 1: Summary of the pressure $P^*$ at which phase transitions occur in systems of hard rhombs at a given shape parameter $\gamma$.

| $\gamma$ | fluid-to-RTP | RTP-to-crystal | fluid-to-crystal |
|---|---|---|---|
| $\gamma = 0$ | $P^* = 13.57 \pm 1.27$ | | - |
| $\gamma = 1/4$ | $P^* = 14.75 \pm 0.24$ | $P^* = 17.8 \pm 0.1$ | - |
| $\gamma = 1/3$ | $P^* = 15.37 \pm 0.15$ | $P^* = 15.7 \pm 0.05$ | - |
| $\gamma = 5/12$ | - | | $P^* = 14.4 \pm 0.05$ |
| $\gamma = 1/2$ | - | | $P^* = 14.0 \pm 0.05$ |
| $\gamma = 1$ | - | | $P^* = 12.6 \pm 0.05$ |

Table 2 Summary of the value of the shape parameter $\gamma$ and the phase transitions exhibited by the system.

| $\gamma$ | fluid-to-RTP | RTP-to-crystal |
|---|---|---|
| $\gamma = 0$ | continuous | |
| $\gamma = 1/4$ | continuous | 1st-order |
| $\gamma = 1/3$ | continuous | 1st-order |
| $\gamma = 5/12$ | 1st-order | |

| | |
|---|---|
| $\gamma = 1/2$ | 1st-order |
| $\gamma = 1$ | 1st-order |

Analysis of the equation of state (Figure 6-5**a**) and phase diagram (Figure 6-5**c**) shows that the order of the phase transition changes as a function of the aspect ratio $\gamma$. The presence of discontinuities in the equation of state (Figure 6-5**a**) for higher values of $\gamma$: $\gamma \geq \frac{5}{12}$ indicates that the fluid-to-solid phase transition is 1st order. For lower values of $\gamma$: $\gamma \leq \frac{1}{3}$, the RTP appears, exhibiting a continuous transition between the fluid and RTP, and a 1st-order transition between the RTP and ordered solid for $\gamma \geq \frac{1}{4}$. For $\gamma = 0$, both the fluid-to-RTP and RTP-to-ordered solid transitions are continuous. These transitions are summarized in Table 2 and the phase diagram in Figure 6-5**c**, showing the persistence of the RTP beyond $\gamma = 0$, with the 1st-order transition between the RTP and ordered solid phases for $0 \leq \gamma \leq \frac{1}{3}$.

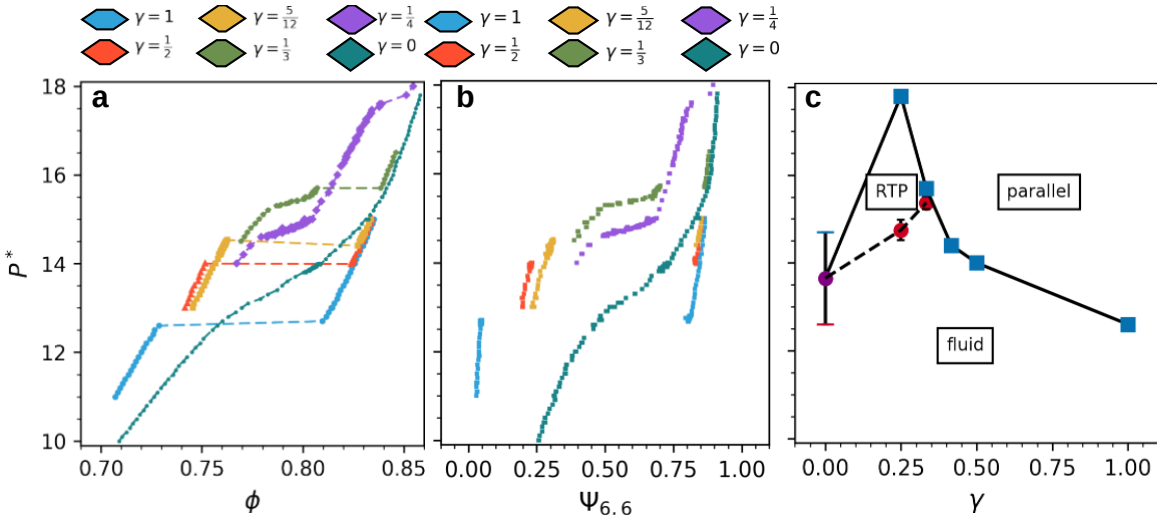


Figure 6-5 **a** Equation of state and **b** Orientation-orientation hexatic order paramete for elongated rhombs with shape parameter $\gamma = \left[0, \frac{1}{4}, \frac{1}{3}, \frac{5}{12}, \frac{1}{2}, 1\right]$. Note the 1st-order phase transitions between fluid and ordered solid phases for $\gamma \geq \frac{5}{12}$, in contrast with the continuous fluid-to-RTP transition observed for $\gamma \leq \frac{1}{3}$. Both continuous and 1st-order transitions are present for $\gamma = \frac{1}{4}, \frac{1}{3}$. While the RTP is stable for $\gamma = \frac{1}{4}$ over a relatively large pressure window $\Delta P^* \approx 2.0$, the RTP is only stable for $\Delta P^* \approx 0.5$ for $\gamma = \frac{1}{3}$. The orientation-orientation hexatic order parameter $\Psi_{6,6}$ shows the same phase transitions as the equation of state. The values of $\Psi_{6,6}$ for the different shapes indicate which motifs are preferred in the dense fluid phase. For $\gamma = 1, \Psi_{6,6} \to 0$, indicating that herringbone and hexagonal bonds compete equally in the fluid phase, resulting in an overall lack of orientational order congruent with either RTP or parallel phases. The fact that $\Psi_{6,6} > 0$ indicates that the hexagonal bonds are preferred, as observed in Ref. 173[173]. As the value of $\gamma$ decreases, the value of $\Psi_{6,6}$ in the fluid phase increases, indicating an increased preference for hexagonal to herringbone order. For $\gamma \leq \frac{1}{3}$, values of $\Psi_{6,6}$ associated with the RTP are observed, indicating the presence of the RTP phase. **c** Phase diagram constructed from **a** and **b**. Red dots represent the edge of the fluid phase connected by dashed lines representing the continuous transition between the fluid and RTP. Blue squares represent the solid phase, connected by a solid line representing the 1st-order phase transition between the RTP or fluid and parallel phases. The continuous-continuous phase transition for $\gamma = 0$ is plotted with a purple circle with error bars estimating the edges of the fluid (red line) and crystal (blue line) phases. Please reference Figure 6-3 for how these phase transitions are estimated. These phase transitions are detailed in Table 1 and Table 2.

Previous study of hard rhombs indicates that the preferred self-assembled phase is the parallel ordered phase[112]. The accessibility and stability of the RTP is unexpected because of the induced strain in the rhombille motif due to the inability for three rhombs to assemble a perfect hexagonal motif[112]. As shown in Figure 6-1, the rhombs studied here are not the rhombus, having an internal acute angle of $\alpha = 68°$. However, at intermediate densities, there is enough free volume per particle to allow the imperfect hexagon motif to exist without

disrupting the development of long-range ordering. If fact, the elongation of rhombs, for at least some values of $\gamma$, should help stabilize the formation of hexagons due to the reduction in the strain introduced through the larger value of $\alpha$.

Analysis of $\Psi_{6,6}$ shows that the primary, hexagonal, and rhombille motifs are preferred as $\gamma$ decreases. This preference is explained through the analysis of the free-energy landscape. The decrease in the entropic bonding energy of the primary, hexagonal, and rhombille bonds (increasing the depth of their bonding free-energy wells) increases their stability, resulting in the increase in the value of the order parameter. This is also due to the increase of the free energy of the herringbone bond (decrease in the depth of the free-energy well), decreasing its stability.

Analysis of the free-energy landscapes (Figure 6-6) show topological differences between lower and higher values of $\gamma$. At low values of $\gamma$, for example, $\gamma = 0$ (Figure 6-6**a**-**c**) the herringbone bonding motif is absent, and there exist no low-energy pathways connecting primary and rhombille bonds, or hexagonal and rhombille bonds, while there are low-energy transitions between primary and hexagonal bonds. This inhibits transitions to or from rhombille bonds from either primary or hexagonal bonds while allowing for the transition between primary and hexagonal bonds. Further analysis shows that there exist low-energy pathways between rhombille bonds and 2$^{nd}$ nearest-neighbor motifs, indicating that for low values of $\gamma$, rhombille bonds prefer to transition to/from 2$^{nd}$ nearest-neighbor motifs, rather than transition to/from primary or hexagonal bonds. This is in

contrast to higher values of $\gamma$, for example, $\gamma = 5/12$ (Figure 6-6**d**-**f**). All entropic bonding motifs are present and connected by low-energy transition pathways. This allows for these bonds to interconvert rather than require the use of 2$^{nd}$ nearest-neighbors. Observation of the shear and twist landscapes (Figure 6-6**e**,**f**) support this conclusion, as the low-energy pathways between the rhombille and 2$^{nd}$ nearest-neighbors are no longer present.

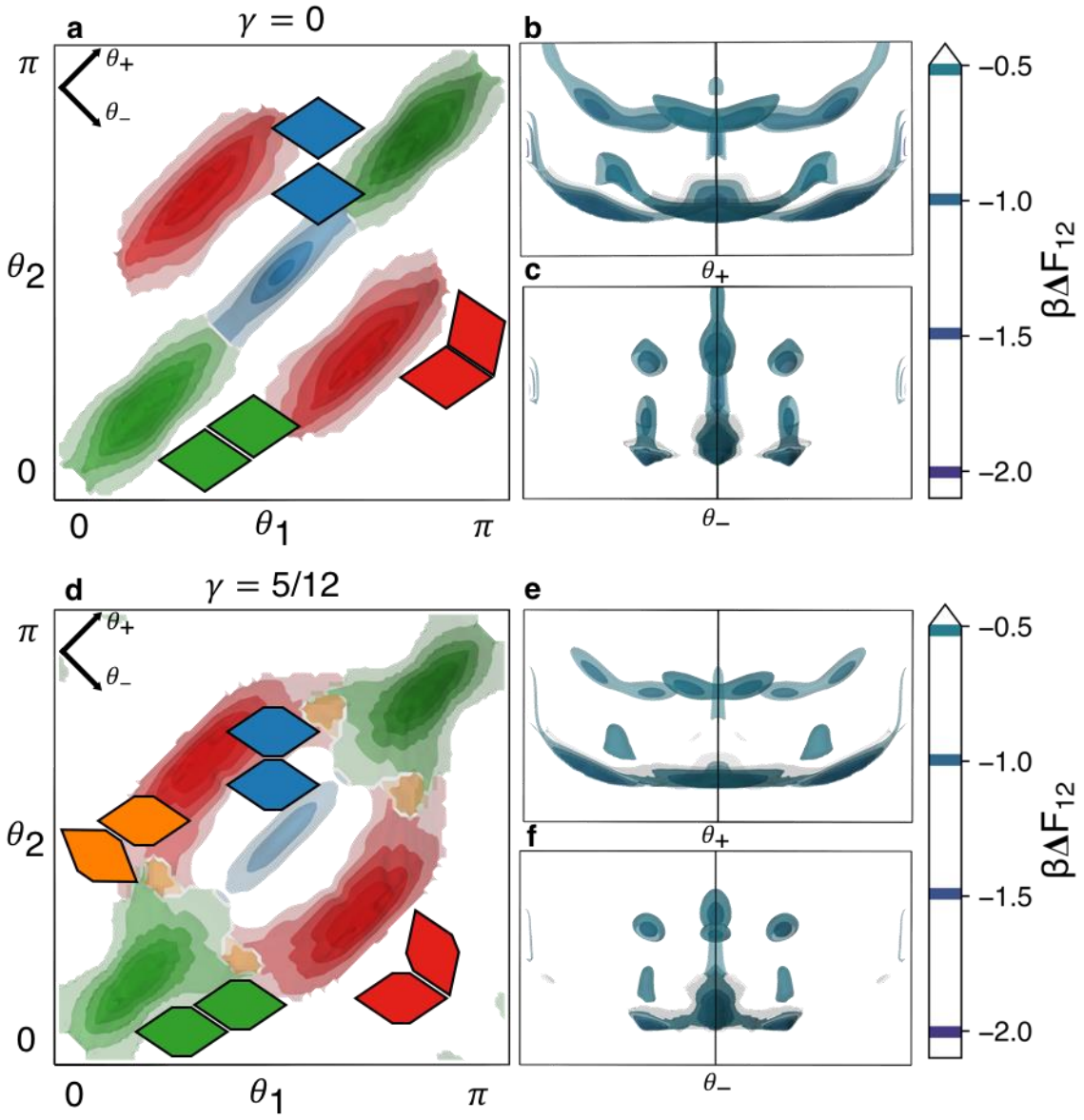


Figure 6-6 Fluid-phase entropic bonding free-energy landscapes for **a** $\gamma = 0$ and **d** $\gamma = \frac{5}{12}$, showing an orthographic view of the $(\theta_1, \theta_2)$ plane, with color-coded bonding regions: parallel (green), hexagonal (blue), herringbone (orange), and rhombille (red). Note that only regions of the free-energy landscape belonging to entropic bonds (1st nearest-neighbors) are shown. Constant energy isosurfaces are shown, corresponding to $\beta\Delta F_{12} = [-2, -1.5, -1, -0.5]$, with lower free energies shown in increasingly darker colors. $\theta_1$ and $\theta_2$ are limited to $[0, \pi]$ due to the two-fold symmetry of the rhomb $(k = 2)$. Orthographic views of the **b**, **e** $\theta_+$ (shear) and **c**, **f** $\theta_-$ (twist) directions. These views are colored by free energy, showing preferred motifs and transitions between them in the free-energy landscape, including 2nd nearest-neighbors. Grey regions of $\beta\Delta F_{12} = 0$ are included for reference. Rhombs ($\gamma = 0$, **b**, **c**) do not possess low-energy pathways between the primary and rhombille motifs, nor is there a low-energy herringbone motif, in contrast to $\gamma = 5/12$ (**e**, **f**). This shows the difficulty for transitions between primary, hexagonal, and rhombille motifs that arises as $\gamma$ decreases. There exist low-energy pathways between all motifs for higher values of $\gamma$.

Disconnectivity graph analysis reinforces this conclusion (Figure 6-7). The topology clearly changes as the value of $\gamma$ increases. At lower values of $\gamma$ (Figure

6-7**a,** $\gamma = 0$), the lowest-energy pathways facilitate interconversion of the primary and hexagonal bonds, while interconversion to the rhombille motif requires a higher-energy transition. Comparison of the graphs utilizing 2nd nearest-neighbors for transitions (Figure 6-7**a**, top) and those that don't (Figure 6-7**a**, bottom) shows that transition between the rhombille and 2nd nearest-neighbor motifs is of lower energy, and is therefore preferred to transitions directly between 1st nearest-neighbor motifs. This is also the case for $\gamma = 1/3$ (Figure 6-7**b**): without the use of 2nd nearest-neighbor motifs, primary-hexagonal and herringbone-rhombille transitions are more favorable. Thus, I conclude that lower $\gamma$ shapes prefer the parallel and rhombille motifs in the fluid phase. These motifs lack low-energy transition pathways, making interconversion difficult. This helps to stabilize the RTP as an intermediate phase. The RTP remains stable until the system pressure allows for the higher-energy pathways to become viable, allowing the system to adopt the space-filling parallel configuration. At higher values of $\gamma$, the ability for primary, herringbone, and rhombille bonds to interconvert stabilizes the fluid phase and prevents the RTP from forming, making direct transition to the parallel phase possible.

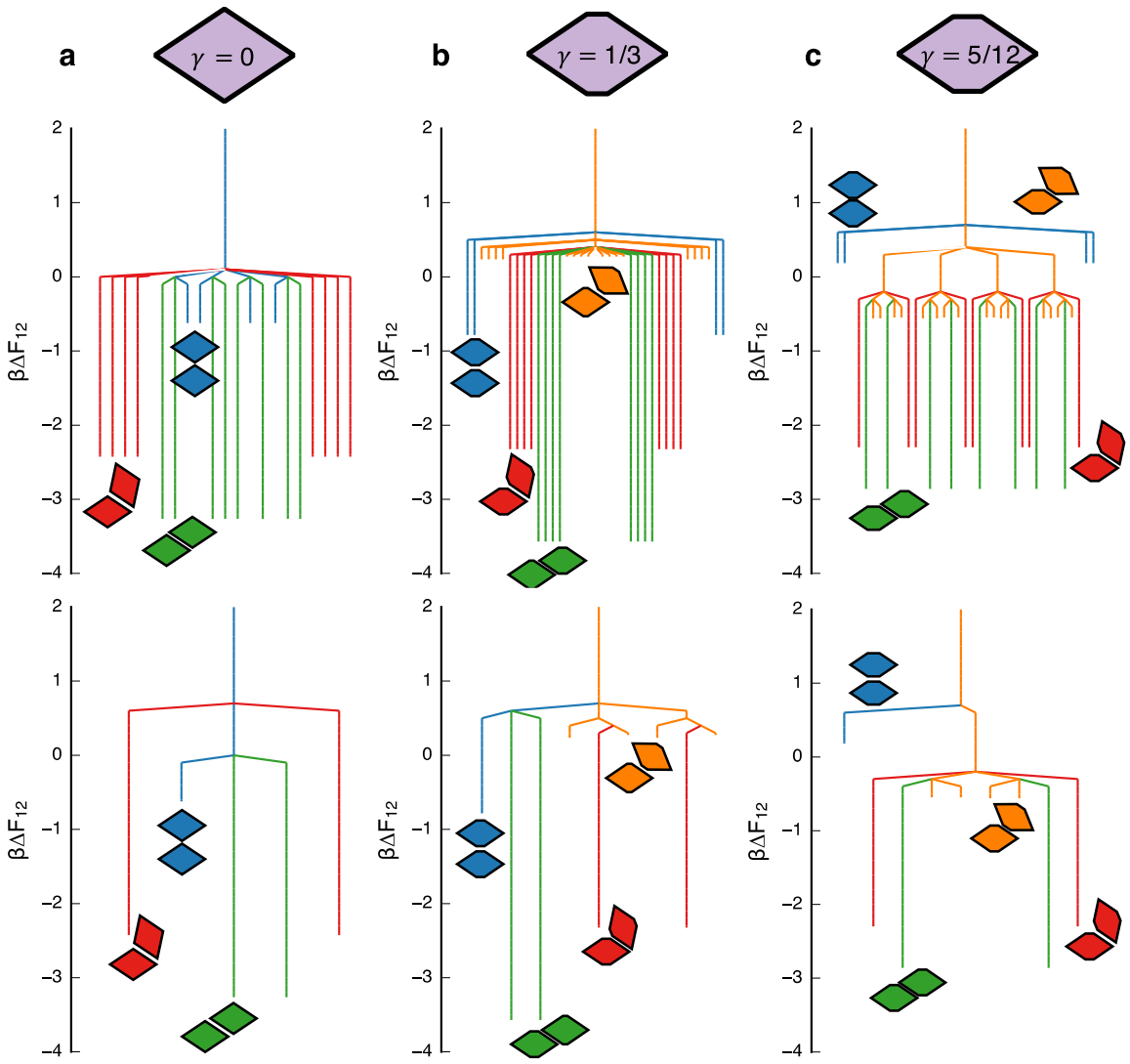


Figure 6-7 Disconnectivity graphs for three values of $\gamma$: $\gamma = \left[0, \frac{1}{3}, \frac{5}{12}\right]$. The top row takes 2nd nearest-neighbors into account, allowing transitions to be made through nearest-neighbor meta-basins. The bottom row only considers the 1st nearest-neighbors and transitions between them. The smaller 1st nearest-neighbor graphs indicate that 2nd nearest-neighbors are required to completely explore the free-energy landscape. As discussed in Figure 6-6, the transitions between primary and hexagonal bonds are of lower energy than for transitions to rhombille bonds, and are therefore preferred for $\gamma = 0$. Comparison to the plot accounting for 2nd nearest-neighbors indicates that transitions to/from rhombille bonds are preferred through the 2nd neighbor shell. For $\gamma = 1/3$, primary and hexagonal bonds prefer to interconvert, as do herringbone and rhombille bonds. For $\gamma = 5/12$, the conversion between primary, herringbone, and rhombille become preferred to transitions to the hexagonal bonding motif.

Previous studies considered the role that emergent directional entropic forces play in the self-assembly and phase behavior of polygonal systems[108,210]. Like these studies, phase transitions that differ from the canonical KTHNY two-dimensional melting transitions are discovered[211–214]. However, these studies do

not consider the manipulation of a continuous shape parameter, instead altering the number of sides of a regular polygon. This results in both the symmetry of the polygon, as well as the symmetry of the solid phase. Here I show that the number of phases and transitions between them may be manipulated without changing either the symmetry of the shape or the symmetry of the crystal lattice. The shapes investigated here are perfectly hard and sharp, in contrast to experimental systems, which are rarely as hard or as sharp[197]. These "imperfections" in experimental systems are a type of shape parameter, similar to the aspect ratio $\gamma$ considered here, altering the predicted self-assembly behavior, resulting in the formation of unexpected phases and phase transitions[197]. While the hexatic and rotator phases report in Ref. 197[197] were not observed, the rounded nature of the colloidal rhombs could partially explain the observance of these phases, as rounder particles tend to behave more similarly to disks, forming hexatic phases[108]f. Computation and analysis of the free-energy landscapes of rounded rhombs should be considered, as such analysis should reveal entropic bonds that result in the formation of hexatic and plastic crystal phases[210].

## 6.4 Conclusions

I demonstrated that changing the shape of a hard, anisotropic particle alone is enough to alter existing phases and phase transitions present in a system, without altering the underlying symmetry of either the particle or self-assembled phase. Calculation of the PMFT and associated entropic bonds demonstrate the ability to control the preferred pair motifs by manipulating the shape of these

elongated rhombs. Analysis of the free-energy landscape shows this can be explained *via* an understanding of the transitions between entropic bonding motifs: when competing motifs are connected by higher-energy transition pathways and are therefore less likely to interconvert, an intermediate phase may be stable, if the competing motifs form intermediate structures compatible with such a phase.

Further investigation into the manipulation of particle shape and the resulting self-assembly behavior will enable the creation of reconfigurable materials with multiple phases and controllable phase transitions. The “imperfections” found in experimental systems, such as rounded vertices, may serve as tunable shape parameters, similar to the aspect ratio investigated in this chapter. As in Ref. 197[197], the ability to manipulate such parameters will enable the ability to direct the self-assembly of a given shape into different self-assembled geometries. The creation of reconfigurable materials made from nano- and colloidal-scale tiles will require the understanding of their assembly dynamics. Thus, the dynamics of entropic bond rearrangement should be further investigated, to determine if there exist kinetic barriers that prevent the realization of the predicted phases and transitions.

# Chapter 7

# Conclusion

## 7.1 Summary

In this thesis, I detail the ways in which emergent directional entropic forces result in the formation of entropic bonds between hard, anisotropic nanoparticles, directing and stabilizing the self-assembly of ordered nanostructures. In Chapter 2 I discuss the methods used in the analysis of these systems, focusing on the calculation of the potential of mean force and torque PMFT), and how analysis of this potential yields information about the entropic bond.

In Chapter 3, I investigate the hierarchical self-assembly of a two-dimensional hard square lattice from 2:1 rectangles and right-isosceles triangles. These basic shapes do not self-assemble the desired square lattice, and analysis of the PMFT shows how the emergent directional entropic forces prevent the desired assembly behavior. Through the use of allophilic patterning, the desired square lattice may be achieved. Analysis of the PMFT shows how allophilic shaping results in the formation of effective entropic bonds.

Three-dimensional hierarchical self-assembly is then investigated in Chapter 4. I consider similar shapes to those in Chapter 3, 2:1 rectangular prisms and right-isosceles triangular prisms, as well as other shapes derived from hard cubes. I observe the self-assembly behavior of these systems, identifying a previously

unverified cubatic phase in 2:1 rectangular prisms. By analyzing the pair motifs that form in the dense fluid phase as a result of the emergent directional entropic forces, I explain the observed self-assembly behavior, developing rules for the design of hierarchically self-assembling particles.

In Chapter 5 I investigate systems of hard hexagonal nanoplatelets. By calculating and analyzing the PMFT for these particles, I quantify the entropic bonds formed between these particles. Modifying the shape of these nanoparticles modifies the bonds they form; analysis of these bonds explains the observed self-assembly behavior, as well as providing insight into the way these particles may be manipulated to direct their self-assembly.

Finally, in Chapter 6, the phase behavior of the system of hexagons in Chapter 5 is investigated, showing how the strength of the entropic bonds effects the number and kind of phase transitions observed. Manipulation of nanoparticle shape alters which entropic bonds are preferred by the system, as well as the preferred transition pathways between these bonds. The ability to control phase transitions *via* relatively simple shape manipulation will enable the creation of novel reconfigurable materials.

## 7.2 Outlook

Together, these studies give us a greater understanding of the entropic bond, as well as how this bond may be engineered to create new classes of materials. Chemical functionalization is a very common way to alter, direct, and control the self-assembly of nanoparticles and colloids. By accounting for the entropic bonds

present in the system, more effective chemical functionalization can be applied to nanosystems, opening the way to new classes of designer materials.

### 7.2.1 Comparison to other bonds

As discussed in Chapter 5, while entropic bonds deserve to be held in similar esteem to traditional chemical bonds, they are not chemical bonds. Chemical bonds may be tuned in traditional chemical systems *via* the use of functional groups: for example, the addition of a functional group can alter the electron density within a bond, thereby strengthening or weakening it. Depending on the context, this effect can be dramatic, especially in the biomedical/pharmaceutical discipline[215]. However, the ability to tune these bonds are limited to the available chemistry around the bond, as well as the quantized nature of functional groups (while there are methyl ($CH_3$) and ethyl ($C_2H_5$) groups, the carbon character cannot be continuously varied between these two groups). The nature of the entropic bond lends itself to being as continuously variable as the geometry of the nanoparticle, opening up new classes of mesoscale “chemistry”. Particles with the ability to change shape, for example through the altering of the aspect ratio, as in Chapter 5 and Chapter 6, would be able to change the entropic bonds that form, providing an alternate route for the creation of reconfigurable materials[9,11,13], self-healing materials[216–218], and other designer materials[219].

It is also useful to place the entropic bond in context of classic chemical bonds. Here I report the strength of entropic bond on the order of magnitude of $5k_{\mathrm{B}}T$ $\left(O(5k_{\mathrm{B}}T)\right)$. For systems at room temperature, this works out to $O(0.1\ eV)$ or $O\left(10\frac{kJ}{\mathrm{mol}}\right)$.

Table 3 Comparison of entropic bond strength to common chemical bond strength. All calculations are done on an order-of-magintude basis, and only report one significant figure. Hydrogen bonds and entropic bonds are shaded in gray to indicate they are on the same order of magnitude in terms of strength

| Bond | Strength $O(eV)$ | Strength $O(kJ/\mathrm{mol})$ |
|---|---|---|
| van der Waals | 0.01 | 1 |
| Entropic | 0.1 | 10 |
| Hydrogen | 0.1 | 10 |
| Metallic | 3 | 300 |
| Covalent | 4 | 400 |
| Ionic | 7 | 700 |

As seen in Table 3, the entropic bond is stronger than bonds formed by van der Waals forces, and are on the order of magnitude of hydrogen bonds, while being $O(10\%)$ the strength of metallic, covalent, and ionic bonds. This strengthens the comparison I made between entropic and hydrogen bonds in Chapter 5. In addition to the similarities in strength and directionality between entropic bonds and hydrogen bonds, the similarities between entropic bonds and other bonds should be further investigated. For example, the emergent nature of entropic bonds is similar to the delocalization of electron density in metallic bonds[175]. There are also other "non-classical bonds" e.g. mechanical bonds[220], and any similarities between these non-classical bonds should be investigated as well.

### 7.2.2 Emergent nature

While the emergent nature of the entropic bond makes the self-assembly of hard particle systems unique, these bonds and structures share similarities with well-known systems, providing insight into how scientists and engineers can contextualize and utilize entropic bonding to create new materials. Unlike chemical bonds, in entropic bonds, no electron density is shifted; rather, entropic bonds form through the shifting of entropy density. Chemical bonds are typically

defined intensively rather than extensively i.e. independent of their environment. For example, the hydrogen bonding force between two water molecules is the same at a given thermodynamic state point regardless of whether those two molecules are isolated or surrounded by moles of other water molecules. However, there exist many chemical systems that exhibit an emergent component to intermolecular forces and/or bonds. The strength of the van der Waals forces arising between polymer chains is a summation of the collective forces between billions of individual atoms, and the resulting polymeric structure is thus a result of these collective forces. In metallic systems, the metallic bonds and resulting band gaps are a result of the total number of atoms in the system; nanoscale metallic systems such as quantum dots[221–223] exhibit very different properties than their bulk counterparts due to their size[224–226]. The entropic bond thus shares some similarities with established chemical bonds, and should be similarly accepted.

For purely hard particles, there exists no intrinsic force holding the particles together, so that the stability of the self-assembled phase is a function of the volume/pressure of the system; the structure will fall apart if removed from confinement. These entropically-stabilized structures can thus be thought of having characteristics of both fluids and solids: like solids, they can have a well-defined structure, but like fluids, they depend on some kind of confinement to remain in a given configuration. Such hybrid materials are not unheard of, with liquid crystals being a canonical example of a material sharing aspects of fluids

and solids[114]. These materials provide some insight into how entropically self-assembled systems may be leveraged in material applications.

Liquid crystal elastomers (LCEs) are polymers with rigid, rod-like regions attached to a flexible polymer backbone[115]. By loosely cross-linking these polymers in the ordered liquid-crystalline state, they form solid structures with well-defined phase transitions. LCEs also possess unique, novel behavior resulting from the liquid crystalline state[227–229]. In a similar fashion, nanoparticles could be functionalized with polymer coatings and then cross-linked in the self-assembled state. The resulting material would then be locally constrained, retaining the ability for emergent directional entropic forces to direct the local arrangements of the nanoparticles. Such materials may exhibit novel material properties, similarly to LCEs.

## 7.3 Future Research

In Chapter 4, I analyze the preferred pair motifs in the fluid phase for systems of polyhedra. This pair motif analysis is very similar to the entropic bonding analysis performed in Chapter 5 and Chapter 6, but does not require the calculation of the PMFT for a three-dimensional system. While it is possible to compute PMFTs in three-dimensions $(x, y, z)$, these PMFTs do not fully account for the local pair geometry, as seen by comparing the PMFTs in Chapter 3 to those in Chapter 5 and Chapter 6. As discussed in Chapter 2, to truly understand the PMFT for systems of particles in three-dimensional space, a 6-dimensional PMFT must be computed. Such a PMFT presents significant challenges to calculate and analyze. The current algorithm to calculate the PMFT[129] will not scale to 6D

space, requiring more input data, more time to compute, and more hard-disk space to store the resulting PMFT. These challenges aside, there still exist the difficulties in analyzing and visualizing 6-dimensional space. The techniques employed in Chapter 4 effectively reduce the number of dimensions, and similar techniques may enable the creation of a suitable data structure and analysis technique for the 6D PMFT.

In Chapter 5 and Chapter 6, the PMFT analysis leveraged the relatively simply crystal structure to identify free-energy minima. This kind of preprocessing is not as suitable for more complex structures. Use of the machine learning techniques in Chapter 4 to identify the preferred pair motifs will result in more efficient and effective pre-processing for the image analysis of the free-energy landscape.

In Chapter 5 I discuss how an understanding the relative free-energies of particular bonds impact the resulting self-assembled structure. This kind of analysis should be applied to different systems, in both two- and three-dimensions, identifying potential nanoparticles that exhibit multiple phases as a function of their shape, similar to those in Chapter 6.

I discuss the entropic bond lifetime between nanoparticles in the Brownian limit in Chapter 5. The bond lifetime should be compared to systems with explicit kinetics, such as those modelled using DEM MD[92], into account. The kinetics and thermodynamics as measured by the PMFT should then be compared, developing a model accounting for entropic bond dynamics.

# Bibliography


1. Doucet, S. M. & Meadows, M. G. Iridescence: a functional perspective. *J. R. Soc. Interface* **6,** S115-32 (2009).

2. Maia, R., Caetano, J. V. O., Báo, S. N. & Macedo, R. H. Iridescent structural colour production in male blue-black grassquit feather barbules : the role of keratin and melanin. *J. R. Soc. Interface* **6,** S203--S211 (2009).

3. Saranathan, V. *et al.* Structure, function, and self-assembly of netrwork gyroid (I4_132) photonic crystals in butterfly wing scales. *Proc. …* **107,** 11676–11681 (2010).

4. Vukusic, P., Sambles, J. R., Lawrence, C. R. & Wootton, R. J. Quantified interference and diffraction in single Morpho butterfly scales. *Proc. R. Soc. London B Biol. Sci.* **266,** 1403–1411 (1999).

5. Prum, R. O., Quinn, T. & Torres, R. H. Anatomically diverse butterfly scales all produce structural colours by coherent scattering. *J. Exp. Biol.* **209,** 748–765 (2006).

6. McNamara, M. E. *et al.* Cryptic iridescence in a fossil weevil generated by single diamond photonic crystals. *J. R. Soc. Interface* **11,** (2014).

7. Vignolini, S. *et al.* Pointillist structural color in Pollia fruit. *Proc. Natl. Acad. Sci.* **109,** 15712–15715 (2012).

8. Kohlstedt, K. L. & Glotzer, S. C. Self-assembly and tunable mechanics of reconfigurable colloidal crystals. *Phys. Rev. E* **87,** 32305 (2013).

9. Bharti, B. & Velev, O. D. Assembly of Reconfigurable Colloidal Structures by Multidirectional Field-Induced Interactions. *Langmuir* **31,** 7897–908 (2015).

10. Nguyen, T. D., Jankowski, E. & Glotzer, S. C. Self-assembly and reconfigurability of shape-shifting particles. *ACS Nano* **5,** 8892–903 (2011).

11. Nguyen, T. D. & Glotzer, S. C. Reconfigurable assemblies of shape-changing nanorods. *ACS Nano* **4,** 2585–94 (2010).

12. Gibaud, T. *et al.* Reconfigurable self-assembly through chiral control of interfacial tension. *Nature* **481,** 348–351 (2012).

13. Kim, Y., Macfarlane, R. J., Jones, M. R. & Mirkin, C. A. Transmutable nanoparticles with reconfigurable surface ligands. *Science (80-. ).* **351,** 579–582 (2016).

14. Long, A. W., Phillips, C., Jankowski, E. & Ferguson, A. Nonlinear machine learning and design of reconfigurable digital colloids. *Soft Matter* **12,** 7119–7135 (2016).

15. Wojtecki, R. J., Meador, M. A. & Rowan, S. J. Using the dynamic bond to access macroscopically responsive structurally dynamic polymers. *Nat. Mater.* **10,** 14–27 (2011).

16. Youssef, M., Hueckel, T., Yi, G.-R. & Sacanna, S. Shape-shifting colloids via stimulated dewetting. *Nat. Commun.* **7,** 12216 (2016).

17. Palacci, J., Sacanna, S., Steinberg, A. P., Pine, D. J. & Chaikin, P. M. Living crystals of light-activated colloidal surfers. *Science (80-. ).* **339,** 936–40 (2013).

18. Song, P. *et al.* Patchy Particle Packing under Electric Fields. *J. Am. Chem. Soc.* (2015). doi:10.1021/ja5127903

19. Yethiraj, A., Wouterse, A., Groh, B. & van Blaaderen, A. Nature of an Electric-Field-Induced Colloidal Martensitic Transition. *Phys. Rev. Lett.* **92,** 58301 (2004).

20. Velichko, Y. S. Y. *et al.* Electric field controlled self-assembly of hierarchically ordered membranes. *Adv. Funct. Mater.* **22,** 369–377 (2012).

21. Shah, A. A., Schultz, B., Zhang, W., Glotzer, S. C. & Solomon, M. J. Actuation of shape-memory colloidal fibres of Janus ellipsoids. *Nat. Mater.* **14,** 117–124 (2015).

22. Wykes, M. S. D. *et al.* Dynamic self-assembly of microscale rotors and swimmers. *Soft Matter* 33 (2015). doi:10.1038/srep12528

23. Glotzer, S. C. & Solomon, M. J. Anisotropy of building blocks and their assembly into complex structures. *Nat. Mater.* **6,** 557–62 (2007).

24. Chen, Q., Bae, S. C. & Granick, S. Directed self-assembly of a colloidal kagome lattice. *Nature* **469,** 381–4 (2011).

25. Chen, Q., Bae, S. C. & Granick, S. Staged self-assembly of colloidal metastructures. *J. Am. Chem. Soc.* **134,** 11080–3 (2012).

26. Kraft, D. J., Groenewold, J. & Kegel, W. K. Colloidal molecules with well-controlled bond angles. *Soft Matter* **5,** 3823–3826 (2009).

27. Kraft, D. J. *et al.* Surface Roughness Directed Self-Assembly of Patchy Particles into Colloidal Micelles. *Proc. Natl. Acad. Sci.* **109,** 10787–10792 (2012).

28. Odriozola, G., Jimenez-Angeles, F., Lozada-Cassou, M., Jiménez-Ángeles, F. & Lozada-Cassou, M. Entropy Driven Key-Lock Assembly. *J. Chem. Phys.* **129,** 111101 (2008).

29. Wang, Y. *et al.* Colloids with valence and specific directional bonding. *Nature* **491,** 51–5 (2012).

30. Biben, T., Bladon, P. & Frenkel, D. Depletion effects in binary hard-sphere fluids. *J. Phys. Condens. Matter* **8,** 10799–10821 (1999).

31. Schilling, T., Pronk, S., Mulder, B. & Frenkel, D. Monte Carlo study of hard pentagons. *Phys. Rev. E* **71,** 36138 (2005).

32. Haji-Akbari, A. *et al.* Disordered, quasicrystalline and crystalline phases of densely packed tetrahedra. *Nature* **462,** 773–7 (2009).

33. Agarwal, U. & Escobedo, F. A. Mesophase behaviour of polyhedral particles. *Nat. Mater.* **10,** 230–235 (2011).

34. Damasceno, P. F., Engel, M. & Glotzer, S. C. Predictive self-assembly of polyhedra into complex structures. *Science (80-. ).* **337,** 453–7 (2012).

35. Avendano, C. & Escobedo, F. A. Phase behavior of rounded hard-squares. *Soft Matter* **8,** 4675–4681 (2012).

36. Smallenburg, F., Filion, L., Marechal, M. & Dijkstra, M. Vacancy-stabilized crystalline order in hard cubes. *Proc. Natl. Acad. Sci.* **109,** 17886--17890 (2012).

37. Sacanna, S., Irvine, W. T. M., Chaikin, P. M. & Pine, D. J. Lock and key colloids. *Nature* **464,** 575–8 (2010).

38. van Anders, G., Klotsa, D., Karas, A. S., Dodd, P. M. & Glotzer, S. C. Digital Alchemy for Materials Design: Colloids and Beyond. *ACS Nano* **9,** 9542–9553 (2015).

39. Frenkel, D. Simulations: The dark side. *Eur. Phys. J. Plus* 1–41 (2013).

40. Anderson, H. L. Metropolis, Monte Carlo, and the MANIAC. *Los Alamos Sci.* 96–108 (1986).

41. *History of Computing in the Twentieth Century*. (Academic Press, 1980).

42. Metropolis, N., Rosenbluth, A. W., Rosenbluth, M. N., Teller, A. H. & Teller,

E. Equation of State Calculations by Fast Computing Machines. *J. Chem. Phys.* **21,** 1087–1092 (1953).

43. Alder, B. J. & Wainwright, T. E. Phase Transition for a Hard Sphere System. *J. Chem. Physis* **27,** 1208–1209 (1957).

44. Frenkel, D. & Smit, B. *Understanding Molecular Simulation: From Algorithms to Applications*. (Academic Press, 2002).

45. Alder, B. J. & Wainwright, T. E. Phase transition in elastic disks. *Phys. Rev.* **127,** 359–361 (1962).

46. Anderson, V. J. & Lekkerkerker, H. N. W. Insights into phase transition kinetics from colloid science. *Nature* **416,** 811–815 (2002).

47. Frenkel, D. & Ladd, A. J. C. New Monte Carlo method to compute the free energy of arbitrary solids. Application to the fcc and hcp phases of hard spheres. *J. Chem. Phys.* **81,** 3188 (1984).

48. Hoover, W. G. Melting Transition and Communal Entropy for Hard Spheres. *J. Chem. Phys.* **49,** 3609 (1968).

49. Manoharan, V. N. Colloidal matter: Packing, geometry, and entropy. *Science (80-. ).* **349,** 942 (2015).

50. Kirkwood, J. G. Molecular Distribution in Liquids. *J. Chem. Phys.* **7,** 919--925 (1939).

51. Kirkwood, J. G. & Monroe, E. Statistical Mechanics of Fusion. *J. Chem. Phys.* **9,** 514–526 (1941).

52. Kirkwood, J. G. & Boggs, E. M. The radial distribution function in liquids. *J. Chem. Phys.* **10,** 394–402 (1942).

53. Kirkwood, J. G., Maun, E. K. & Alder, B. J. J. Radial Distribution Functions and the Equation of State of a Fluid Composed of Rigid Spherical Molecules. *J. Chem. Phys.* **18,** 1040–1047 (1950).

54. Wood, W. W. & Jacobson, J. D. Preliminary Results from a Recalculation of the Monte Carlo Equation of State of Hard Spheres. *J. Chem. Phys.* **27,** 1207 (1957).

55. Asakura, S. & Oosawa, F. Interaction between Particles Suspended in Solutions of Macromolecules. *J. Polym. Sci.* **33,** 183–192 (1958).

56. Oosawa, F. & Asakura, S. On Interaction between Two Bodies Immersed in a Solution of Macromolecules. *J. Chem. Phys.* **22,** 1255–1256 (1954).

57. Oosawa, F. & Asakura, S. Surface Tension of High-Polymer Solutions. *J. Chem. Phys.* **22,** 1255–1256 (1954).

58. Mao, Y., Cates, M. E. & Lekkerkerker, H. N. W. Depletion force in colloidal systems. *Phys. A Stat. Mech. its Appl.* **222,** 10–24 (1995).

59. Binder, K., Virnau, P. & Statt, A. Perspective: The Asakura Oosawa model: A colloid prototype for bulk and interfacial phase behavior. *J. Chem. Phys.* **141,** (2014).

60. van Anders, G., Klotsa, D., Ahmed, N. K., Engel, M. & Glotzer, S. C. Understanding shape entropy through local dense packing. *Proc. Natl. Acad. Sci.* **111,** E4812–E4821 (2014).

61. de Boer, J. Molecular distribution and equation of state of gases. *Reports Prog. Phys.* **12,** 305–374 (1949).

62. Tao, A. R., Habas, S. & Yang, P. Shape control of colloidal metal nanocrystals. *Small* **4,** 310–325 (2008).

63. Stein, A., Li, F. & Wang, Z. Synthesis of shaped particles and particle arrays by disassembly methods. *J. Mater. Chem.* **19,** 2102–2106 (2009).

64. Sacanna, S. & Pine, D. J. Shape-Anisotropic Colloids: Building Blocks for Complex Assemblies. *Curr. Opin. Colloid Interface Sci.* **16,** 96–105 (2011).

65. Cademartiri, L., Bishop, K. J. M., Snyder, P. W. & Ozin, G. A. Using Shape for Self-Assembly. *Philos. Trans. R. Soc. A* **370,** 2824–2847 (2012).

66. Xia, Y., Xiong, Y., Lim, B. & Skrabalak, S. E. Shape-Controlled Synthesis of Metal Nanocrystals: Simple Chemistry Meets Complex Physics? *Angew. Chemie Int. Ed.* **48,** 60–103 (2009).

67. Senyuk, B. *et al.* Topological colloids. *Nature* **493,** 200–205 (2013).

68. Henzie, J., Grünwald, M., Widmer-Cooper, A., Geissler, P. L. & Yang, P. Self-assembly of uniform polyhedral silver nanocrystals into densest packings and exotic superlattices. *Nat. Mater.* **11,** 131–7 (2012).

69. Padilla, J. E., Colovos, C. & Yeates, T. O. Nanohedra: using symmetry to design self assembling protein cages, layers, crystals, and filaments. *Proc. Natl. Acad. Sci.* **98,** 2217–21 (2001).

70. Haji-Akbari, A., Engel, M. & Glotzer, S. C. Phase diagram of hard tetrahedra. *J. Chem. Phys.* **135,** 194101 (2011).

71. Cadotte, A. T., Dshemuchadse, J., Damasceno, P. F., Newman, R. S. & Glotzer, S. C. Self-assembly of a space-tessellating structure in the binary

system of hard tetrahedra and octahedra. *Soft Matter* **12,** 7073--7078 (2016).

72. Damasceno, P. F., Engel, M. & Glotzer, S. C. Crystalline Assemblies and Densest Packings of a Family of Truncated Tetrahedra and the Role of Directional Entropic Forces. *ACS Nano* **6,** 609–614 (2012).

73. Schultz, B. A., Damasceno, P. F., Engel, M. & Glotzer, S. C. Symmetry Considerations for the Targeted Assembly of Entropically Stabilized Colloidal Crystals via Voronoi Particles. *ACS Nano* 150218161039001 (2015). doi:10.1021/nn507490j

74. Engel, M., Damasceno, P. F., Phillips, C. L. & Glotzer, S. C. Computational self-assembly of a one-component icosahedral quasicrystal. *Nat. Mater.* **14,** 109–116 (2015).

75. Sanders, J. V. Close-packed structures of spheres of two different sizes I. Observations on natural opal. *Philos. Mag. A* **42,** 705–720 (1980).

76. Murray, M. J. & Sanders, J. V. Close-packed structures of spheres of two different sizes II. The packing densities of likely arrangements. *Philos. Mag. A* **42,** 721–740 (1980).

77. Bartlett, P., Ottewill, R. H. & Pusey, P. N. Superlattice formation in binary mixtures of hard-sphere colloids. *Phys. Rev. Lett.* **68,** 3801–3804 (1992).

78. Eldridge, M. D., Madden, P. A. & Frenkel, D. Entropy-driven formation of a superlattice in a hard-sphere binary mixture. *Nature* **365,** 35–37 (1993).

79. Trizac, E., Eldridge, M. D. & Madden, P. A. Stability of the AB crystal for asymmetric binary hard sphere mixtures. *Mol. Phys.* **90,** 675–678 (1997).

80. Zhao, K., Bruinsma, R. & Mason, T. G. Entropic Crystal--Crystal Transitions of Brownian Squares. *Proc. Natl. Acad. Sci.* **108,** 2684–2687 (2011).

81. Torquato, S. & Jiao, Y. Dense packings of the Platonic and Archimedean solids. *Nature* **460,** 876–9 (2009).

82. van Anders, G., Ahmed, N. K., Smith, R., Engel, M. & Glotzer, S. C. Entropically Patchy Particles: Engineering Valence through Shape Entropy. *ACS Nano* **8,** 931–40 (2014).

83. Millan, J. A., Ortiz, D., van Anders, G. & Glotzer, S. C. Self-Assembly of Archimedean Tilings with Enthalpically and Entropically Patchy Polygons. *ACS Nano* **8,** 2918--2928 (2014).

84. Chandler, D. *Introduction to Modern Statistical Mechanics*. (Oxford

University Press, 1987).

85. Walter, J. C. & Barkema, G. T. An introduction to Monte Carlo methods. *Phys. A Stat. Mech. its Appl.* **418,** 78–87 (2014).

86. Alder, B. J. & Wainwright, T. E. Studies in Molecular Dynamics. I. General Method. *J. Chem. Phys.* **31,** 459 (1959).

87. Anderson, J. a., Lorenz, C. D. & Travesset, a. General purpose molecular dynamics simulations fully implemented on graphics processing units. *J. Comput. Phys.* **227,** 5342–5359 (2008).

88. Marson, R. L., Phillips, C. L., Anderson, J. A. & Glotzer, S. C. Phase Behavior and Complex Crystal Structure of Self-Assembled Tethered Nanoparticle Telechelics. *Nano Lett.* **14,** 2071--2078 (2014).

89. Frenkel, D. & Smit, B. *Understanding Molecular Simulations: From Algorithms to Applications*. (Elsevier, 2002).

90. John, B. S. & Escobedo, F. A. Phase behavior of colloidal hard tetragonal parallelepipeds (cuboids): a Monte Carlo simulation study. *J. Phys. Chem. B* **109,** 23008–15 (2005).

91. John, B. S., Stroock, A. & Escobedo, F. A. Cubatic liquid-crystalline behavior in a system of hard cuboids. *J. Chem. Phys.* **120,** 9383–9 (2004).

92. Spellings, M., Marson, R., Anderson, J. A. & Glotzer, S. C. GPU accelerated Discrete Element Method (DEM) Molecular Dynamics for convervative, faceted particle simulations. *J. Comput. Phys.* **334,** 460–467 (2017).

93. Anderson, J. A., Eric Irrgang, M. & Glotzer, S. C. Scalable Metropolis Monte Carlo for simulation of hard shapes. *Comput. Phys. Commun.* **204,** 21–30 (2016).

94. Fernández, L. A., Martin-Mayor, V., Seoane, B. & Verrocchio, P. Equilibrium Fluid-Solid Coexistence of Hard Spheres. *Phys. Rev. Lett.* **108,** 165701 (2012).

95. Fortini, A. & Dijkstra, M. Phase behaviour of hard spheres confined between parallel hard plates: manipulation of colloidal crystal structures by confinement. *J. Phys. Condens. Matter* **18,** L371 (2006).

96. Noya, E. G., Vega, C. & De Miguel, E. Determination of the melting point of hard spheres from direct coexistence simulation methods. *J. Chem. Phys.* **128,** 154507–1--154507–7 (2008).

97. Davidchack, R. L. & Laird, B. B. Simulation of the hard-sphere crystal-melt

interface. *J. Chem. Phys.* **108,** 9452–62 (1998).

98. Speedy, R. J. Pressure of the metastable hard-sphere fluid. *J. Phys. Condens. Matter* **9,** 8591 (1997).

99. Odriozola, G. Replica exchange Monte Carlo applied to hard spheres. *J. Chem. Phys.* **131,** (2009).

100. Isobe, M. & Krauth, W. Hard-sphere melting and crystallization with event-chain Monte Carlo. *J. Chem. Phys.* **143,** 2–7 (2015).

101. *Density Functional Methods in Chemistry*. (Springer, 1991). doi:10.1007/978-1-4612-3136-3

102. Kohn, W., Becke, A. D. & Parr, R. G. Density Functional Theory of Electronic Structure. *J. Phys. Chem.* **100,** 12974–12980 (1996).

103. Cousty, J., Bertrand, G., Najman, L. & Couprie, M. Watershed Cuts: Minimum Spanning Forests and the Drop of Water Principle. *Pattern Anal. Mach. Intell. IEEE Trans.* **31,** 1362–1374 (2009).

104. van der Walt, S. *et al.* Scikit-image: image processing in Python. *PeerJ* **2,** e453 (2014).

105. Smeeton, L. C., Oakley, M. T. & Johnston, R. L. Visualizing energy landscapes with metric disconnectivity graphs. *J. Comput. Chem.* **35,** 1481–1490 (2014).

106. Wales, D. J. Energy landscapes: some new horizons. *Curr. Opin. Struct. Biol.* **20,** 3–10 (2010).

107. Becker, O. M. & Karplus, M. The topology of multidimensional potential energy surfaces: Theory and application to peptide structure and kinetics. *J. Chem. Phys.* **106,** 1495 (1997).

108. Anderson, J. A., Antonaglia, J., Millan, J. A., Engel, M. & Glotzer, S. C. Shape and symmetry determine two-dimensional melting transition of hard polygons. *Phys. Rev. X* **7,** 2001 (2017).

109. Engel, M. *et al.* Hard-disk equation of state: First-order liquid-hexatic transition in two dimenstions with three simulation methods. *Phys. Rev. E* **87,** 1–9 (2013).

110. Bernard, E. P. & Krauth, W. Two-Step Melting in Two Dimensions: First-Order Liquid-Hexatic Transition. *Phys. Rev. Lett.* **107,** 155704 (2011).

111. Kapfer, S. C. & Krauth, W. Soft-disk melting: From liquid-hexatic coexistence to continuous transitions. *arXiv* 4 (2014).

112. Whitelam, S., Tamblyn, I., Beton, P. H. & Garrahan, J. P. Random and ordered phases of off-lattice rhombus tiles. *Phys. Rev. Lett.* **108,** 1–4 (2012).

113. Haji-Akbari, A. & Glotzer, S. C. Strong Orientational Coordinates and Orientational Order Parameters For Symmetric Objects. *J. Phys. A Math. Theor.* **48,** 1–19 (2015).

114. Gennes, P. de & Prost, J. *The Physics of Liquid Crystals*. (Oxford University Press, 1995).

115. Warner, M. & Terentjev, E. M. *Liquid Crystal Elastomers*. (Oxford University Press, 2007).

116. Maaten, L. Van Der & Hinton, G. Visualizing Data using t-SNE. *J. Mach. Learn. Res. 1* **620,** 267–284 (2017).

117. Van Der Maaten, L. Accelerating t-SNE Using Tree-based Algorithms. *J. Mach. Learn. Res.* **15,** 3221–3245 (2014).

118. Pedregosa, F. *et al.* Scikit-learn: Machine Learning in Python. *J. Mach. Learn. Res.* **12,** 2825–2830 (2011).

119. Spellings, M. & Glotzer, S. C. Machine learning for crystal identification and discovery. (2017).

120. Dempster, A. P., Laird, N. M. & Rubin, D. B. Maximum likelihood from incomplete data via the EM algorithm. *J. R. Stat. Soc. Ser. B Methodol.* **39,** 1–38 (1977).

121. Baudry, J. P., Raferty, A. E., Celeux Gilles, Lo Kenneth & Gottardo, R. Combining mixture components for clustering. *J. Comput. Graph. Stat.* **19,** 332–353 (2010).

122. Bragg, W. H. & Bragg, W. L. The Reflection of X-rays by Crystals. *Proc. R. Soc. London A Math. Phys. Eng. Sci.* **88,** 428–438 (1913).

123. Rosvall, M. & Bergstrom, C. T. Mapping change in large networks. *PLoS One* **5,** (2010).

124. Anderson, J. A. & Glotzer, S. C. The development and expansion of HOOMD-blue through six years of GPU proliferation. *arXiv* 1308.5587 (2013).

125. Howard, M. P., Anderson, J. A., Nikoubashman, A., Glotzer, S. C. & Panagiotopoulos, A. Z. Efficient neighbor list calculation for molecular simulation of colloidal systems using graphics processing units. *Comput. Phys. Commun.* **203,** 45–52 (2016).

126. Anderson, J. A. HOOMD-blue. Available at: http://codeblue.umich.edu/hoomd-blue.

127. Anderson, J. A., Irrgang, M. E. & Glotzer, S. C. High Performance Hard Particle Monte CArlo. *Preprint* (2015).

128. Glaser, J. *et al.* Strong scaling of general-purpose molecular dynamics simulations on GPUs. *Comput. Phys. Commun.* **192,** 97–107 (2015).

129. Harper, E. S., Spellings, M. P., Anderson, J. A. & Glotzer, Sharon, C. Freud: A Software Suite for High-Throughput Analysis. (2017). doi:10.5281/zenodo.166564

130. Harper, E. S., Spellings, M. P., Anderson, J. A. & Glotzer, S. C. freud. (2016). doi:10.5281/zenodo.166564

131. van der Walt, S., Colbert, S. C. & Varoquaux, G. The NumPy Array: A Structure for Efficient Numerical Computation. *Comput. Sci. Eng.* **13,** 22–30 (2011).

132. Jones, E., Oliphant, T., Peterson, P. & others. SciPy: Open source scientific tools for Python. (2001).

133. Oliphant, T. E. Python for Scientific Computing. *Comput. Sci. Eng.* **9,** 10–20 (2007).

134. Millman, K. J. & Aivazis, M. Python for Scientists and Engineers. *Comput. Sci. Eng.* **13,** 9–12 (2011).

135. Pérez, F. & Granger, B. E. IPython: a System for Interactive Scientific Computing. *Comput. Sci. Eng.* **9,** 21–29 (2007).

136. Hunter, J. D. Matplotlib: A 2D graphics environment. *Comput. Sci. Eng.* **9,** 90–95 (2007).

137. Ramachandran, P. & Varoquaux, G. Mayavi: 3D Visualization of Scientific Data. *Comput. Sci. Eng.* **13,** 40–51 (2011).

138. Harper, E. S., Marson, R. L., Anderson, J. A., van Anders, G. & Glotzer, S. C. Shape allophiles improve entropic assembly. *Soft Matter* **11,** 7250–7256 (2015).

139. King, N. P. *et al.* Computational design of self-assembling protein nanomaterials with atomic level accuracy. *Science (80-. ).* **336,** 1171–4 (2012).

140. Lai, Y.-T., King, N. P. & Yeates, T. O. Principles for designing ordered protein assemblies. *Trends Cell Biol.* **22,** 653–61 (2012).

141. Lanci, C. C. J. *et al.* Computational design of a protein crystal. *Proc. Nation* **109,** 7304–7309 (2012).

142. Bortolini, C. *et al.* The position of hydrophobic residues tunes peptide self-assembly. *Soft Matter* **10,** 5656–5661 (2014).

143. Chen, R. & Weng, Z. A Novel Shape Complementarity Scoring Function for Protein-Protein Docking. *Proteins Struct. Funct. Genet.* 397–408 (2003). doi:10.1002/prot.10334

144. Piazza, R. Protein interactions and association: an open challenge for colloid science. *Curr. Opin. Colloid Interface Sci.* **8,** 515–522 (2004).

145. Ulijn, R. V. Molecular self-assembly: Best of both worlds. *Nat. Nanotechnol.* **10,** 295–296 (2015).

146. Yao, L. *et al.* Near field capillary repulsion. *Soft Matter* **9,** 779 (2012).

147. Paik, T. & Murray, C. B. Shape-Directed Binary Assembly of Anisotropic Nanoplates: A Nanocrystal Puzzle with Shape-Complementary Building Blocks. *Nano Lett.* **13,** 2952–2956 (2013).

148. Colòn-Melèndez, L. *et al.* Binding kinetics of lock and key colloids. *J. Chem. Phys.* **142,** 174909(1)-174909(9) (2015).

149. König, P.-M. *et al.* Lock and Key Model System. *Eur. Lett.* **84,** 68006 (2008).

150. Wojciechowski, K. W. & Frenkel, D. Tetratic phase in the planar hard square system? *Comput. Methods Sci. Technol.* **10,** 235–255 (2004).

151. Weber, T. & Stillinger, F. Melting of square crystals in two dimensions. *Phys. Rev. E* **48,** 4351–4358 (1993).

152. Donev, A., Burton, J., Stillinger, F. H. F. & Torquato, S. Tetratic order in the phase behavior of a hard-rectangle system. *Phys. Rev. B* **73,** 54109 (2006).

153. Triplett, D. A. & Fichthorn, K. A. Monte Carlo simulation of two-dimensional hard rectangles: Confinement effects. *Phys. Rev. E* **77,** 11707 (2008).

154. Dillmann, P., Maret, G. & Keim, P. Comparison of 2D melting criteria in a colloidal system. *J. Phys. Condens. Matter* **24,** 464118 (2012).

155. Deutschländer, S. *et al.* Two-Dimensional Melting under Quenched Disorder. *Phys. Rev. Le* **111,** 98301 (2013).

156. Towns, J. *et al.* XSEDE: Accelerating Scientific Discovery. *Comput. Sci.*

*Eng.* **16,** 62–74 (2014).

157. Texas Advanced Computing Center. Available at: http://www.tacc.utexas.edu.

158. Gantapara, A. P., Qi, W. & Dijkstra, M. A Novel Chiral Phase of Achiral Hard Triangles and an Entropy-Driven Demixing of Enantiomers. *arXiv* (2015).

159. Gao, B., Alvi, Y., Rosen, D., Lav, M. & Tao, A. R. Designer nanojunctions: orienting shaped nanoparticles within polymer thin-film nanocomposites. *Chem. Commun.* **49,** 4382–4384 (2013).

160. Rosen, D. a. & Tao, A. R. Modeling the Optical Properties of Bowtie Antenna Generated By Self-Assembled Ag Triangular Nanoprisms. *ACS Appl. Mater. Interfaces* **6,** 4134–4142 (2014).

161. Tritschler, U. & Cölfen, H. Self-assembled hierarchically structured organic-inorganic composite systems. *Bioinspir. Biomim.* **11,** 35002 (2016).

162. Pfeifer, W. & Saccà, B. From Nano to Macro through Hierarchical Self-Assembly: The DNA Paradigm. *ChemBioChem* 1–19 (2016). doi:10.1002/cbic.201600034

163. Whitelam, S. Hierarchical assembly may be a way to make large information-rich structures. *Soft Matter* **11,** 8225--8235 (2015).

164. Morphew, D. & Chakrabarti, D. Supracolloidal reconfigurable polyhedra via hierarchical self-assembly. *Soft Matter* **12,** 9633–9640 (2016).

165. Zhou, Y., Marson, R. & Et, A. Biomimetic Hierarchical Assembly of Helical Supraparticles from Chiral Nanoparticles. *ACS Nano* **10,** 3248--3256 (2016).

166. Jankowski, E. & Glotzer, S. C. Screening and designing patchy particles for optimized self-assembly propensity through assembly pathway engineering. *Soft Matter* **8,** 2852 (2012).

167. Zeravcic, Z., Manoharan, V. N. & Brenner, M. P. Size limits of self-assembled colloidal structures made using specific interactions. *Proc. Natl. Acad. Sci.* **111,** 15918–15923 (2014).

168. Rossi, L. *et al.* Cubic Crystals from Cubic Colloids. *Soft Matter* **7,** 4139–4142 (2011).

169. Ni, R., Gantapara, A. P., de Graaf, J., van Roij, R. & Dijkstra, M. Phase diagram of colloidal hard superballs: from cubes via spheres to octahedra. *Soft Matter* **8,** 8826 (2012).

170. Gantapara, A. P., de Graaf, J., van Roij, R. & Dijkstra, M. Phase behavior of a family of truncated hard cubes. *J. Chem. Phys.* **142,** 54904 (2015).

171. Seo, D., Ji, C. P. & Song, H. Polyhedral gold nanocrystals with O_h symmetry: From octahedra to cubes. *J. Am. Chem. Soc.* **128,** 14863–14870 (2006).

172. John, B. S., Juhlin, C. & Escobedo, F. A. Phase behavior of colloidal hard perfect tetragonal parallelepipeds. *J. Chem. Phys.* **128,** 44909 (2008).

173. Harper, E. S., van Anders, G. & Glotzer, S. C. Nature of the Entropic Bond in Particle Assemblies. *Submitt. to Nat.* (2018).

174. Pauling, L. The nature of the chemical bond. Application of results obtained from the quantum mechanics and from a theory of paramagnetic susceptibility to the structure of molecules. *J. Am. Chem. Soc.* **53,** 1367–1400 (1931).

175. Pauling, L. *The Nature of the Chemical Bond*. (Cornell University Press, 1960).

176. Arunan, E. *et al.* Definition of the hydrogen bond (IUPAC Recommendations 2011). *Pure Appl. Chem.* **83,** 1637–1641 (2011).

177. Desiraju, G. R. A bond by any other name. *Angew. Chemie - Int. Ed.* **50,** 52–59 (2011).

178. Nic, M., Jirat, J. & Kosata, B. IUPAC. Compendium of Chemical Terminology, 2nd ed. (the 'Gold Book'). doi:10.1351/goldbook

179. Ye, X. *et al.* Competition of shape and interaction patchiness for self-assembling nanoplates. *Nat. Chem.* **5,** 466–73 (2013).

180. Park, S. Y. *et al.* DNA-programmable nanoparticle crystallization. *Nature* **451,** 553–6 (2008).

181. Macfarlane, R. J. *et al.* Nanoparticle superlattice engineering with DNA. *Science (80-. ).* **334,** 204–8 (2011).

182. Ashton, D., Jack, R. & Wilding, N. Self-assembly of colloidal polymers via depletion-mediated lock and key binding. *Soft Matter* **9,** 9661--9666 (2013).

183. Beltran-Villegas, D. J., Colón-Meléndez, L., Solomon, M. J. & Larson, R. G. Kinetic modeling and design of colloidal lock and key assembly. *J. Colloid Interface Sci.* **463,** 242–257 (2016).

184. Ahmed, N. K., van Anders, G., Chen, E. R. & Glotzer, S. C. Crossover Behavior in the Packing and Assembly of Multivalent Lock-and-Key

Colloids. *arXiv* (2016).

185. Sciortino, F., Poole, P. H., Stanley, H. E. & Havlin, S. Lifetime of the bond network and gel-like anomalies in supercooled water. *Phys. Rev. Lett.* **64,** 1686–1689 (1990).

186. Sciortino, F. & Fornili, S. L. Hydrogen bond cooperativity in simulated water: Time dependence analysis of pair interaction. *J. Chem. Phys.* **90,** 2786 (1989).

187. Sciortino, F., Geiger, A. & Stanley, H. E. Network defects and molecular mobility in liquid water. *J. Chem. Phys.* **96,** 3857--3865 (1992).

188. Koga, K. & Tanaka, H. Rearrangement dynamics of the hydrogen-bonded network of clathrate hydrates encaging polar guest. *J. Chem. Phys.* **104,** 263–72 (1996).

189. Martiniano, H. F. M. C. & Galamba, N. Insights on hydrogen-bond lifetimes in liquid and supercooled water. *J. Phys. Chem. B* **117,** 16188–16195 (2013).

190. Luzar, A. Resolving the hydrogen bond dynamics conundrum. *J. Chem. Phys.* **113,** 10663–10675 (2000).

191. Starr, F. W., Nielsen, J. K. & Stanley, H. E. Fast and slow dynamics of hydrogen bonds in liquid water. *Phys. Rev. Lett.* **82,** 2294–2297 (1998).

192. Stannard, A. *et al.* Broken symmetry and the variation of critical properties in the phase behaviour of supramolecular rhombus tilings. *Nat. Chem.* **4,** 112–117 (2011).

193. Garrahan, J. P., Stannard, A., Blunt, M. O. & Beton, P. H. Molecular random tilings as glasses. *Proc. Natl. Acad. Sci.* **106,** 15209–15213 (2009).

194. Blunt, M. O. *et al.* Random Tiling and Topological Defects in a Two-Dimensional Molecular Network. *Science (80-. ).* **322,** 1077–1081 (2008).

195. Zhang, Z. *et al.* Supersnowflakes: Stepwise Self-Assembly and Dynamics Exchange of RHombus Star-Shaped Supramolecules. *J. Am. Chem. Soc.* **139,** 8174–8185 (2017).

196. Pivetta, M., Blüm, M. C., Patthey, F. & Schneider, W. D. Two-dimensional tiling by rubrene molecules self-assembled in supramolecular pentagons, hexagons, and heptagons on a Au(111) surface. *Angew. Chemie - Int. Ed.* **47,** 1076–1079 (2008).

197. Zhao, K. & Mason, T. G. Twinning of rhombic colloidal crystals. *J. Am. Chem. Soc.* **134,** 18125–18131 (2012).

198. Dedovets, D., Bauduin, P., Causse, J., Girard, L. & Diat, O. Switchable self-assembly of Prussian blue analogs nano-tiles triggered by salt stimulus. *Phys. Chem. Chem. Phys.* **18,** 3188–3196 (2016).

199. Ye, X. *et al.* Morphologically controlled synthesis of colloidal upconversion nanophosphors and their shape-directed self-assembly. *Proc. Natl. Acad. Sci.* **107,** 22430–22435 (2010).

200. Zhang, Y. W., Sun, X., Si, R., You, L. P. & Yan, C. H. Single-crystalline and monodisperse LaF3 triangular nanoplates from a single-source precursor. *J. Am. Chem. Soc.* **127,** 3260–3261 (2005).

201. Zhao, K. & Mason, T. G. Frustrated rotator crystals and glasses of brownian pentagons. *Phys. Rev. Lett.* **103,** 13–16 (2009).

202. Zhao, K., Bruinsma, R. & Mason, T. G. Local chiral symmetry breaking in triatic liquid crystals. *Nat. Commun.* **3,** 801 (2012).

203. Widom, M., Mosseri, R., Destainville, N. & Bailly, F. Arctic octahedron in three-dimensional rhombus tilings and related integer solid partitions. *J. Stat. Phys.* **109,** 945–965 (2002).

204. Krattenthaler, C. Descending plane partitions and rhombus tilings of a hexagon with a triangular hole. *Eur. J. Comb.* **27,** 1138–1146 (2006).

205. Destainville, N. Entropy and boundary conditions in random rhombus tilings. *J. Phys. A. Math. Gen.* **31,** 6123–6139 (1998).

206. Kasteleyn, P. W. Dimer Statistics and Phase Transitions. *J. Math. Phys.* **4,** 287–293 (1963).

207. Fisher, M. E. & Stephenson, J. Statistical mechanics of dimers on a plane lattice. II. Dimer correlations and monomers. *Phys. Rev.* **132,** 1411–1431 (1963).

208. Wales, D. *Energy Landscapes: Applications to Clusters, Biomolecules and Glasses*. (Cambridge University Press, 2003).

209. Smeeton, L. No Title. (2016).

210. Shen, W. *et al.* Orientational Ordering of Hard Regular Polygons in Plastic Crystals. *Submitt. to PRL* 1–7 (2017).

211. Kosterlitz, J. M. & Thouless, D. J. Long range order and metastability in two dimensional solids and superfluids. *J. Phys. C Solid State Phys.* **5,** L-124--L-126 (1972).

212. Halperin, B. I. & Nelson, D. R. Theory of Two-Dimensional Melting. *Phys.*

*Rev. Lett.* **41,** 121–124 (1978).

213. Young, A. P. P. Melting and vector Coulomb gas in two dimensions. *Lab At. Solid State Phys.* **19,** (1979).

214. Zahn, D. Thermodynamics and Kinetics of Prenucleation Clusters, Classical and Non-Classical Nucleation. *ChemPhysChem* **16,** 2069–2075 (2015).

215. Mandal, T., Marson, R. L. & Larson, R. G. Coarse-grained modeling of crystal growth and polymorphism of a model pharmaceutical molecule. *Soft Matter* **12,** 8246–8255 (2016).

216. Casagrande, C., Fabre, P., Raphael, E. & Veyssie, M. 'Janus Beads': Realization and Behaviour at Water/Oil Interfaces. *Europhys. Lett.* **9,** 251–255 (1989).

217. Elsukova, A. *et al.* Structure, morphology, and aging of Ag-Fe dumbbell nanoparticles. *Phys. Status Solidi A* **208,** 2437–2442 (2011).

218. Kumar, A., Park, B. J., Tu, F. & Lee, D. Amphiphilic Janus particles at fluid interfaces. *Soft Matter* **9,** 6604--6617 (2013).

219. Talapin, D. V., Lee, J.-S., Kovalenko, M. V. & Shevchenko, E. V. Prospects of Colloidal Nanocrystals for Electronic and Optoelectronic Applications. *Chem. Rev.* **110,** 389–458 (2010).

220. Stoddartd, J. F. & Bruns, C. J. *The Nature of the Mechanical Bond: From Molecules to Machines*. (Wiley, 2016).

221. Pietryga, J. M. *et al.* Spectroscopic and device aspects of nanocrystal quantum dots. *Chem. Rev.* **116,** 10513–10622 (2016).

222. Wang, Y. *et al.* Preparation of primary amine derivatives of the magic-size nanocluster (CdSe)13. *Inorg. Chem.* **52,** 2933–2938 (2013).

223. Liu, Y. H., Wayman, V. L., Gibbons, P. C., Loomis, R. A. & Buhro, W. E. Origin of high photoluminescence efficiencies in CdSe quantum belts. *Nano Lett.* **10,** 352–357 (2010).

224. Brus, L. Electronic wave functions in semiconductor clusters: Experiment and theory. *J. Phys. Chem.* **90,** 2555–2560 (1986).

225. Brus, L. Quantum crystallites and nonlinear optics. *Appl. Phys. A Solids Surfaces* **53,** 465–474 (1991).

226. Brus, L. E. & Brus, L. E. The size dependence of the lowest excited electronic state Electron-electron and electron-hole interactions in small

semiconductor crystallites : The size dependence of the lowest excited electronic state. **4403,** (1998).

227. Corbett, D. & Warner, M. Nonlinear photoresponse of disordered elastomers. *Phys. Rev. Lett.* **96,** 1–4 (2006).

228. Biggins, J. S., Warner, M. & Bhattacharya, K. Elasticity of polydomain liquid crystal elastomers. *J. Mech. Phys. Solids* **60,** 573–590 (2012).

229. Ware, T. H., Biggins, J. S., Shick, A. F., Warner, M. & White, T. J. Localized soft elasticity in liquid crystal elastomers. *Nat. Commun.* **7,** 10781 (2016).